NOVEL DETECTION METHODS FOR CHEMICAL EXCHANGE AND APPLICATION TO BREAST CANCER IMAGING

APPROVED BY SUPERVISORY COMMITTEE

Elena Vinogradov, Ph.D.

Ananth Madhuranthakam, Ph.D.

Robert Lenkinski, Ph.D.

Dean Sherry, Ph.D.

Ivan Pedrosa, M.D., Ph.D.

DEDICATION

First and foremost, I would like to thank my supervisor and mentor Dr. Elena Vinogradov for her continuous guidance, encouragement and support. Her enthusiasm for science and insightful comments inspires my excitement about molecular imaging. She teaches me how to ask scientific questions, think critically and helps me grow in the field of magnetic resonance imaging. I learn a lot from her not only on the academic side, but also lifetime wisdom. It is a true pleasure to have her as my mentor.

I would like to thank my dissertation committee members, Drs. Ananth Madhuranthakam, Robert Lenkinski, Dean Sherry and Ivan Pedrosa, for their time, inspirational discussions and suggestions. I would like to thank members in our research group that make these projects possible. I am especially grateful to Kelli Key for her help in recruiting the volunteers, to Trevor Wigal for his help during human scans, to Asghar Hajibeigi and Khaled Nasr for their help with the phantoms, to Drs. Stephen Seiler and Emily

Knippa for their help of the breast cancer study, and to Drs. Ivan Dimitrov and Jochen Keupp from Philips for their technical support.

I also would like to thank all the former and current lab members, Zheng Liu, Bian Li, Huajun She, Ece Ercan, Josh Greer, Crystal Harrison, Xinzeng Wang, Quyen Do, Yue Zhang and Durgesh Dwivedi for their help, encouragement and friendship. Thank you for making the very joyful lab environment.

Lastly, I would like to thank my family. Many thanks to my husband, Xinzeng, for always being there for me and unconditional support. Many thanks to my parents for supporting me in pursuing the PhD degree oversea. A special thanks goes to my newborn daughter Emily, whose arrival not only brings me a great joy, but also gives me more power to work hard.

NOVEL DETECTION METHODS FOR CHEMICAL EXCHANGE AND APPLICATION TO BREAST CANCER IMAGING

by

SHU ZHANG

DISSERTATION / THESIS

Presented to the Faculty of the Graduate School of Biomedical Sciences

The University of Texas Southwestern Medical Center at Dallas

In Partial Fulfillment of the Requirements

For the Degree of

DOCTOR OF PHILOSOPHY

The University of Texas Southwestern Medical Center at Dallas

Dallas, Texas

August, 2018

NOVEL DETECTION METHODS FOR CHEMICAL EXCHANGE AND APPLICATION TO BREAST CANCER IMAGING

Publication No. _____

Shu Zhang, M.E.

The University of Texas Southwestern Medical Center at Dallas, 2018

Supervising Professor: Elena Vinogradov, Ph.D.

Chemical exchange saturation transfer (CEST) is a novel contrast mechanism that is based on the chemical exchange processes between the protons in water and solutes. CEST can indirectly detect the low concentrated solutes, which are not observable with conventional MRI and indicate the quantitative environmental parameters such as pH. Therefore, many promising applications of CEST are explored. The aim of my projects is to develop new CEST imaging techniques and apply these techniques in human studies at 3 T. The first project is to develop a fast and quantitative imaging method based on the balanced steady-

state free precession sequence as an alternative way for chemical exchange detection (bSSFPX). The feasibility of bSSFPX for chemical exchange detection was proved both theoretically through Bloch-McConnell Equations simulations and experimentally by phantoms studies. Analytical models for bSSFPX were developed for quantitative measurements of $T_{1\rho}$ and exchange rate. In a first in vivo experiment, bSSFPX was applied in the human brain to detect the chemical exchange possibly from fast exchanging metabolites with resonance frequencies close to water that would be challenging at 3 T for standard CEST imaging methods. As a new CEST data acquisition method, the bSSFPX experiment holds high promise for fast, quantitative and 3D CEST imaging.

The second project is to develop a CEST-Dixon sequence for fat free CEST imaging and apply it to breast cancer imaging. The influence of non-exchanging fat on CEST imaging was studied by simulation, in phantoms, and in vivo at different fat fractions and echo times. The CEST-Dixon method has been proved to eliminate lipid contamination robustly in breast CEST imaging. In the breast cancer study, higher CEST effects were observed in the more aggressive cancer group than the less aggressive cancer, benign and normal groups in all three frequencies ranges (hydroxyl, amine and amide) explored, while no significant differences were observed between the less aggressive cancer, benign and normal groups. In addition, significant correlation between MTR_{asym} and Ki-67 was observed for cancer groups. While the study is preliminary, the results indicate that the CEST-Dixon method may differentiate between more aggressive and less aggressive breast cancer.

TABLE OF CONTENTS

PRIOR PUBLICATIONS

1. **Zhang S**, Seiler S, Wang X, Madhuranthakam AJ, Keupp J, Lenkinski RE, Vinogradov E. CEST-Dixon for human breast lesion characterization at 3 T: A preliminary study. Magn Reson Med 2018; PMID: 29322559, DOI:10.1002/mrm.27079.
2. **Zhang S**, Keupp J, Wang X, Dimitrov I, Madhuranthakam AJ, Lenkinski RE, Vinogradov E. Z-spectrum appearance and interpretation in the presence of fat: Influence of acquisition parameters. Magn Reson Med 2018; 79(5):2731-2737. PMID: 28862349, PMCID: PMC5821535, DOI: 10.1002/mrm.26900.
3. **Zhang S**, Liu Z, Grant A, Keupp J, Lenkinski RE, Vinogradov E. Balanced Steady-State Free Precession (bSSFP) from an effective field perspective: Application to the detection of chemical exchange (bSSFPX). J Magn Reson 2017; 275:55-67. PMID: 28012297, PMCID: PMC5810596, DOI: 10.1016/j.jmr.2016.12.002.
4. She H, Greer JS, **Zhang S**, Li B, Keupp J, Madhuranthakam AJ, Dimitrov IE, Lenkinski RE, Vinogradov E. Accelerating Chemical Exchange Saturation Transfer MRI with Parallel Blind Compressed Sensing. Magn Reson Med; Accepted.

LIST OF FIGURES

LIST OF TABLES

LIST OF APPENDICES

LIST OF DEFINITIONS

^{1}H	Proton
APT	Amide proton transfer
bSSFP	Balanced steady-state free precession
bSSFPX	Balanced steady-state free precession for exchange detection
CEST	Chemical exchange saturation transfer
CNR	Contrast-to-noise ratio
CNS	Central nervous system
CW	Continuous wave
DCE	Dynamic contrast-enhanced
ER	Estrogen receptor
eTHRIVE	Enhanced T_1 high-resolution isotropic volume excitation
FA	Flip angle
FF	Fat fraction
FOV	Field of view
GAG	Glycosaminoglycan
gagCEST	Glycosaminoglycan chemical exchange saturation transfer
gluCEST	Glutamate chemical exchange saturation transfer
GM	Gray matter
HS	Hyperbolic secant
hyperCEST	Hyperpolarized chemical exchange saturation transfer
IDC	Invasive ductal carcinoma

IP	In-phase
IVD	Intervertebral disk
lipoCEST	Liposomal chemical exchange saturation transfer
MICEST	Myo-inositol chemical exchange saturation transfer
MRI	Magnetic resonance imaging
MRS	Magnetic resonance spectroscopy
MT	Magnetization transfer
MTR_{asym}	Magnetization transfer ratio asymmetry
NMR	Nuclear magnetic resonance
NOE	Nuclear overhauser enhancement
OP	Out-of-phase
paraCEST	Paramagnetic chemical exchange saturation transfer
PTR	Proton transfer ratio
QUESP	Quantifying exchange using saturation power
QUEST	Quantifying exchange using saturation time
RF	Radio frequency
ROI	Region of interest
SAR	Specific absorption rate
SL	Spin-locking
SNR	Signal-to-noise ratio
SPIR	Spectral presaturation with inversion recovery
STIR	Short TI inversion recovery

TFE	Turbo filed echo
TNBC	Triple-negative breast cancer
TSE	Turbo spin echo
WASSR	Water saturation shift referencing
WM	White matter

CHAPTER ONE
Introduction to Chemical Exchange Saturation Transfer

1.1 OVERVIEW

This chapter introduces underlying principles of chemical exchange saturation transfer (CEST) imaging, the analytical solutions to Bloch-McConnell Equations which are used to mathematically describe the CEST processes, the imaging sequence for CEST data acquisition and the sources of endogenous CEST contrast.

1.2 CHEMICAL EXCHANGE SATURATION TRANSFER

CEST is a novel contrast mechanism in magnetic resonance imaging (MRI) (1). It employs selective saturation of exchangeable protons in a solute pool which transfers to water via chemical exchange. The exchangeable protons can be amide, amine or hydroxyl protons in the protein backbones and small molecules such as creatine, urea and glucose (2-5). The solute pools are at low concentration, typically in the μM - mM range, hence cannot be directly detected in conventional MRI scans. The CEST imaging provides a way of indirect detection of these low concentrated solutes by analyzing water signal decrease. Compared with proton MR spectroscopy (MRS), which directly detects the signals from the solute pools, the CEST imaging significantly increases the sensitivity to certain molecules or a group of molecules (6). As a result, much higher spatial resolution can be achieved using

the CEST imaging technique compared with MRS, which is particularly desirable for clinical applications. Moreover, due to the dependence on exchange rate, CEST is sensitive to the quantitative environmental parameters, such as pH and temperature (7-9). Therefore, CEST methodology is a focus of increased research interest that may lead to a significant clinical impact.

1.2.1 Mechanism

The underlying principle of CEST is shown in Figure 1-1 (6,10-12). The exchangeable protons in a solute pool resonates at a different frequency from the water protons. If the exchangeable protons in the solute pool are selectively saturated by a radio frequency (RF) irradiation, then the saturation can be transferred to the water pool through the chemical exchange, hence bringing down the water signal. If the RF irradiation lasts long enough, the water signal can be significantly reduced due to the continuous chemical exchange process. Eventually, a steady-state can be reached between the water signal reduction via the chemical exchange and the water signal recovery via longitudinal relaxation.

In a CEST experiment, frequency-dependent saturation effects are visualized by plotting the measured water signals against the RF irradiation frequency, the so-called Z-spectrum (Fig. 1-2). The water signal is normalized to a reference signal (S_0) acquired with RF irradiation applied far away from both the water and solute pools. Conventionally, the water frequency is assigned to 0 ppm in a Z-spectrum, hence the x-axis is the frequency

offset with regard to water. The dip in the middle of the Z-spectrum is caused by direct water saturation. The direct water saturation is symmetric about the water frequency. The smaller dip in the Z-spectrum is caused by the CEST process between the solute and water pools. The CEST effect is commonly measured by magnetization transfer ratio (MTR) asymmetry analysis (Fig. 1-2):

$$MTR_{asym} = \frac{S_{sat}(-\omega_s) - S_{sat}(\omega_s)}{S_0} \qquad [1.1]$$

where $S_{sat}(-\omega_s)$ and $S_{sat}(\omega_s)$ are the Z-spectrum intensities acquired with the RF irradiation applied on-resonance with the solute pool (ω_s) and at the frequency symmetric around water ($-\omega_s$), and S_0 is the reference signal. MTR_{asym} analysis removes direct water saturation and other non-CEST contributions with an implicit assumption that these contributions are symmetric around water.

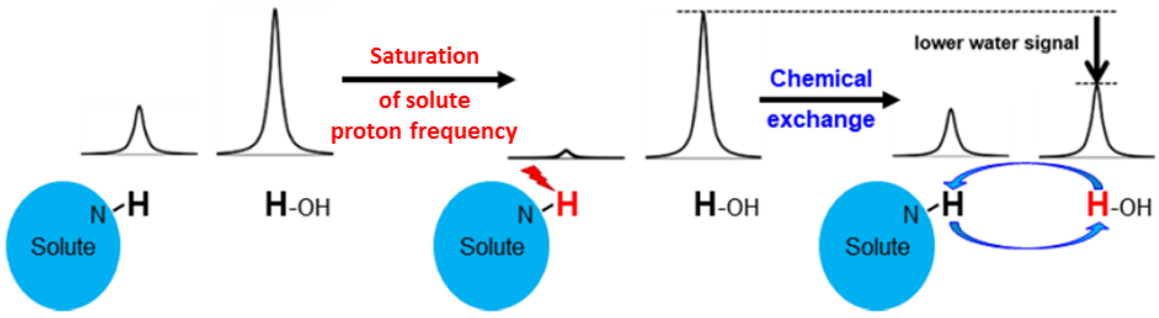

Figure 1-1 Schematic of CEST.
Selective saturation (lightning bolt) of a proton (red) on solute causes the proton's MR signal to disappear. Chemical exchange of protons between solute and water (blue arrows) transfers the saturation to water, lowering the MR signal from water.

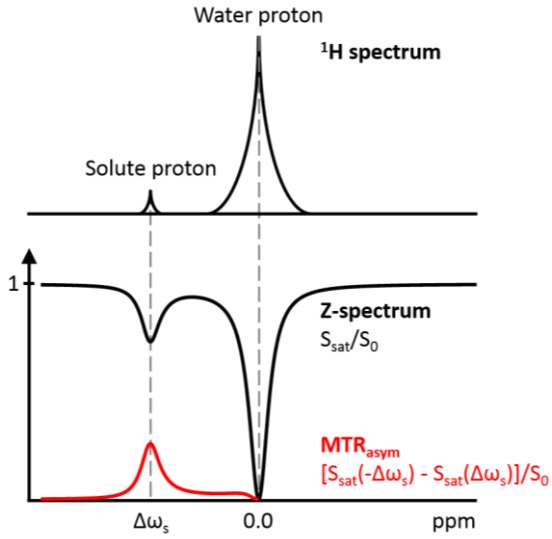

Figure 1-2 Schematic of CEST experiment
Water and solute protons have different chemical shifts. Z-spectrum is the measurement of normalized water signals against RF off-resonance irradiation frequencies, with respect to water (which is assigned to 0 ppm). MTR_{asym} is the asymmetry of the Z-spectrum versus RF off-resonance.

For a successful CEST experiment, the system is required to be in the slow to intermediate exchange regime: $k_{ex} < \Delta f_{sw}$, where $k_{ex} = k_{sw} + k_{ws}$, k_{sw} is the exchange rate from the solute pool to the water pool and k_{ws} is the exchange rate of the reversed direction, and Δf_{sw} is the chemical shift between the solute and water pools. Although, successful CEST in intermediate and even fast exchange regimes were observed (13-15).

1.2.2 Source of endogenous CEST signals

The CEST signals can originate from either endogenous or exogenous contrast agents. Paramagnetic CEST contrast agents (paraCEST) (16), contrast agents using liposomes (lipoCEST) (17), hyperpolarized gases (hyperCEST) (18), and exogenously

injected glucose (14,19) fall into the exogenous CEST category. The endogenous CEST relies on the endogenous contrast agents, such as proteins and metabolites. The endogenous CEST is the focus of my dissertation.

For endogenous CEST, the effect usually originates from amide, amine or hydroxyl chemical groups. The amide group can be from the backbones of proteins or peptides, with a chemical shift approximately 3.5 ppm downfield of water. The exchange rate is in the range of 10 - 30 Hz which puts the amide protons in the slow exchange regime (8,10). The amine group is from the side chains of amino acid such as arginine or small molecules such as urea and creatine. The chemical shift is between 2 - 3 ppm downfield of water and the exchange rate is on the order of several kHz to tens of kHz, putting the amine protons in the intermediate to fast exchange regime. The hydroxyl group is from small molecules such as choline, myo-inositol and glucose and sugar polymers such as glycogen and glycosaminoglycan. The hydroxyl group locates approximately 1 ppm downfield of water and with an exchange rate > 1000 Hz, putting hydroxyl protons in the fast exchange regime.

1.2.3 Confounding saturation transfer effects

CEST is a part of the saturation transfer family. The other two important members are magnetization transfer (MT) and nuclear Overhauser effect (NOE). These two effects often accompany CEST effect for *in vivo* imaging. Broadly, the MT contrast originates from dipole-dipole interactions in the macromolecule pools with restricted mobility. Hence, these macromolecules possess very short T_2 (on the order of ten to several tens of μs) and a very

broad spectrum (on the order of tens of kHz), as shown in Figure 1-3. The macromolecular pool is slightly asymmetric around water (20,21).

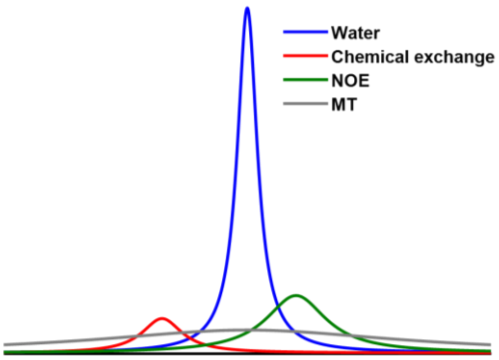

Figure 1-3 Schematic spectrum of water and different saturation transfer sources.

The NOE effect can be observed in brain and cartilage and is attributed to exchange relayed magnetization transfer through aliphatic or oliphatic protons (22-24). It appears from -5 to 0 ppm in the Z-spectrum. MT and NOE are two confounding factors of the CEST effect, especially when MTR_{asym} is used as a measurement of CEST effect. Therefore, great research effort is dedicated to remove or separate MT and NOE from CEST which will be discussed later in this chapter in details.

1.3 THEORY

1.3.1 Two pools exchange modeling for CEST

The simplest model for CEST is a two-pool exchange model consisting of a water pool (subscript w) and a solute pool (subscript s) as shown in Figure 1-4.

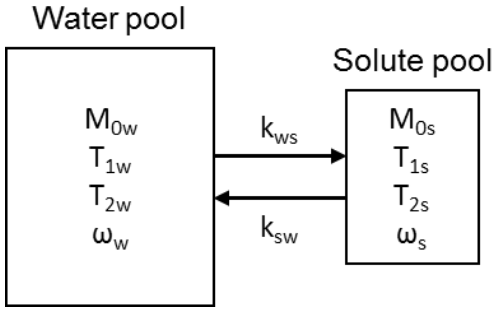

Figure 1-4 Two-pool exchange model for CEST.
M_0 is the thermal equilibrium z-magnetization. T_1 and T_2 are longitudinal and transverse relaxation times. ω is the resonance frequency. k_{sw} is the exchange rate from the solute pool to the water pool and k_{ws} is the exchange rate of reversed direction.

The Bloch-McConnell Equations are used to describe the two-pool exchange (25):

$$\frac{d}{dt}\begin{bmatrix} M_{xw} \\ M_{yw} \\ M_{zw} \\ M_{xs} \\ M_{ys} \\ M_{zs} \end{bmatrix} = \begin{bmatrix} -r_{2w} & \Delta\omega_w & -\omega_{1y} & k_{sw} & 0 & 0 \\ -\Delta\omega_w & -r_{2w} & \omega_{1x} & 0 & k_{sw} & 0 \\ \omega_{1y} & -\omega_{1x} & -r_{1w} & 0 & 0 & k_{sw} \\ k_{ws} & 0 & 0 & -r_{2s} & \Delta\omega_s & -\omega_{1y} \\ 0 & k_{ws} & 0 & -\Delta\omega_s & -r_{2s} & \omega_{1x} \\ 0 & 0 & k_{ws} & \omega_{1y} & -\omega_{1x} & -r_{1s} \end{bmatrix} \begin{bmatrix} M_{xw} \\ M_{yw} \\ M_{zw} \\ M_{xs} \\ M_{ys} \\ M_{zs} \end{bmatrix} + \begin{bmatrix} 0 \\ 0 \\ R_{1w}M_{0w} \\ 0 \\ 0 \\ R_{1s}M_{0s} \end{bmatrix} \quad [1.2]$$

where $R_1 = 1/T_1$ and $R_2 = 1/T_2$ are the longitudinal and transverse relaxation rates, $r_{2w} = R_{2w} + k_{ws}$, $r_{1w} = R_{1w} + k_{ws}$, $r_{2s} = R_{2s} + k_{sw}$, $r_{1s} = R_{1s} + k_{sw}$, $\Delta\omega_w = \omega_w - \omega$ and $\Delta\omega_s = \omega_s - \omega$ are the frequency offsets between water (ω_w)/solute (ω_s) and RF saturation (ω). The mass balance relationship applies to the exchange rates:

$$k_{sw}M_{0s} = k_{ws}M_{0w} \quad [1.3]$$

Equation 1.2 has the form of:

$$\frac{dM}{dt} = AM + C \quad [1.4]$$

The general solution to Equation 1.2 is:

$$M(t) = [M(0) + A^{-1}C]e^{At} - A^{-1}C \qquad [1.5]$$

In addition to the above solution, there are several mathematical models for Equation 1.2. Two of the models are commonly used, as described in more details below.

1.3.1.1 Weak saturation pulse assumption

The first approach makes weak saturation pulse (WSP) assumption (26,27). In the WSP assumption, the applied RF irradiation only affects the solute pool while the water pool is unperturbed. For simplicity and without loss of generality, the derivation assumes the RF irradiation is applied along the x-axis. Under the WSP assumption, the terms containing $\Delta\omega_w$ and ω_1 in the water pool can be ignored. Thus, the Equation 1.2 can be simplified to:

$$\frac{d}{dt}\begin{bmatrix} M_{xw} \\ M_{yw} \\ M_{zw} \\ M_{xs} \\ M_{ys} \\ M_{zs} \end{bmatrix} = \begin{bmatrix} -r_{2w} & 0 & 0 & k_{sw} & 0 & 0 \\ 0 & -r_{2w} & 0 & 0 & k_{sw} & 0 \\ 0 & 0 & -r_{1w} & 0 & 0 & k_{sw} \\ k_{ws} & 0 & 0 & -r_{2s} & \Delta\omega_s & 0 \\ 0 & k_{ws} & 0 & -\Delta\omega_s & -r_{2s} & \omega_1 \\ 0 & 0 & k_{ws} & 0 & -\omega_1 & -r_{1s} \end{bmatrix} \begin{bmatrix} M_{xw} \\ M_{yw} \\ M_{zw} \\ M_{xs} \\ M_{ys} \\ M_{zs} \end{bmatrix} + \begin{bmatrix} 0 \\ 0 \\ R_{1w}M_{0w} \\ 0 \\ 0 \\ R_{1s}M_{0s} \end{bmatrix} \qquad [1.6]$$

Equation 1.6 can be solved in the steady-state, where all the derivatives equal to 0. The steady-state z-magnetizations of the solute and water pools are:

$$\frac{M_{zs}^{ss}}{M_{0s}} = \frac{pq + \frac{q}{p}\Delta\omega_s^2}{\omega_1^2 + pq + \frac{q}{p}\Delta\omega_s^2} = 1 - \alpha \qquad [1.7]$$

$$\frac{M_{zw}^{ss}}{M_{0w}} = 1 - \frac{k_{ws}}{r_{1w}} \cdot \frac{\omega_1^2}{\omega_1^2 + pq + \frac{q}{p}\Delta\omega_s^2} = 1 - \frac{k_{ws}}{r_{1w}} \cdot \alpha \qquad [1.8]$$

where $p = r_{2s} - \frac{k_{sw}k_{ws}}{r_{2w}}$, $q = r_{1s} - \frac{k_{sw}k_{ws}}{r_{1w}}$ and α is the labeling efficiency:

$$\alpha = 1 - \frac{M_{zs}^{ss}}{M_{0s}} = \frac{\omega_1^2}{\omega_1^2 + pq + \frac{q}{p}\Delta\omega_s^2} \quad [1.9]$$

The CEST effect can be measured by proton transfer ratio (PTR), which is defined as:

$$PTR = 1 - \frac{M_{zw}^{ss}}{M_{0s}} = \frac{k_{ws}}{r_{1w}} \cdot \frac{\omega_1^2}{\omega_1^2 + pq + \frac{q}{p}\Delta\omega_s^2} = \frac{k_{ws}}{r_{1w}} \cdot \alpha \quad [1.10]$$

The time dependent z-magnetization of the water pool and PTR can also be derived. The derivation assumes that the solute pool reaches its steady-state instantly once the RF irradiation is applied, however the solute pool is not yet in the steady-state. Hence, dM_{zw}/dt in Equation 1.6 becomes:

$$\frac{dM_{zw}}{dt} = -r_{1w}M_{zw} + R_{1w}M_{0w} + k_{sw}M_{zs}^{ss} \quad [1.11]$$

Equation 1.11 has the solution

$$\frac{M_{zw}(t)}{M_{0w}} = -\frac{k_{ws}}{r_{1w}}\alpha(1 - e^{-r_{1w}t}) + 1 \quad [1.12]$$

As a result, the time dependent PTR is:

$$PTR = 1 - \frac{M_{zw}(t)}{M_{0s}} = \frac{k_{ws}}{r_{1w}}\alpha(1 - e^{-r_{1w}t}) \quad [1.13]$$

For a two-pool CEST model:

$$MTR_{asym} = \frac{M_{zw}(-\omega_s) - M_{zw}(\omega_s)}{M_{zw}^0} = PTR \quad [1.14]$$

1.3.1.2 Effective field theory and $T_{1\rho}$ relaxation

Another approach to solve Equation 1.2 is derived based on the effective field theory and utilizes the similarities between the CEST and spin-locking (SL) experiments (28-30). For simplicity and without loss of generality, the derivation assumes the RF irradiation is applied along the x-axis and the RF irradiation is of constant amplitude. This leads to production of an effective field as shown in Figure 1-5a, red arrow. It is the vector sum of the RF saturation component B_1 and off-resonance component $\Delta\omega_w/\gamma$.

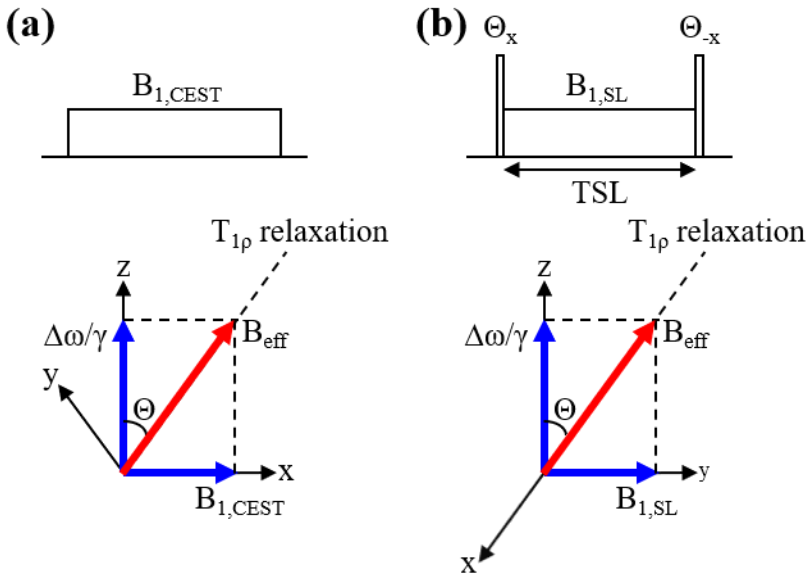

Figure 1-5 The effective field of CEST and SL.
The CEST (a) and SL (b) preparation pulse sequences and the effective fields. $B_{1,CEST}$ is the RF saturation strength of a CEST experiment. The SL preparation pulse sequence consists of three pulses: the pulse Θ_x to tip the magnetization, the SL pulse with a strength of $B_{1,SL}$ and a duration of TSL to lock the magnetization, and the pulse Θ_{-x} to tip the magnetization back to the longitudinal axis. $\Delta\omega$ is the frequency offset, γ is the gyromagnetic ratio, B_{eff} is the effective field and Θ is the angle between the effective field and the z-axis. The $T_{1\rho}$ relaxation occurs along the effective field direction.

If there is only water pool present and the magnetization starts from the thermal equilibrium, the magnetization component along the effective field is:

$$M_{zweff}(0) = M_{zw}^{0}\cos\Theta_w \qquad [1.15]$$

The magnetization component along the effective field undergoes $T_{1\rho}$ relaxation that is the relaxation time constant for the decay of magnetization along the effective field in the rotating frame:

$$M_{zweff}(t) = M_{zweff}^{ss}(1-e^{-t/T_{1\rho,w}}) + M_{zweff}(0)e^{-t/T_{1\rho,w}} \qquad [1.16]$$

where M_{zweff}^{ss} is the steady-state water signal along the effective field and $T_{1\rho,w} = 1/R_{1\rho,w}$ with $R_{1\rho,w} = R_{1w}\cos^2\Theta_w + R_{2w}\sin^2\Theta_w$. Therefore, the measured signal along the z-axis is:

$$\begin{aligned} M_{zw}(t) &= M_{zweff}(t)\sin\Theta_w \\ &= M_{zweff}^{ss}\sin\Theta_w(1-e^{-t/T_{1\rho}}) + M_{zweff}(0)\sin\Theta_w e^{-t/T_{1\rho}} \\ &= M_{zweff}^{ss}\sin\Theta_w(1-e^{-t/T_{1\rho}}) + M_{zw}^{0}\cos\Theta_w\sin\Theta_w e^{-t/T_{1\rho}} \\ &= M_{zw}^{ss}(1-e^{-t/T_{1\rho}}) + M_{zw}(0)e^{-t/T_{1\rho}} \end{aligned} \qquad [1.17]$$

The expression of M_{zw}^{ss} can be derived based on the Bloch Equations:

$$\frac{d}{dt}\begin{bmatrix} M_{xw} \\ M_{yw} \\ M_{zw} \end{bmatrix} = \begin{bmatrix} -R_2 & \Delta\omega_w & 0 \\ -\Delta\omega_w & -R_2 & \omega_1 \\ 0 & -\omega_1 & -R_1 \end{bmatrix}\begin{bmatrix} M_{xw} \\ M_{yw} \\ M_{zw} \end{bmatrix} + \begin{bmatrix} 0 \\ 0 \\ R_{1w}M_{0w} \end{bmatrix} \qquad [1.18]$$

In the steady-state, all the derivatives equal to 0. Hence the steady-state water z-magnetization can be solved as:

$$\frac{M_{zw}^{ss}}{M_{0w}} = \frac{R_{1w}\left(A+\cos^2\Theta_w\right)}{R_{1w}A + R_{1\rho,w}} \qquad [1.19]$$

where $R_{1\rho,w} = R_{1w}\cos^2\Theta_w + R_{2w}\sin^2\Theta_w$, $\cos^2\Theta_w = \frac{\Delta\omega_w^2}{\Delta\omega_w^2 + \omega_1^2}$, $\sin^2\Theta_w = \frac{\omega_1^2}{\Delta\omega_w^2 + \omega_1^2}$ and $A = \frac{R_{2w}^2}{\Delta\omega_w^2 + \omega_1^2}$. If ω_1 is large enough, then $A \to 0$. Thus Equation 1.16 can be simplified to:

$$\frac{M_{zw}^{ss}}{M_{0w}} = \frac{R_{1w}\cos^2\Theta_w}{R_{1\rho,w}} \qquad [1.20]$$

Substitute Equation 1.20 into Equation 1.17, the time dependent signal is:

$$\frac{M_{zw}(t)}{M_{0w}} = \frac{R_{1w}\cos^2\Theta_w}{R_{1\rho,w}}(1 - e^{-t/T_{1\rho}}) + \cos\Theta_w e^{-t/T_{1\rho}} \qquad [1.21]$$

If the exchanging solute pool is also present, then the derivations above hold for the two-pool case with the exchange term R_{ex} , added to the $R_{1\rho,w}$: $R_{1\rho,w} = R_{1w}\cos^2\Theta_w + (R_{2w} + R_{ex})\sin^2\Theta_w$.

There are two commonly used expressions for R_{ex}. One is (31):

$$R_{ex} = \frac{p_w p_s \Delta\omega_{sw}^2 k_{ex}}{\frac{\omega_{weff}^2 \omega_{seff}^2}{\overline{\omega_{eff}}^2} + k_{ex}^2} \qquad [1.22]$$

where $p_w = \frac{M_{0w}}{M_{0w} + M_{0s}}$, $p_s = \frac{M_{0s}}{M_{0w} + M_{0s}}$, $\Delta\omega_{sw} = \omega_s - \omega_w$, $\omega_{weff}^2 = \Delta\omega_w^2 + \omega_1^2$, $\omega_{seff}^2 = \Delta\omega_s^2 + \omega_1^2$, $\overline{\Delta\omega_{sw}} = p_w\Delta\omega_w + p_s\Delta\omega_s$ and $\overline{\omega_{eff}}^2 = \overline{\Delta\omega_{sw}}^2 + \omega_1^2$. The other is (32):

$$R_{ex} = k_{ws}\frac{\Delta\omega_{sw}^2}{\frac{\Gamma^2}{4} + \Delta\omega_s^2} + f_s R_{2s}\frac{\Delta\omega_{weff}^2}{\frac{\Gamma^2}{4} + \Delta\omega_s^2} + \frac{k_{ws}R_{2s}r_{2s}}{\frac{\Gamma^2}{4} + \Delta\omega_s^2} \qquad [1.23]$$

where $\Gamma = 2\sqrt{\frac{r_{2s}}{k_{sw}}\omega_1^2 + r_{2s}^2}$. Compared with the R_{ex} in Equation 1.22, the R_{ex} in Equation 1.23 takes the R_{2s} into consideration. This model ignores the magnetization component perpendicular to the effective field. This is valid when T_1 and T_2 values are small compared with the saturation time.

The SL experiment can also be used to probe exchange processes because $T_{1\rho}$ is sensitive to exchange (Eqs. 1.22, 1.23) (29,33). Unlike a CEST experiment that uses a long saturation for magnetization preparation (Fig. 1-5a, the CEST imaging sequence will be discussed in detail in Section 1.4.1), a set of three pulses is used for magnetization preparation in a SL experiment: the first pulse is to tip the longitudinal magnetization to align with the lock direction, followed by a SL pulse to "lock" the magnetization and the last pulse is to tip the magnetization back to the longitudinal axis prior to acquisition sequence (Fig. 1-5b). During the SL pulse the magnetization decays with $T_{1\rho}$ time constant.

There are two types of SL experiments, on-resonance SL (Θ = 90º, RF applied exactly at water resonance) and off-resonance SL (RF applied at off-resonance from water). Often, the on-resonance SL experiment probes exchange via a $T_{1\rho}$ dispersion curve (the dependence of $T_{1\rho}$ on the SL pulse strength $B_{1,SL}$) or a quantitative $T_{1\rho}$ map. The off-resonance SL experiment acquires the offset frequency dependent SL spectrum in a way very similar to the Z-spectrum acquisition of a CEST experiment. Indeed, a sub-set of off-resonance SL experiments, specifically aimed at the detection of the exchange, was named chemical exchange imaging with spin-lock technique (CESL). The CEST and CESL

experiments are sensitive to slow to intermediate exchange while the on-resonance SL experiment is more sensitive to fast exchange (29,33).

1.3.2 Three pools exchange modeling for CEST

As mentioned in the previous section 1.2.3, MT should be taken into account for in vivo CEST imaging. A three-pool model including a water pool, a solute pool and a macromolecule pool is used for mathematical description of both CEST and MT effects. As shown in Figure 1-6, there is always exchange of magnetizations between the water and the other pools (via chemical exchange or dipole-dipole interaction). However, the exchange between the solute and the macromolecule pools is negligible.

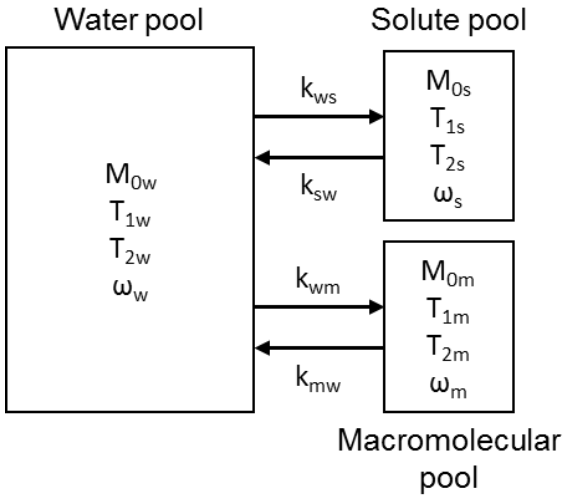

Figure 1-6 Three-pool exchange model for CEST and MT.
M_0 is the thermal equilibrium z-magnetization. T_1 and T_2 are longitudinal and transverse relaxation times. ω is the resonance frequency. k_{sw} is the exchange rate from the solute pool to the water pool and k_{ws} is the exchange rate of reversed direction. k_{mw} is the exchange rate from the macromolecule pool to the water pool and k_{wm} is the exchange rate of reversed direction.

The Bloch-McConnell Equations are used to describe the three-pool model (34-37):

$$\frac{d}{dt}\begin{bmatrix} M_{xw} \\ M_{yw} \\ M_{zw} \\ M_{xs} \\ M_{ys} \\ M_{zs} \\ M_{zm} \end{bmatrix} = \begin{bmatrix} -r_{2w} & \Delta\omega_w & -\omega_{1y} & k_{sw} & 0 & 0 & 0 \\ -\Delta\omega_w & -r_{2w} & \omega_{1x} & 0 & k_{sw} & 0 & 0 \\ \omega_{1y} & -\omega_{1x} & -r_{1w} & 0 & 0 & k_{sw} & k_{mw} \\ k_{ws} & 0 & 0 & -r_{2s} & \Delta\omega_s & -\omega_{1y} & 0 \\ 0 & k_{ws} & 0 & -\Delta\omega_s & -r_{2s} & \omega_{1x} & 0 \\ 0 & 0 & k_{ws} & \omega_{1y} & -\omega_{1x} & -r_{1s} & 0 \\ 0 & 0 & k_{wm} & 0 & 0 & 0 & -k_{mw} - R_{rfm} \end{bmatrix} \begin{bmatrix} M_{xw} \\ M_{yw} \\ M_{zw} \\ M_{xs} \\ M_{ys} \\ M_{zs} \\ M_{zm} \end{bmatrix} + \begin{bmatrix} 0 \\ 0 \\ R_{1w}M_{0w} \\ 0 \\ 0 \\ R_{1s}M_{0s} \\ R_{1m}M_{0m} \end{bmatrix} \quad [1.24]$$

where

$$R_{rfm} = \pi\omega_1^2 g_m(\Delta\omega_m) \quad [1.25]$$

$g_m(\Delta\omega_m)$ is the line shape of the macromolecule pool, which can be Lorentzian, Gaussian and super-Lorentzian. The super-Lorenztian line shape works well in tissues (Eq. 1.26).

$$g_m(\Delta\omega_m) = \int_0^{\pi/2} \sin\theta \sqrt{\frac{2}{\pi}} \frac{T_{2m}}{3\cos^2\theta - 1} e^{-2\left(\frac{\Delta\omega_m T_{2m}}{3\cos^2\theta - 1}\right)^2} d\theta \quad [1.26]$$

Because macromolecules have very short T_2 due to restricted motion, the transverse magnetizations are ignored in this model.

Since Equation 1.24 has the form of $dM/dt = AM + C$ the same as Equation 1.2, the analytical solution to Equation 1.2 in Equation 1.5 is also valid for the Equation 1.24.

It has been reported that the macromolecule pool is slightly asymmetric about water (20,21). As a result, the MTR_{asym} does not equal to PTR when a macromolecule pool is present. Instead, it contains an additional term to account for macromolecule pool asymmetry:

$$MTR_{asym} = PTR + MTR'_{asym} \quad [1.27]$$

1.4 CEST IMAGING

1.4.1 Imaging sequence

A basic CEST imaging sequence consists of saturation and acquisition units for a range of saturation frequencies. The saturation can be achieved in two ways: the continuous wave (CW) saturation and the pulsed saturation (Figs. 1-7 and 1-8). To reach the steady-state of the spin system, there are also two ways: the steady-state method and the segmented steady-state method. The saturation scheme of either the steady-state method or the segmented steady-state method can be CW or pulsed. Many methods can be used for image acquisition, including but not limited to echo planar imaging (EPI), turbo spin echo (TSE) and turbo field echo (TFE). This section focuses on the saturation part.

In addition to the basic, conventional, CEST imaging sequences, there are several other non-standard sequences achieving CEST effect, such as saturation with frequency alternating RF irradiation (SAFARI) (38) and frequency-labeled exchange transfer (FLEX) (39,40).

1.4.1.1 Continuous wave saturation

CW saturation employs RF irradiation of constant amplitude. The schematic of the CW CEST imaging sequence is shown in Figure 1-7. The saturation time (t_{sat}) is usually long

(t_{sat} >> T_{1w}) to ensure a steady-state of the system before the image acquisition. The acquired signal is the Z-magnetization of water. Hence, a crusher gradient follows the CW saturation to destroy the transverse magnetization before image acquisition.

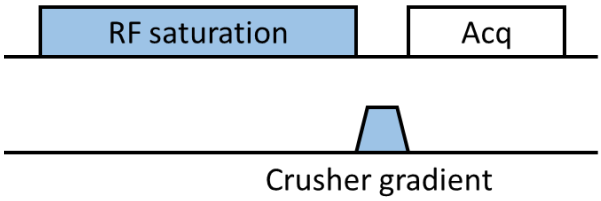

Figure 1-7 Schematic of CW saturation CEST.
The RF saturation is of constant amplitude. A crusher gradient follows the saturation to remove residual transverse magnetization before image acquisition. Acq: acquisition.

The advantage of CW saturation is that it is easy to optimize. There are only two parameters, t_{sat} and saturation amplitude/power, to be optimized. However, because CW saturation has high duty cycle and high specific absorption rate (SAR), it is not achievable in most clinical scanners. The experiment needs to be repeated at multiple RF frequencies, and can be time-consuming.

1.4.1.2 Pulsed saturation

To overcome the hardware limitation and satisfy SAR requirements for human CEST imaging, pulsed saturation is proposed in replacement of CW saturation (Figure 1-8). The pulsed saturation uses a train of shorter RF saturation pulses interleaved with delays, instead of a single, continuous, CW saturation. To destroy the transverse magnetizations, crusher gradients can be added either after each RF saturation pulse or at the end of the saturation pulse train. Pulsed saturation has many parameters to optimize (e.g. individual pulse

durations, inter-pulse delays, pulse shapes). Thus, optimization can be more complicated compared with the CW saturation. Similar to CW, acquisition of multiple RF frequencies increase total scan time.

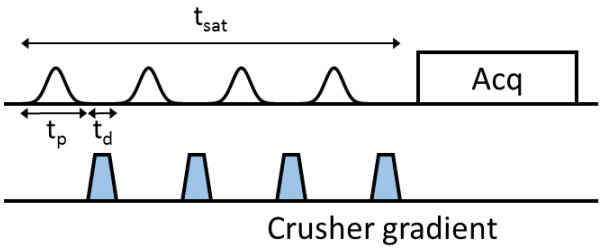

Figure 1-8 Schematic of pulsed saturation CEST.
The crusher gradient can be applied after each pulse or only applied once at the end of the saturation pulse train. t_p: pulse duration. t_d: inter-pulse delay. t_{sat}: saturation time. Acq: acquisition.

1.4.1.3 Segmented steady-state saturation

In the steady-state method, the saturation is long ($t_{sat} >> T_1$) to ensure the system is in the steady-state before the image acquisition. Hence the k-space is filled from the center to the outside. By contrast, the segmented steady-state method splits the long saturation into short parts with intermittent acquisitions (Figure 1-9). For each saturation-acquisition block, the $t_{sat} << T_1$ and the acquisition is for parts of the image, a single k-line or a few k-lines. Since the last saturation-acquisition block has the longest t_{sat} and hence, the highest CEST effect, the k-space is filled from the outside to the center. Compared with the pulsed steady-state method, the pulsed segmented steady-state method can be faster, especially for 3D acquisitions.

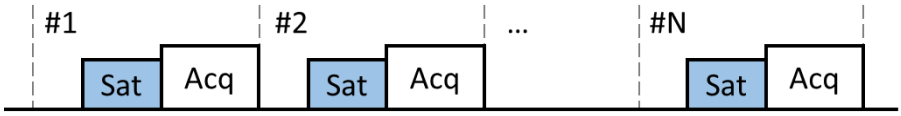

Figure 1-9 Schematic of segmented steady-state saturation CEST.
Sat: saturation module, can either be CW saturation or pulsed saturation. Acq: acquisition module.

For the segmented steady-state method, either full or partial excitation of the Z-magnetization to the transverse plane for image acquisition is required. As a result, the Z-magnetization is reduced after each pulse. However, if a gradient echo based acquisition is used, the majority of the z-magnetization remains along the z-axis, since low flip angle pulses are used for excitation.

1.4.2 CEST data analysis

1.4.2.1 MTR_{asym}

There are multiple ways to analyze data and generate CEST contrast. The most widely used method is the MTR_{asym} analysis as discussed in the Section 1.2.1. To a good approximation, MTR_{asym} removes contributions other than CEST that are symmetric around water frequency, such as direct water saturation. However, because MT is slightly asymmetric around water, MTR_{asym} can only remove MT to some extent. NOE is asymmetric in itself, thus can confound MTR_{asym} analysis. In addition, MTR_{asym} is sensitive to B_0 inhomogeneity, since the exact position of "0" water reference needs to be determined. Thus, to use MTR_{asym}, additional imaging sequences are needed to acquire B_0 information, such as B_0 mapping sequences and WASSR (41). However, separate B_0 mapping sequences has

problems. First, it increases the total scan time. Second, the sequences need to be set up carefully to ensure that the water frequency and the shimming conditions are the same as the CEST scans.

1.4.2.2 Other methods

Beside the MTR_{asym}, there are many other methods used for CEST data analysis. Among them, the apparent exchange-dependent relaxation (AREX), Lorentzian fitting and Bloch-McConnell Equations fitting are seen most often.

The AREX is proposed as a way to generate CEST contrast with T_1 relaxation effect corrected (42). The disadvantages of using AREX is similar to MTR_{asym}, it cannot decouple the contributions other than CEST.

The saturation curve of each pool can be represented by a Lorentzian line. Therefore, the multiple-pool Z-spectrum can be fitted using multiple Lorentzian lines. The advantages of Lorentzian fitting is that it can separate the contributions of each pool, hence remove the MT and NOE contributions from CEST effects. However, if no prior knowledge about where the leading CEST pools are, the fitting could be arbitrary. In most studies, the Lorentzian lines are added up, to form the Z-spectrum (43). Some studies also take the pool interactions indirectly through water pool into consideration (27). This increases the model complexity and hence is less used.

The Bloch-McConnell Equations fitting method can provide quantitative information such as exchange rate (25,44-46). However, fitting for a set of differential equations can be very time consuming, especially for multiple-pool systems.

1.5 ENDOGENOUS CEST APPLICATIONS

1.5.1 A marker of protein and metabolite concentration

Several published studies demonstrated the feasibility of CEST as an imaging marker of protein and metabolite concentrations, which has been applied to cancer, neurological diseases and neurodegenerative diseases. Here we list a few examples of different endogenous CEST sources and their applications.

The amide proton transfer (APT) is a sub-set of CEST. APT assumes that CEST effects originate predominantly from the amide groups in the backbones of proteins and peptides, resonating at 3.5 ppm from water. For example, one theory suggest that in the brain tumors, the intracellular protein concentration is elevated and results in higher APT signals in the tumors than in the normal brain tissues (2,47). It has been reported that the APT signal can be used to differentiate between high grade and low grade gliomas (48), tumor and edema (47), and tumor and radiation necrosis (49). In addition to brain cancer, APT has also been applied to breast (50) and prostate cancer (51).

Another example is CEST detection of glutamate, resonating at 3 ppm. Glutamate is a major excitatory neurotransmitter in the brain. The glutamate concentration is altered in many central nervous system (CNS) diseases, such as Alzheimer's disease, autism and schizophrenia. The glutamate CEST (gluCEST) is proposed as a method for in vivo mapping of glutamate (52,53) which can provide valuable information for both understanding and

treatment of the diseases. The CEST signal is from the amine group in the glutamate. It has been shown that lower gluCEST signals were observed in the Alzheimer's disease models (54).

Another example is detection of glycosaminoglycan (GAG), an important content in both cartilage and intervertebral disks (IVD). GAG has hydroxyl groups which can be detected by CEST at 1 ppm from water. GAG is associated with the maintenance of tissue fluid and hence its loss indicates damage or degeneration. The glycosaminoglycan CEST (gagCEST) is proposed as a method for in vivo mapping of GAG distribution. Lower gagCEST signals were observed in osteoarthritis (22) and IVD degeneration (55).

In addition to the above-mentioned applications, other applications utilizing different CEST signals have also been reported, such as amine CEST at 2 ppm to map creatine (CrCEST) as an indication for muscle energy metabolism (3,56,57), hydroxyl CEST at ~0.6 ppm to map myo-inositol (MICEST) in the brain for neurological diseases (58) and hydroxyl CEST at 1 ppm to map glycogen concentration in the liver (13).

1.5.2 A marker of pH

The intracellular and extracellular pH of the tissues are important to maintain normal functions. Altered pH is observed in many diseases: tumors have lowered extracellular pH due to glycolysis, and the pH is lowered in the stroke due to hypoxia. CEST is sensitive to pH because the exchange rate is pH dependent. In the physiological conditions ($6.5 < pH < 7.5$), most endogenous exchangeable protons are base-catalyzed. In other words, the

exchange rate increases as the pH increases. APT signal is ideal for in vivo pH measurement, because amide signals locate about 3.5 ppm downfield from water with an exchange rate on the order of several ten Hz, making the amide signal in the slow exchange regime. APT has been applied to both qualitative (59) and quantitative (8) pH measurements.

APT imaging of ischemic stroke is depended on APT's sensitivity to pH variation. The lowered pH in ischemic regions results in decreased APT signals compared with well perfused regions.

Measurement of the exchange rate can lead to quantitative pH via (60):

$$k_{sw} = k_a 10^{-pH} + k_b 10^{-pH-pK_w} + k_0 \qquad [1.29]$$

where k_a is the acid catalyzed exchange rate, k_b is the base catalyzed exchange rate, k_0 is the exchange rate of water with exchangeable protons, and pK_w is the water dissociation constant. Because most endogenous exchangeable protons are base-catalyzed in the physiological conditions, Equation 1.29 can be reduced to:

$$k_{sw} = k_b 10^{-pH-pK_w} \qquad [1.30]$$

Based on Equation 1.30, a curve of measured exchange rate versus pH can be established (8).

There are several methods that can be used to measure exchange rate, such as QUEST (61), QUESP (61) and Ω-plot (62). However, because the CEST measurement, such as MTR_{asym}, contains other confounding factors, from MT asymmetry and NOE, the exchange rate measurement is not precise. Hence, the pH derived via Equation 1.30 is not accurate. Therefore, most CEST applications related to pH are still qualitative.

CHAPTER TWO
An Alternative CEST imaging method: bSSFPX

2.1 OVERVIEW

The majority of this work was accepted for publication in the Journal of Magnetic Resonance 2017; 275:55-67. Portions of this work were presented at the 23rd annual meeting of International Society for Magnetic Resonance in Medicine (ISMRM) in Toronto, Canada (May 2015), the PENN-CEST in Philadelphia, PA, United States (October 2015), the 24th annual meeting of ISMRM in Singapore (May 2016), the 25th ISMRM in Honolulu, HI, United States (April 2017) and the Music City CEST in Nashville, TN, United States (August 2017).

CEST as a novel contrast mechanism is gaining popularity. Fast and quantitative CEST imaging techniques are further needed in order to increase the applicability of CEST for clinical use as well as to derive quantitative physiological and biological information. In this chapter, we observe that a balanced steady-state free precession (bSSFP) sequence in itself is sensitive to the exchange processes; hence, no additional saturation or preparation is needed for CEST-like data acquisition. The feasibility of bSSFP for exchange detection (bSSFPX) was verified both theoretically via Bloch-McConnell Equations simulations and experimentally in phantoms. Analytical models for bSSFPX were also developed for quantitative measurements of $T_{1\rho}$ and exchange rate. In a first in vivo experiment, bSSFPX was applied in the human brain to detect the chemical exchange possibly from fast

exchanging metabolites with resonance frequencies close to water that would be challenging at 3 T for standard CEST imaging methods.

2.2 INTRODUCTION

CEST as a new contrast mechanism in MRI is gaining popularity. However, a successful translation of CEST into clinical applications is hampered in part by its time-consuming acquisition as discussed in details in Section 1.4.1. Typically, the CEST pulse sequence utilizes a long saturation pulse followed by data acquisition. To correct for the artifacts due to B_0 inhomogeneity, and/or to acquire information about multiple exchanging sites, CEST often employs a series of off-resonance saturation pulses to acquire the so-called Z-spectrum. Moreover, exchange rate quantification methods that lead to metabolite distribution maps or pH measurements require several repetitions of the entire experiment with different saturation time or power (61). Hence, the already time-consuming whole Z-spectrum acquisition becomes even more time-consuming for exchange rate quantification and 3D CEST imaging. Therefore, seeking faster alternative ways for CEST data acquisition is highly desired.

Recently, steady-state methods for fast CEST imaging were reported, where the long saturation irradiation was split into short parts with intermittent acquisition (23). In the steady-state methods, the data acquired first (with shorter saturation time) fills the outer portion of the k-space and the data acquired later (with longer saturation time) fills the center of the k-space. By doing so, the acquisition time is shortened. The extreme case of this

approach would be a train of RF pulses with intervals for data acquisition. We observe that this is, in essence, a balanced steady-state free precession (bSSFP) sequence: a train of RF pulses interleaved with balanced gradients for image acquisition.

At the core of this project is the realization that the bSSFP sequence in itself is sensitive to the exchange processes, hence no additional saturation, preparation or separate detection pulses are needed to create the CEST effect. The bSSFP spectral profile is collected at multiple frequency offsets. The analysis of the profile provides information about the exchanging moieties, similar to CEST or off-resonance $T_{1\rho}$ experiments. This method, using bSSFP sequence for chemical exchange detection, is dubbed bSSFPX (bSSFP for eXchange detection). bSSFPX provides a new way for CEST data acquisition: the acquisition is performed during the saturation. Thus, it may speed up the CEST experiment. Also, the bSSFPX method should allow acquisition while the system approaches the steady-state, thus providing the data for QUEST-like quantification (61) in a "single-shot". Notably, in this method we are observing the XY-component of the magnetization and not the Z-component, as is standard in Z-spectroscopy.

Properties of equally spaced pulses have been investigated since the 1960s (63). Specifically, theory and experiments performed in solid-state NMR had shown that the train of equally spaced pulses creates an effective lock field, similar in its action to the CW lock (64-66). Two cases were thoroughly investigated: with same phase (65) and with 180° phase advance between the pulses (64). It has been shown that this pulsed spin lock affects the dipolar interaction in the way similar to the application of the CW irradiation.

Since the introduction by Carr in 1958 (67), the basic principles and theory of the steady-state signals (SSFP) generated by the repetitive pulses, has been explored in numerous publications, including the iconic work by Freeman *et.al.* (68). Since the introduction of SSFP imaging combined with balanced gradients (bSSFP), numerous studies investigated the sequence properties (69-81). To name a few examples, bSSFP was combined with inversion recovery to continuously acquire data for T_1 quantification (72). The sequence has been used for fast T_2 mapping (DESPOT2 (74)). The multicomponent T_1 and T_2 relaxation in bSSFP has been investigated (mcDESPOT (75)). Miller *et.al.* investigated asymmetries observed in bSSFP (82). Bieri and Scheffler have investigated properties of bSSFP to modulate magnetization transfer effects (83). However, to the best of our knowledge, this is the first time that the spin-locking and off-resonance saturation transfer properties of the imaging sequence are investigated, thus explicitly realizing and exploring the analogous nature of bSSFP and CEST/$T_{1\rho}$ experiments.

In this project, the ability of bSSFPX to create CEST-like effects was demonstrated by theoretical derivation, simulation and phantom studies. The bSSFPX method was first implemented in the steady-state (ss-bSSFPX) as a proof of principle. The results of an ss-bSSFPX experiment were compared with that of a standard pulsed CEST experiment. Next, the transient-state bSSFPX (ts-bSSFPX) method was implemented and validated in phantom studies. To lay the foundations for quantitative measurements of the bSSFPX method, the mathematical model was derived and compared with the Bloch-McConnell Equations simulations. At last, the ss-bSSFPX was tried in human brain. The results show that bSSFPX is a highly promising approach to achieve fast and quantitative CEST imaging.

2.3 THEORY

A basic repetitive n[th] unit of a bSSFP sequence is $\left[\alpha_{\phi_0+(n-1)\Delta\phi} - TR\right]$, where α is the flip angle, ϕ_0 is the phase of the first RF pulse and $\Delta\phi$ is the phase advance between two consecutive RF pulses. In a typical bSSFP experiment, $\Delta\phi = 0$ or π. Since the sequence consists of a number of the repeating basic units, the phase advance can be treated as the frequency offset by an amount $\Delta\phi/(2\pi TR)$ (84). In the bSSFP sequence, all the gradients are balanced over one TR. In other words, the net gradient over one TR is 0. Hence, the influence of gradients can be ignored and the evolution of magnetization at the echo times or the end of each unit is governed solely by RF (73). For simplicity and without loss of generality, the following derivations assume $\phi_0 = 0$ which makes the basic unit of the bSSFP sequence $\left[\alpha_{(n-1)\Delta\phi} - TR\right]$.

2.3.1 Effective field

First, consider the simplest case in which only one pool is present and TR << T_1 and T_2 hence the influence of relaxation can be ignored. In the absence of relaxation, the propagation of magnetization over one cycle is given by:

$$M_{n+1} = R_z(\theta) R_x(\alpha) M_n = R_e(\Phi) M_n = e^{H_{eff} TR} M_n \qquad [2.1]$$

where M_{n+1} and M_n are the magnetization vectors at the end of *n+1* and *n* cycle. $R_z(\theta)$ and $R_x(\alpha)$ are the standard z- and x-rotation matrices respectively. $\theta = \Delta\omega_w TR - \Delta\phi$ is the precession angle, where $\Delta\omega_w = \omega_w - \omega_{RF}$ is the off-resonance of water (84,85). The propagation of the magnetization is given by two consecutive rotations and thus, in accordance with Euler theorem, can be represented by a single rotation. The composite rotation is described by the directionality vector $\vec{e}$ and the rotation angle Φ. To be specific, $\vec{e}$ represents the axis of rotation about which M_n rotates by the angle Φ. Using the Euler parameters, the directionality vector and the rotation angle are:

$$\vec{e} = \begin{bmatrix} e_1 \\ e_2 \\ e_3 \end{bmatrix} = \vec{u}\sin(\Phi/2),\ e_0 = \cos(\Phi/2) \text{ with } \begin{array}{l} e_0 = \cos(\alpha/2)\cos(\theta/2) \\ e_1 = \sin(\alpha/2)\cos(\theta/2) \\ e_2 = \sin(\alpha/2)\sin(\theta/2) \\ e_3 = \cos(\alpha/2)\sin(\theta/2) \end{array} \qquad [2.2]$$

where $\vec{u} = (u_1, u_2, u_3)^T$ is the unit vector in the same direction as $\vec{e}$, hence $u_1 = e_1 / \sqrt{1-e_0^2}$, $u_2 = e_2 / \sqrt{1-e_0^2}$ and $u_3 = e_3 / \sqrt{1-e_0^2}$. In addition, using Equation 2.2, the angle Θ between the effective field and the z-axis can be found:

$$\cos(\Theta) = \frac{e_3}{\sqrt{1-e_0^2}} = \frac{\cos(\alpha/2)\sin(\theta/2)}{\sqrt{1-\cos^2(\alpha/2)\cos^2(\theta/2)}} \qquad [2.3]$$

Thus, the effective field is given by:

$$\gamma \vec{B}_{eff} = \frac{\Phi}{TR}\vec{u} = \omega_{eff}^{bSSFP}\vec{u} \qquad [2.4]$$

This is illustrated in Figure 2-1a. The effective field "strength" is given by:

$$\omega_{eff}^{bSSFP} = \frac{\Phi}{TR} \qquad [2.5]$$

i.e. precession over time TR will result in rotation by angle Φ.

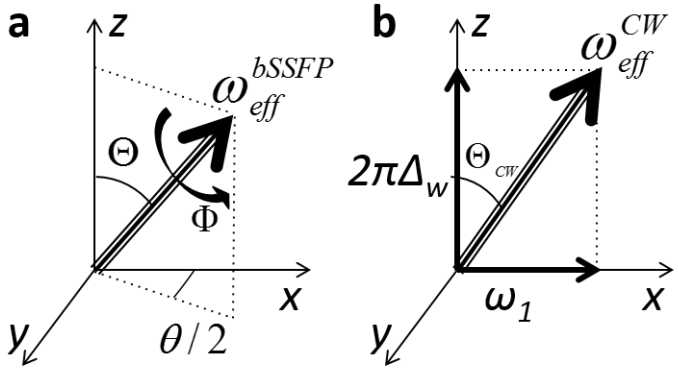

Figure 2-1 The effective fields of bSSFP and CEST/$T_{1\rho}$ experiments.
The effective fields generated during (a) bSSFPX experiment and (b) standard CEST/$T_{1\rho}$ experiment. In CEST/$T_{1\rho}$, the effective field depends on the RF off-resonance value, Δ_w, and RF intensity, ω_1. In bSSFP, the effective field can be described by two angles: Θ and Φ, that are functions of the flip angle, TR and off-resonance value used in bSSFP. $\theta/2$ is the angle between the x-axis and the projection of the effective field into the xy-plane.

This effective field governs the magnetization dynamics, in accordance with the Bloch Equations. The effective field in the bSSFP sequence can be written in matrix notation as:

$$H_{eff} = \sin(\Theta)\frac{\Phi}{TR} I_{xy} + \cos(\Theta)\frac{\Phi}{TR} I_z \qquad [2.6]$$

where I_x , I_y and I_z are the standard 3-dimentional space basis matrices and $I_{xy} = I_x \cos(\theta/2) + I_y \sin(\theta/2)$. An alternative form for H_{eff} using the components of $\vec{u}$ is given by:

$$H_{eff} = \frac{\Phi}{TR}\begin{bmatrix} 0 & -u_3 & u_2 \\ u_3 & 0 & -u_1 \\ -u_2 & u_1 & 0 \end{bmatrix} \qquad [2.7]$$

For comparison, in the standard CW spin-lock or saturation transfer experiment, the effective field can be written similar to Equation 2.4:

$$\gamma \vec{B}_{eff}^{CW} = \omega_{eff}^{CW} \vec{u}_{CW} \qquad [2.8]$$

where the effective field strength is given by $\omega_{eff}^{CW} = \sqrt{\omega_1^2 + \omega_w^2}$ as shown in Figure 2-1b. In the CW case, the directionality vector is $\vec{u}_{CW} = \left(\sin\Theta_{CW}\cos\varphi,\ \sin\Theta_{CW}\sin\varphi,\ \cos\Theta_{CW}\right)^T$, with $\Theta_{CW} = \arctan\left(\omega_1/\omega_w\right)$ where ω_1 is the RF intensity and φ is the RF phase. In the most common case the RF is along x axis with $\varphi = 0$ (Fig. 2-1b).

Comparison between Equations 2.4 and 2.8 demonstrates the complete analogy between bSSFP and CW application (as illustrated in Fig. 2-1). The key difference is: while in the CW case the effective field strength as a function of off-resonance is a non-periodic function (Eq. 2.8), in the bSSFP case (Eq. 2.4) it is cyclic with the period $2\pi/TR$ (as can be seen from Φ dependence on α and θ in Eq. 2.2). Thus, it will lead to RF profile with multiple saturation bands, the known characteristic of bSSFP profile.

2.3.2 Relaxation influence

In the presence of relaxation, the magnetization dynamic becomes more complex. In general, based on the Bloch Equations, the magnetization equation over one cycle becomes:

$$M_{n+1} = e^{(H_{eff}-\tilde{R})TR} M_n - \left[I - e^{(H_{eff}-\tilde{R})TR} \right] \left(H_{eff} - \tilde{R} \right)^{-1} R_1 M_0 \qquad [2.9]$$

where $R = \mathrm{diag}\left(R_2, R_2, R_1 \right)$ is standard relaxation matrix (86). The above equation can be used to assess transient as well as steady-state magnetization. In the steady-state, Equation 2.9 reduces to:

$$M_{ss} = - (H_{eff} - \tilde{R})^{-1} R_1 M_0 \qquad [2.10]$$

However, it is more instructional to observe what happens in the interaction frame defined by the eigensystem of the effective RF field, $\gamma \vec{B}_{eff}$. It is also more exact, since in the presence of RF, the standard concepts of R_1 and R_2 relaxation do not properly describe magnetization dynamics. Instead, it is more appropriate to use the relaxation in the RF interaction frame, which also consists of two components, parallel and perpendicular to the effective field, $R_{||}$ or $R_{1\rho}$ and $R_{\perp}$ or $R_{2\rho}$ respectively (87). Using analogy with the effective field in the spin-lock experiment, as discussed in the Section 1.3.1, the two relaxation components are (88):

$$\begin{aligned} R_{1\rho} &= \cos^2(\Theta) R_1 + \sin^2(\Theta) R_2 \\ R_{2\rho} &= \sin^2(\Theta) R_1 + \cos^2(\Theta) R_2 \end{aligned} \qquad [2.11]$$

Using these two relaxation components the steady-state magnetization becomes:

$$M_{ss} = -D\Lambda^{-1}D^{-1}R_1 M_0 \qquad [2.12]$$

where *D* is the diagonalization matrix of the H_{eff}, which is composed of eigenvectors of H_{eff}:

$$D = \begin{bmatrix} u_1 & \frac{-u_1u_3 + iu_2}{\sqrt{2\left(1-u_3^2\right)}} & \frac{-u_1u_3 - iu_2}{\sqrt{2\left(1-u_3^2\right)}} \\ u_2 & \frac{-u_2u_3 - iu_1}{\sqrt{2\left(1-u_3^2\right)}} & \frac{-u_2u_3 + iu_1}{\sqrt{2\left(1-u_3^2\right)}} \\ u_3 & \sqrt{\frac{1-u_3^2}{2}} & \sqrt{\frac{1-u_3^2}{2}} \end{bmatrix} \quad [2.13]$$

and Λ is the diagonal matrix:

$$\mathsf{L} = \begin{bmatrix} -R_{1r} & 0 & 0 \\ 0 & -R_{2r} - i\mathsf{F}/TR & 0 \\ 0 & 0 & -R_{2r} + i\mathsf{F}/TR \end{bmatrix} \quad [2.14]$$

Λ is the subtraction of two diagonal matrixes: $\Lambda = \Lambda_{eff} - \Lambda_R$. After diagonalization, $H_{eff} = D\mathsf{L}_{eff}D^{-1}$ with Λ_{eff} the diagonal matrix composed of the eigenvalues of H_{eff}:

$$\Lambda_{eff} = \begin{bmatrix} 0 & 0 & 0 \\ 0 & -i\frac{\Phi}{TR} & 0 \\ 0 & 0 & i\frac{\Phi}{TR} \end{bmatrix} \quad [2.15]$$

The relaxation matrix R can be presented in the eigensystem of the effective field as well:

$$\tilde{R} = D\Lambda_R D^{-1} \quad [2.16]$$

Analogous to the effective field in the spin-lock experiment, the off-diagonal values in Equation 2.16 are ignored and Λ_R becomes:

$$\Lambda_R = \begin{bmatrix} R_{1\rho} & 0 & 0 \\ 0 & R_{2\rho} & 0 \\ 0 & 0 & R_{2\rho} \end{bmatrix} \quad [2.17]$$

where $R_{1\rho}$ and $R_{2\rho}$ are found in Equation 2.11. Hence,

$$H_{eff} - R = D\left(\Lambda_{eff} - \Lambda_R\right)D^{-1} = D\Lambda D^{-1} \quad [2.18]$$

In the core, Equation 2.12 describes the transformation to the H_{eff} eigensystem where the steady-state is described by the eigenvalues of the effective field 0, $\pm i\Phi / TR$ as well as by the two appropriate relaxation components $R_{1\rho}$ and $R_{2\rho}$.

Based on the Equations 2.9 and 2.12, the time-dependent or transient magnetization can be derived:

$$M_n = M_{ss} + De^{\Lambda \cdot nTR}D^{-1}\left(M_0 - M_{ss}\right) \quad [2.19]$$

2.3.3 Two pools with exchange

This discussion is confined to the two-pool system (bulk water pool denoted “w” in subscript and solute pool denoted “s” in subscript) only, at the slow exchange regime, although the generalization to larger number of pools and other exchange regimes is possible. In the presence of two exchanging pools, Equation 2.11 is expanded to include the contribution of exchange in the relaxation terms. In the previous sections, the analogy between bSSFP and spin-lock experiment is demonstrated. Thus, the exchange contribution to relaxation rates can be evaluated using expressions derived for the spin-lock experiment

(31,32,89). Since the water signal is what we are measuring, the R_{ex} term, the contribution of exchange to the relaxation rate, for the water pool only is presented and follows Trott and Palmer's work (31) assuming asymmetric population limit (i.e. water pool fraction is much greater than the solute). Thus, in the presence of exchange, Equation 2.11 becomes:

$$\begin{aligned} R_{1\rho,w} &= \cos^2(\Theta) R_{1,w} + \sin^2(\Theta)(R_{2,w} + R_{ex,w}) \\ R_{2\rho,w} &= \sin^2(\Theta) R_{1,w} + \cos^2(\Theta)(R_{2,w} + R_{ex,w}) \end{aligned} \qquad [2.20]$$

with

$$R_{ex,w} = \frac{p_w p_s \Delta_{ws}^2 k}{\left(\omega_{eff,s}^{bSSFP} / 2\pi\right)^2 + k^2} = \frac{p_w p_s \Delta_{ws}^2 k}{\Phi_s^2 / (2\pi TR)^2 + k^2} \qquad [2.21]$$

in which $p_j = M_{0j} \Big/ \sum_m M_{0m}$ is the population fraction of each pool; $\Delta_{ws} = \delta_w - \delta_s$ is the chemical shift difference between the two pools and $k = k_{ws} + k_{sw}$ is the exchange rate. In Equation 2.21, Equation 2.4 is used to express the effective field of the solute pool ($\omega_{eff,s}^{bSSFP}$) in terms of the precession angle Φ and the repetition time TR.

Note that while the form of $R_{ex,w}$ contribution to $R_{1\rho,w}$ in the spin-lock and saturation transfer experiments is widely discussed, the similar contribution to $R_{2\rho,w}$ has not been addressed as thoroughly. To the best of our knowledge, only work by Michaeli, *et.al.* (90) explicitly discusses the form of $R_{ex,w}$ contribution to $R_{2\rho,w}$ in the presence of adiabatic RF pulses. Hence, the same form of $R_{ex,w}$ for both, $R_{1\rho,w}$ and $R_{2\rho,w}$ is assumed in Equation 2.20.

For bSSFPX, the Equation 2.21 predicts that the exchange contribution is maximal when the rotation angle $\Phi_s = 0, 2\pi, ..., n2\pi$, making the lock field effectively zero for the

solute pool. For small flip angles, this translates to the following condition for the solute off-resonance:

$$\Delta_s = \frac{n - \Delta\phi / 2\pi}{TR} \qquad [2.22]$$

This implies that the exchange contribution is maximal when the pulse train is exactly on-resonance with the solute pool or a multiple of 1/TR off-resonance with respect to the water pool. In other words, when the bSSFP saturation is "on-resonance" with the solute, the maximum saturation is achieved. This is indeed similar to the standard CEST case, with the caveat of the repetitive pattern with 1/TR embedded in the bSSFP train.

Higher flip angle α prevents Φ from reaching $n2\pi$, as demonstrated in Figure 2-6c. However, the condition for general minimum of R_{ex} remains in agreement with Equation 22, as is evident from Figure 2-6a and b. Additional discussion of the influence of the flip angle is conducted in the next sections.

As demonstrated in the following, Equations. 20-22 provide a correct qualitative prediction of the observed behavior of the exchanging system.

2.4 METHODS

2.4.1 Simulation

Numerical simulations were performed in MATLAB 8.4 (The Mathworks, Natick, MA) to 1) validate the theoretical derivations and 2) compare the Z- and XY-spectrum and

their corresponding MTR_{asym} of the bSSFPX with that of the standard CW CEST. The simulations were based on a two-pool Bloch-McConnell model (26). Unless stated differently, the simulation parameters were M_{0w} = 1, T_{1w} = 2 s, T_{2w} = 0.05 s, M_{0s} = 0.05, T_{1s} = 1 s, T_{2s} = 1 s. Variety of chemical shifts and exchange rates was investigated: Δ_{ws} = 1 to 9 ppm, k_{sw} = 0 - 4000 Hz. For the bSSFPX sequence, the rectangular pulses with duration τ = 25 μs and initial phase $\phi_0 = 0°$ were used; the interpulse delay was set to 2 ms (TR = 2.025 ms is the sum of the pulse duration and interpulse delay) and the number of prep-echoes was set to 4096. This was equivalent to an 8.2944 second saturation. Range of flip angles was investigated. The flip angle can be translated to $B_{1,CW}$ using the formula: $B_{1,CW} = \int_0^{TR} B_1(t)\,dt \Big/ TR = \alpha \Big/ (360° \gamma TR)$ (82). For TR ≈ 2 ms used in the simulations, α = 10º, 30º, 45º, 60º, 90º translates to $B_{1,CW}$ = 0.33 μT, 0.98 μT, 1.47 μT, 1.96 μT, 2.94 μT, respectively. No preparation methods were used to smooth the transient-state signals since the magnetization was observed in the steady-state. The offset frequencies were from -500 Hz to 500 Hz with 10 Hz increments. A CW CEST sequence comparable to the bSSFPX sequence, with the saturation duration of 8.2944 s and $B_{1,CW}$ = 0.97 μT, was also simulated. All the simulations assumed a field strength of 3 T.

2.4.2 Phantom

Choline (Sigma-Aldrich, CAS no. 67-48-1), glucose (Research Products International Corporation, CAS no. 50-99-7) and glycogen (Sigma-Aldrich, CAS no. 9005-79-2) water solutions all at the concentration of 100 mM were prepared (phantom I). In addition, choline

water solutions with concentrations 10, 25, 50 and 100 mM were prepared (phantom II). These solutions were transferred to glass vials held together in a glass container. The outer glass container was filled with fomblin oil (Ausimont, Thorofare, NJ) to minimize the field inhomogeneity and susceptibility effects. A 2% agar (Research Products International Corp., CAS no. 9012-36-6) phantom with 0.14 mM gadolinium was also prepared (phantom III).

2.4.3 In vivo study

Three healthy volunteers were recruited for the study. The study was approved by the local institutional review board, and were performed in accordance with the guidelines. Written informed consent was obtained from each subject.

2.4.4 MRI

All the MRI data were acquired on a 3 T whole-body human scanner (Ingenia, Philips Healthcare, Best, the Netherlands). The 2D imaging sequences of ss-bSSFPX and ts-bSSFPX are shown in Figure 2-2. For the ss-bSSFPX sequence (Fig. 2-2a), only one image is acquired at the end of the pulse train. The pulses prior to data acquisition act as prep-echoes to drive the spin system to a steady-state. By contrast, the data acquisition is always on throughout the entire ts-bSSFPX sequence (Fig. 2-2b).

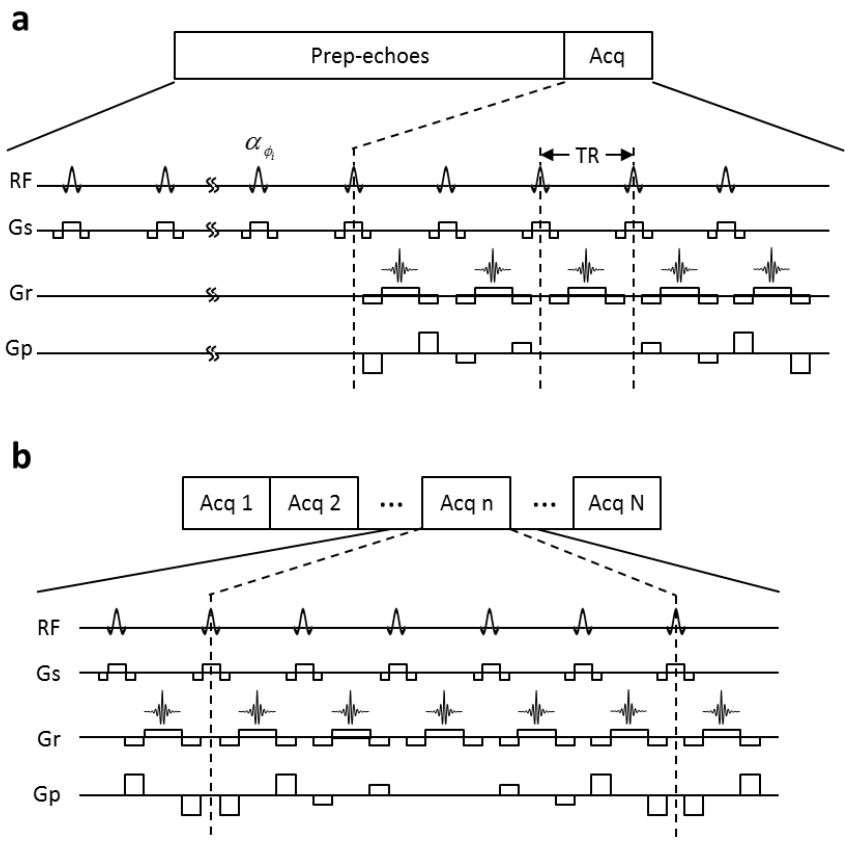

Figure 2-2 Schematic for the 2D bSSFPX pulse sequence.
(a) steady-state bSSFPX (ss-bSSFPX) sequence and (b) transient-state bSSFPX (ts-bSSFPX) sequence. Prep-echoes: preparation echoes needed to reach the steady-state. Acq: acquisition. Gs: slice selection gradients. Gr: readout gradients. Gp: phase encoding gradients.

The phantom scans were performed at room temperature using a 15-channel head-spine coil for both ss-bSSFPX and ts-bSSFPX. The 2D ss-bSSFPX images were acquired using a standard bSSFP sequence with 3500 prep-echoes, $\alpha = 40^{o}$, TR/TE = 2.2/1.1 ms and linear k-space ordering. This was equivalent to a 7.7 second saturation with $B_{1,CW} = 1.19$ μT. No preparation methods were used to smooth the transient-state signals, since the steady-state signals were the focus at this proof-of-principle step. The RF offsets (realized via phase advance (76)) were from -500 Hz to 500 Hz with 10 Hz increments for increasing frequency

sweep and from 500 Hz to -500 Hz with 10 Hz decrements for decreasing frequency sweep. The final profile was the average of the two profiles acquired with reverse frequency sweeps (see Section 2.4.5). Geometric parameters were field of view (FOV) = 200 × 200 mm^2, voxel size = 3-by-3 mm, slice thickness = 8 mm and reconstructed matrix size = 256. It took 8.0 s per irradiation frequency and 13 min 30 s for a whole profile acquisition. For comparison, the 2D pulsed CEST images were also acquired using the same $B_{1,CW}$ as the bSSFPX experiment and the longest saturation time that can be achieved within SAR limitation. The saturation pulse train consisted of 98 hyperbolic secant (HS) pulses with duration 50 ms, no interpulse delay and flip angle 909º. To achieve this 100% RF duty cycle, the alternated parallel transmission (pTx) is needed (91). The total saturation length was 4.9 s and the equivalent $B_{1,CW}$ was 1.19 μT. A single-shot turbo spin echo (TSE) readout was used for image acquisition. For phantom I, 45 images were acquired from -900 Hz to 900 Hz with 40 Hz increments. For phantom II, 41 images were acquired from -500 Hz to 500 Hz with 25 Hz increments. Geometric parameters were FOV = 200 × 200 mm^2, slice thickness = 8mm, reconstructed matrix size = 256. For phantom I: TR/TE = 5691/5.2 ms, voxel size = 3-by-3 mm, the total Z-spectrum acquisition lasted 4 min 33 s with 5.7 s per irradiation frequency and for phantom II: TR/TE = 5666/4.9 ms and voxel size = 1.5-by-1.5 mm, the total acquisition lasted 4 min 3 s with 5.7 s per irradiation frequency. A reference image was acquired at -200 kHz. The Z-spectrum was corrected for B_0 inhomogeneity using the WASSR (41) technique. Additional B_0 drift correction is required on our scanner by adding an overall constant value to the B_0 maps. The WASSR sequence was essentially the same as the CEST sequence but with shorter and weaker saturation. It contained 2 HS pulses with the

same duration and interpulse delay as the CEST sequence but with flip angle 100º. 41 WASSR images were acquired from -200 Hz to 200 Hz with 10 Hz increments using the same geometric parameters and acquisition parameters as the CEST, except TR = 3000 ms and 1522 ms for phantom I and II respectively thus shorter total acquisition times. Second-order shimming was used in all experiments.

The 2D ts-bSSFPX images were acquired using a standard bSSFP sequence with α = 40º, TR/TE = 2.0/1.0 ms, voxel size = 3-by-3 mm, slice thickness = 8 mm, half alpha startup echoes. 51 points in the XY-spectrum were acquired at the frequency range ±500 Hz. 20 images (corresponding to different saturation times) were acquired at each off-resonance frequency. Since the number of phase encoding lines was 73 and the linear k-space ordering was used, the effective saturation time for the i^{th} image t_{sat} = [37+(i-1)*73]*TR. Thus the shortest effective t_{sat} = 74 ms and the longest effective t_{sat} = 2.848 s.

The human scans were performed using a 32-channel head coil. For the first subject, 2D axial images were acquired. For the other two subjects, 2D oblique axial images were acquired to better visualize the corpus callosum. For all the subjects, the images were acquired using a single-shot bSSFP sequence, with α = 15°, TR/TE = 2.2/1.1 ms. Two full cycles from -500 to 500 Hz with ±25 Hz increment were acquired, resulting in 41 points in the bSSFP profiles. The other imaging parameters included FOV = 220 × 220 mm^2, voxel size = 3-by-3 mm (leading to 73 k-space lines), slice thickness = 8 mm. The high-low k-space ordering was used for Subject 1 and linear for the other subjects. Therefore, the longest effective t_{sat} = 2.4 s (Subject 1) and 2.3 s (Subject 2 and 3).

2.4.5 Data processing

All data were processed using custom MATLAB codes. The pulsed CEST and the bSSFPX data were analyzed on a pixel-by-pixel basis. The bSSFPX analysis followed the procedures analogous to the common CEST analysis leading to MTR_{asym}. It also incorporated procedures used in bSSFP processing (82).

First, the bSSFPX profiles were fitted to a single-pool steady-state bSSFP profile (68) to determine the B_0 shift. The shift consisted of two parts 1) B_0 inhomogeneity and 2) B_0 drift. Phantom susceptibility variation and imperfect shimming caused the former. bSSFP is a sequence with intense gradients. Hence the gradient coil heating up during the scan changes the shimming gradually (92), causing the drift. The profiles were realigned according to the amount of their cumulative B_0 shift, following procedure analogous to the one used in Ref (82).

As mentioned in the earlier sections, the long prep-echo train in an ss-bSSFPX sequence was to ensure that the image acquisition occurs in the steady-state. However, the T_1 of the liquid samples is long. As a result, residual transient effects may persist if the preparation length is not sufficiently long and cause asymmetries in the bSSFP profile. Specifically, if the signal at the center k-space originates from both, the transient state and the steady-state, the resulting profile is asymmetric; if only the signals in the steady-state contributed to the center of k-space, the resulting profile is symmetric (82). The preparation length was 7.7 s in the phantom experiment, which could not guarantee steady-state for all spins ($T_{1w} \approx 3.0$ s). However, the asymmetry caused by transient effects will be “mirrored”

upon the reverse of the direction of frequency sweep. Thus, the profiles acquired at reverse frequency sweeps are averaged to correct for this unwanted asymmetry to some degree.

Lastly, asymmetry of the XY spectra was calculated and normalized to the values at negative frequencies ($bSSFPX_{asym}$). Normalization by the negative frequencies is used instead of by reference, because XY-components were observed here and no reference image can be generated.

Standard Z-spectra acquired using pulsed saturation were processed using standard methods with WASSR correction for B_0 inhomogeneity. Then the Z-spectra were interpolated (shape-preserving piecewise cubic interpolation) for MTR_{asym} calculation. The MTR_{asym} was normalized to the negative frequencies, to be analogous to bSSFPX. Region of interests (ROIs) were manually drawn on the images. Both the $bSSFPX_{asym}$ and MTR_{asym} were averaged across each ROI in the frequency range 100-150 Hz to compare the bSSFPX with the standard pulsed CEST method.

2.5 RESULTS AND DISCUSSION

2.5.1 Proof of principle

2.5.1.1 Simulation validation

In Figure 2-3, two-pool simulations using standard CW (Fig. 2-3a-c) and bSSFPX (Fig. 2-3d-f) sequences are shown, displaying representative bSSFPX spectra and comparing the magnetization profiles between the two techniques. Only the signals from the water pool

are shown. In the simulations, different exchange rates were investigated. To guarantee that the spins were in the steady-state when the spectra were acquired, the total length of the saturation for both sequences was set to 8.2944 s, which is about 4 times longer than the maximum T_1 of the two pools. The shallow dips in the spectra (marked by the vertical solid lines) were caused by the CEST effect while the deep dips were caused by direct water saturation. As expected for the zero-degree initial phase, these saturation/dark bands or water dips are occurring at n/TR ≈ n × 500 Hz (with n being an integer, and 1/TR = 1/2.025 ms ≈ 500 Hz). Overall, the profiles for CEST and bSSFP around zero frequency are similar (Fig. 2-3a, b versus d, e); however, they start to quickly deviate from each other at higher frequencies, when the repetitive nature of bSSFPX becomes apparent. Despite the differences, it is evident from the figures that bSSFP displays similar behavior to CW. Moreover, there are some similarities with ZAPI (93) experiments or with dual saturation experiments (94,95).

The spectra in Figure 2-3 with zero exchange rate (i.e. no exchange between the pools), are equivalent to the single water-pool spectra. These spectra are symmetric about the water saturation band at zero frequency. In agreement with the Equations 2.20 and 2.22, the bSSFP pulse train creates saturation of the solute pool when the solute offset is on-resonance with one of the bands: $\Delta_w = \Delta_{ws} + \Delta_s \approx 200 + n500\,\mathrm{Hz}$. Thus, in the cases with nonzero exchange, the asymmetric dips in water magnetization are observed. The dips increase as the exchange rates increase for both, bSSFP and CEST, since higher exchange rate translates to better saturation transfer (25,26). The similarities of the spectra between the two sequences imply that the bSSFPX method has the potential to be used as a CEST experiment sequence.

Note that in bSSFPX the M_{xy} magnetization (Fig. 2-3e) is observed, and not the M_z as in standard CEST experiment (Fig. 2-3a). Thus, the absolute signal intensity might be lower (Fig. 2-3a versus e). At the same time, bSSFP has highest signal-to-noise ratio (SNR) among fast gradient-echo based sequences (96), so when acquisition influence is taken into account, this may not lead to a disadvantage of bSSFPX.

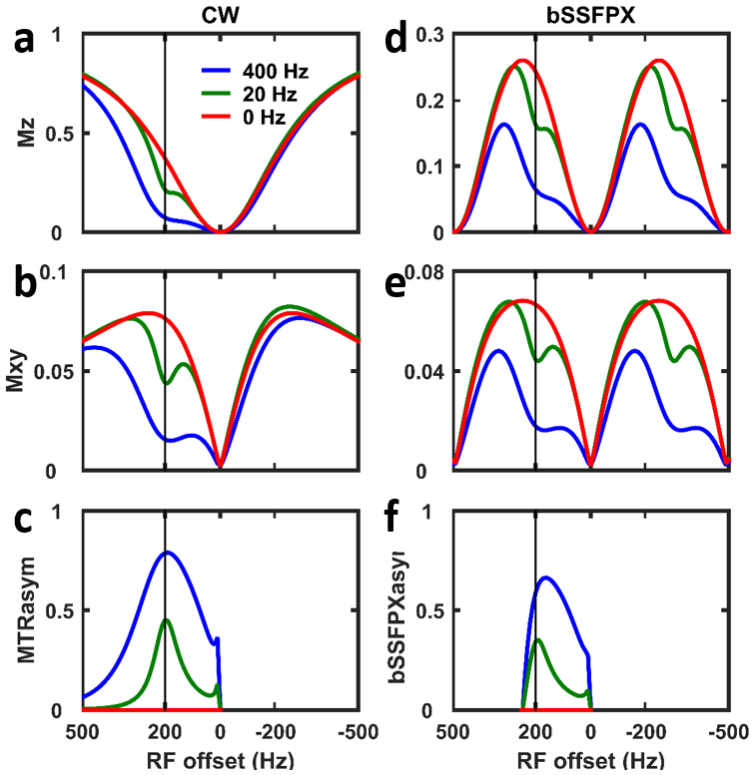

Figure 2-3 Two-pool simulation for CW and bSSFPX.
Two-pool simulation for (a-c) CW and (d-f) bSSFPX methods assuming different exchange rates: 0 (red), 20 Hz (green) and 400 Hz (blue). (a,d) Z-spectra of the water pool; (b,e) XY-spectra of the water pool; (c) MTR_{asym} and (f) $bSSFPX_{asym}$. Two periods of the bSSFPX profile are shown. The vertical line indicates the resonance frequency of the solute pool.

Figure 2-3c and f compares the signal asymmetry for both sequences, MTR_{asym} versus $bSSFPX_{asym}$. The asymmetry of XY-component is equivalent to the asymmetry of the Z-

component (97): XY-MTR_{asym} = Z-MTR_{asym} and XY-$bSSFPX_{asym}$ = Z-$bSSFPX_{asym}$, hence only XY is shown. For both exchange rates shown here, the observed MTR_{asym} is higher than $bSSFPX_{asym}$ (~45% versus 35% and 79% versus 59% for k_{sw} of 20 Hz and 400 Hz, respectively). This indicates that the $bSSFPX_{asym}$ is lower than the CW MTR_{asym}, signifying that the CEST contrast obtainable using bSSFPX is lower than the one using CW sequence. It should be noted that CW saturation achieves maximum possible saturation, which is not achievable on many clinical scanners, where pulsed saturations have to be used with duty cycles lower than 100%. Thus, the true decrease in the CEST effects would depend on the specifics of the implementation of the "standard" CEST used for comparison. Here we compare bSSFPX to the maximum CEST scenario, not always achievable in practice.

To further investigate the influence of the system parameters (exchange rate and chemical shift difference) and experimental parameters (flip angle and associated $B_{1,CW}$) we have conducted a series of simulations. Figure 2-4 shows the representative bSSFPX profiles with different chemical shift differences Δ_{ws} = 1, 3, 9 ppm and exchange rates from slow to fast exchange regime with $k_{sw} = 0.5\Delta_{ws}$, Δ_{ws}, $2\Delta_{ws}$, $3\Delta_{ws}$, $5\Delta_{ws}$. For better illustration, the profiles in Figure 2-4 are shown using $\alpha = 10°$ which is translated to $B_{1,CW} \approx 0.32$ μT assuming TR = 2.025 ms. The flip angle and B_1 influences will be discussed in the following. For small chemical shift difference (Fig. 2-4a), less than 0.5/TR, bSSFPX spectra and asymmetry behaves very similar to the standard CEST. A clear dip in the spectrum can be seen for the slow exchange, and it becomes shallow and shifts toward water/saturation bands at n/TR as exchange rate increases. The trend is also reflected by the $bSSFPX_{asym}$: it decreases and shifts toward water/saturation bands as exchange rate increase (Fig. 2-4b). For

the fixed $B_{1,CW}$, the asymmetry for certain chemical shifts as a function of the exchange rate increases until reaches a maximum value and starts decreasing (Fig. 2-4g). The bSSFPX profiles and $bSSFPX_{asym}$ simulated using $\alpha = 30°$ and 45° has the similar trend. The results are not shown here. They can be found in the Supplementary of Ref. (97).

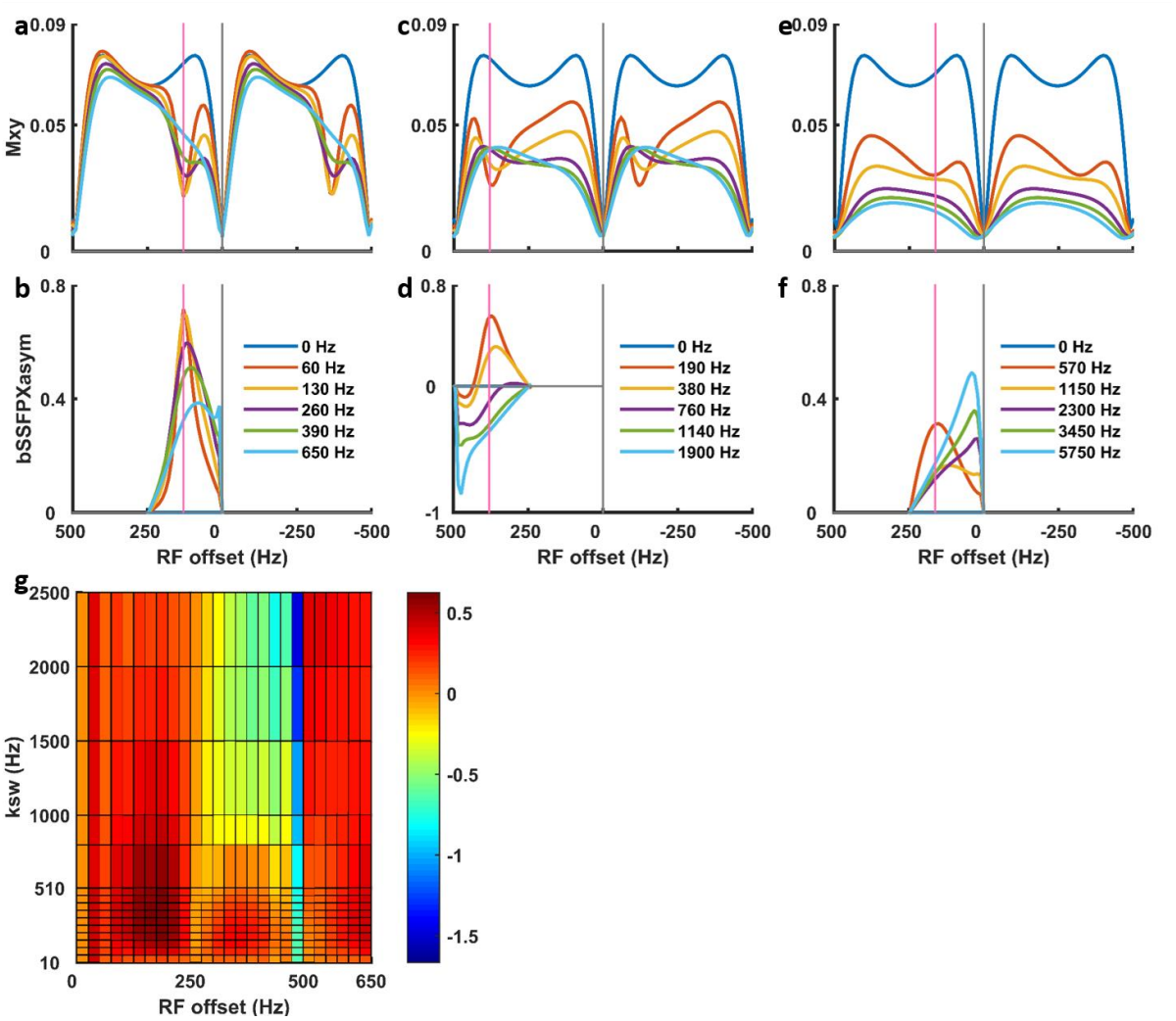

Figure 2-4 Simulated bSSFPX profiles and $bSSFPX_{asym}$ with different chemical shift differences and exchange rates.

Two-pool simulations of bSSFPX profiles (a, c, e) and corresponding $bSSFPX_{asym}$ (b, d, f) for $\Delta_{ws} \approx 1, 3, 9$ ppm, exchange rates from slow to fast exchange regime with $k_{sw} = 0.5\Delta_{ws}$, Δ_{ws}, $2\Delta_{ws}$, $3\Delta_{ws}$, $5\Delta_{ws}$. For better illustration, the profiles are shown using $\alpha = 10^{o}$ ($B_{1,CW} \approx$

0.32 μT with TR = 2.025 ms). Panel (g) shows $bSSFPX_{asym}$ as a function of k_{sw} and Δ_{ws} for $\alpha = 45^{o}$ ($B_{1,CW} \approx 1.45$ μT with TR = 2.025 ms).

When the chemical shift difference increases, the overall profile behaves similar to the small shift discussed above. The well-defined peaks at low exchange rates decrease, broaden and shift towards water saturation bands and eventually disappear. This is again, overall similar to the behavior in the standard CEST experiment. However, there are some important differences. First, due to saturation bands, if Δ_{ws} = n/TR, the CEST dips are not observed at all, since all the magnetization is suppressed, equivalent to the saturating at exactly water frequency in standard experiment (Fig. 2-5b). Moreover, our current analysis employs asymmetry, so that when $\Delta_{ws} \geqslant 0.5$/TR, the analysis underperforms. For example, if the chemical shift difference is exactly Δ_{ws} = n0.5/TR, the asymmetry analysis leads to complete cancellation of the exchange effects, regardless of the exchange rate (Fig. 2-4g and Fig. 2-5a). Away from these two obviously bad conditions (Δ_{ws} = n/TR and Δ_{ws} = n0.5/TR), when the chemical shift increases $0.5/TR < \Delta_{ws} < 1/TR$, the asymmetry analysis leads to negative asymmetry, as seen in Figure 2-4d. Finally, if the chemical shift is larger than 1/TR, the CEST dip will fold back, as is seen in an example in Figure 2-4e, f. Thus, if the simplest asymmetry analysis is used, chemical shift difference should be limited to less than 0.5/TR. In the future, more sophisticated analysis methods could be adopted similar to standard CEST, such as multi-peak and Bloch simulation fittings (50,98). However, currently, we anticipate that the bSSFPX results will be easiest to interpret for the CEST agents with small chemical shift difference, such as choline, glycine, glycogen or glycosaminoglycan.

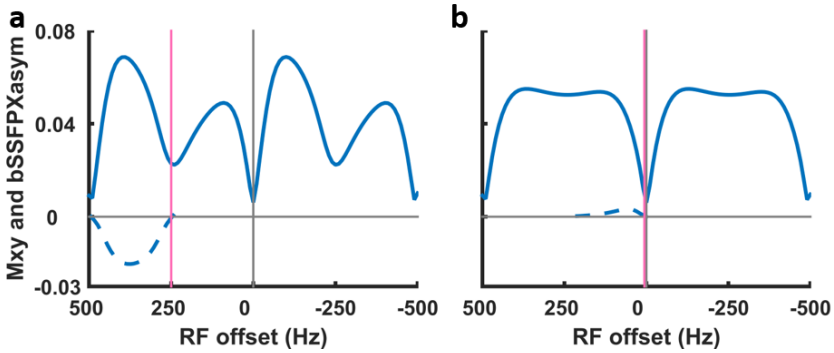

Figure 2-5 Simulated bSSFPX profiles and bSSFPX$_{asym}$ for two special conditions. Two-pool simulations of bSSFPX profiles (solid line) and corresponding bSSFPX$_{asym}$ normalized to the water pool size (dotted line) for Δ_{ws} = 250 Hz (a) and 500 Hz (b). For TR = 2.025 ms, Δ_{ws} = 250 Hz is about one half cycle and 500 Hz is about one full cycle. In the simulation, k_{sw} = 250 Hz and $\alpha = 10^{o}$, other simulation parameters are the same as described in the Section 2.4.1.

Next, the influence of the flip angle α is investigated. From Equations 2.2 and 2.3, the angle affects both, the directionality and the strength of the effective field. For the easier comparison with standard CEST, flip angle can be translated to $B_{1,CW}$, by taking TR into the account, as described in the Methods section. The dependence of the bSSFP spectrum intensity on the flip angle, and thus SNR is well investigated (73). However, in the presence of exchange, the flip angle will also affect asymmetry, and thus contrast-to-noise ratio (CNR). Figure 2-6a, b demonstrates the bSSFPX dependence on α. While the exchange parameters are the same for Figure 2-6a and b, the T_{2w}/T_{1w} ratio is different: 0.83 versus 0.025 ("large" and "small" in the following). From the SNR perspective, the optimal flip angle is different: ~90^{o} for the "large" T_{2w}/T_{1w} and ~20^{o} for the "small".

The flip angle will affect the exchange contribution R_{ex} (Eq. 2.21) via effective field strength and corresponding rotation angle Φ_s. As was discussed in the theory section, the maximum exchange contribution is obtained when $\Phi_s = n2\pi$ (effective zero rotation) which

translates to the Equation 2.22. Figure 2-6d illustrates dependence of Φ_s on α and θ: the figure displays $\cos(\Phi_s)$ and maxima correspond to $\Phi_s = n2\pi$. The figure demonstrates that while for smaller α almost perfect zero rotation is achieved, for larger α it is unattainable. Thus, the efficiency of saturation may actually decrease with higher flip angles. In addition, higher flip angle translates to higher $B_{1,CW}$ and to increased direct saturation, similar to standard CEST. This is further explored in Figure 2-6c, where the $bSSFPX_{asym}$ is shown as a function of the flip angle.

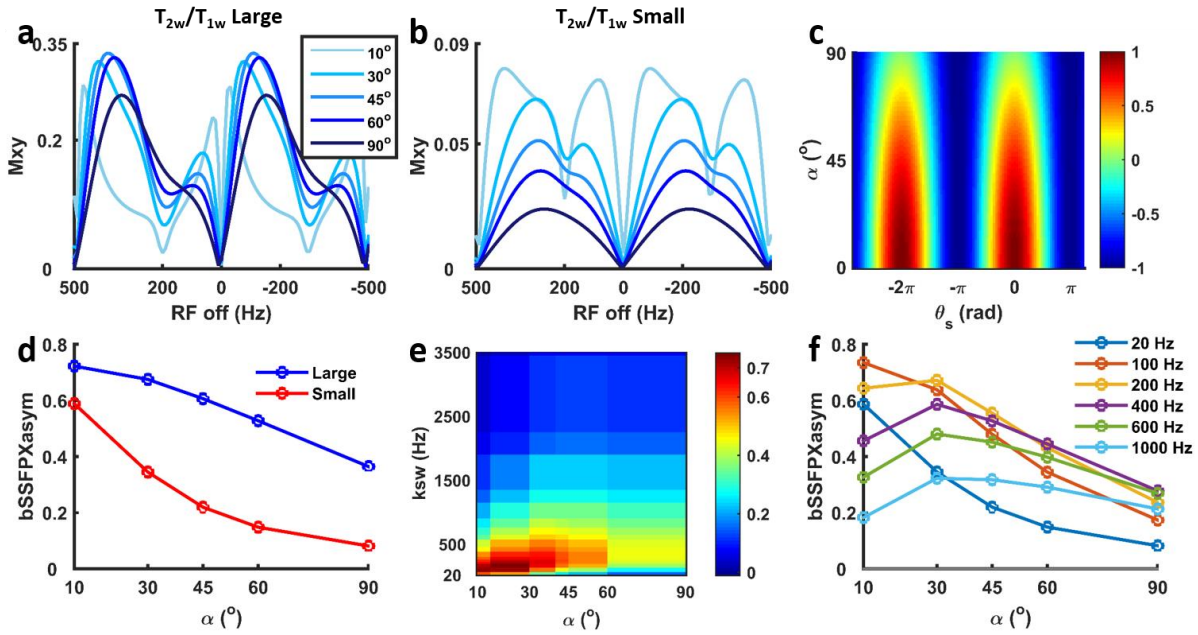

Figure 2-6 Two-pool simulation of the bSSFPX spectra dependence on the flip angle. Two-pool simulation of the bSSFPX spectra dependence on the flip angle α for (a) T_{2w}/T_{1w}~0.83 (T_{2w} = 2.4 s and T_{1w} = 2.9 s) and (b) T_{2w}/T_{1w}~0.025 (T_{2w} = 0.05 s and T_{1w} = 2 s), assuming Δ_{ws} of 200 Hz. Other simulation parameters are the same as Section 2.4.1. (c) The $bSSFPX_{asym}$ at 200 Hz versus flip angle for T_{2w}/T_{1w}~0.83 (blue) and T_{2w}/T_{1w}~0.025 (red). (d) The cosine of the effective field precession angle Φ_s as a function of the flip angle α and the precession angle $\theta_s=2\pi\Delta_s TR$. (e) The $bSSFPX_{asym}$ at 200 Hz as a function of k_{sw} and the flip angle α. (f) Different snapshot of (e), $bSSFPX_{asym}$ at 200 Hz vs. α for a number of exchange rates. For TR of 2.025 ms, α = 10°, 30°, 45°, 60°, 90° corresponds to $B_{1,CW}$ = 0.32, 0.97, 1.45, 1.93, and 2.90 μT, respectively.

The interplay between exchange rates and flip angle is further investigated for small chemical shift difference (Fig. 2-6e, f) and larger chemical shifts (results not shown here, can be found in the Supplement Figures in Ref. (97)). Here too, the analogous nature of the bSSFP and CEST is apparent, when converting flip angle and TR into the $B_{1,\,CW}$. In both methods, optimal B_1 exists for each k_{ex} (99), and the optimal B_1 is higher for faster exchange rates (for CEST the condition is $2\pi B_{1,opt} \sim k_{ex}$ (25)). Both methods are identical for small chemical shifts. Interestingly, for large chemical shift differences, the optimal B_1 for $bSSFPX_{asym}$ for intermediate to fast exchange does not increase much and the $bSSFPX_{asym}$ remains about the same when $B_{1,field}$ exceeds certain value (97). This possibly is due to the repetitiveness of the bSSFPX profile. For small chemical shifts the results of the Figure 2-6f reiterate previous paragraph conclusion: smaller flip angles α (weaker B_1) translate to the most efficient "saturation" and higher asymmetries. Thus, in the phantom experiments that have a large T_{2w}/T_{1w} ratio, $\alpha \approx 30° - 45°$ ($B_{1,CW}$ ≈ 0.97 - 1.45 μT) was chosen to maximize SNR and CNR.

2.5.1.2 Phantom validation

As was shown in the previous section, the bSSFPX and asymmetry analysis performs best when the chemical shift difference is less than 0.5/TR. The shortest TR attainable on our scanner is about 2 ms. Thus, to ease interpretation, the model systems with the chemical shift difference between the solute and the solvent less than 250 Hz were chosen: choline, glucose and glycogen solutions in water. Furthermore, in addition to the small chemical shift difference, which is beneficial for the bSSFPX, these molecules have other features making

them good models for CEST experiment. Choline is a small molecule with a single hydroxyl group whose exchanging proton resonates at ~1 ppm downfield from water (15,100). D-Glucose have several exchanging OH groups with the most prominent CEST effect around 1 ppm (4). Similarly, the glycogen molecule possesses several exchanging sites with the maximum CEST around 1 ppm (101). The solutions behavior can be approximated by a two-pool model with their Z-spectra displaying a single prominent dip at ~1 ppm in the saturation transfer spectrum. There are no MTC and NOE effects to confound data analysis in the first proof-of-principle step (minor NOE was observed in glycogen). Lastly, a number of recent studies has explored these molecules as interesting markers of cancer metabolism (choline) (100,102,103), physiology (glycogen) (13) and infusion agent in cancer (glucose) (14).

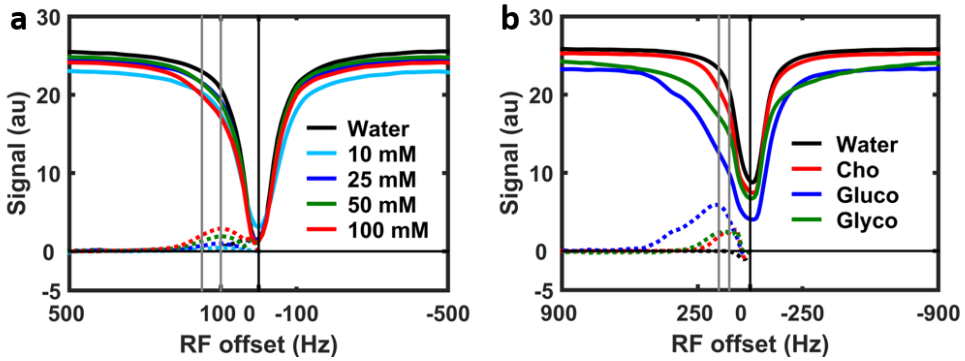

Figure 2-7 Non-normalized Z-spectra and MTR_{asym} for phantom I and II.
Non-normalized Z-spectra and MTR_{asym} for (a) different concentrations of choline solutions: 0 (black), 10 mM (light blue), 25 mM (indigo), 50 mM (green) and 100 mM (red) and (b) different molecules: water (black), choline (Cho, red), glucose (Gluco, blue) and glycogen (Glyco, green). The solid and dotted lines correspond to profiles and asymmetry, respectively. A set of two vertical lines on the downfield side indicates the frequency range 100 - 150 Hz in which the MTR_{asym} is averaged.

Figure 2-7 shows the Z-spectra of the phantoms I and II obtained using the standard pulsed CEST experiment. The maximum CEST effect of choline, glucose and glycogen

occurs at ~1 ppm downfield of water. Therefore, a frequency window from 0.8 to 1.2 ppm is chosen to calculate the MTR_{asym}.

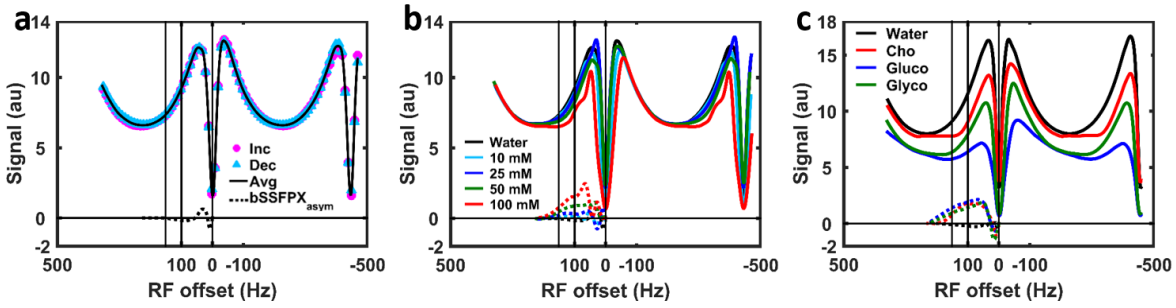

Figure 2-8 Experimental bSSFPX profiles for phantom I and II.
(a) Acquisition and processing steps demonstrated in water phantom: increasing sweep (purple dots), decreasing sweep (blue dots), their average (black line) and non-normalized bSSFPX profile asymmetry. (b) bSSFPX profiles (average of the increasing and decreasing sweeps) and non-normalized bSSFPX asymmetries for different concentrations of choline solutions in Phantom II: 0 (black), 10 mM (light blue), 25 mM (indigo), 50 mM (green) and 100 mM (red). (c) bSSFPX profiles and non-normalized bSSFPX asymmetries for phantom I: water (black), choline (red), glucose and glycogen (green), The solid and dotted lines correspond to profiles and asymmetry, respectively. A set of two vertical lines on the downfield side indicates the frequency range 100 - 150 Hz in which the $bSSFPX_{asym}$ is averaged.

Figure 2-8 displays the bSSFPX experimental results: the processing steps shown for the pure water phantom (Fig. 2-8a), the XY-spectra of the choline solutions of increasing concentrations (Phantom II, Fig. 2-8b) and the XY-spectra of choline, glucose and glycogen phantoms (Phantom I, Fig. 2-8c). Since the reference image "without RF" does not exist in bSSFPX, the profiles and $bSSFPX_{asym}$ shown in Figure 2-8 were not normalized. As shown in Figure 2-8a, asymmetries can be seen in both the increasing (Fig. 2-8a red dot) and decreasing (Fig. 2-8a blue dot) frequency sweep profiles. The averaged profile (Fig. 2-8a black solid line) largely corrects this unwanted asymmetries, however some residual

asymmetry still remains close to water. This could be because the 7.7 s saturation time is still not enough to get to a complete steady-state for water with T_1 of ~3.0 s. As shown in Figure 2-8b, the maximum $bSSFPX_{asym}$ effect in choline is observed about 0.8 ppm which is less than 1 ppm observed in the pulsed CEST experiment (Fig. 2-7). We continued to use the average frequency window determined from the CEST Z-spectra for consistent comparison. From Figure 2-8b it is evident that the $bSSFPX_{asym}$ increases with increased choline concentration. Additional asymmetries still observed close to on-resonance and, as in the water case, can be explained by very long T_1 in the phantom used.

The $bSSFPX_{asym}$ map for phantom II is shown in Figure 2-6a. The map confirms that the $bSSFPX_{asym}$ increases with the increased choline concentration. The $bSSFPX_{asym}$ averaged over the whole ROI and the frequency window is shown in Figure 2-9b. The $bSSFPX_{asym}$ increases almost linearly with the concentration, and is equal to -1.1±0.5, 1.2±0.6, 4.0±0.8, 8.7±0.6 and 15.2±0.8% for 0, 10, 25, 50 and 100 mM, respectively. Figure 2-9c demonstrates the observed MTR_{asym}. Figures 2-8b and c are very similar in overall behavior, except that the $bSSFPX_{asym}$ is about 5% higher than the corresponding MTR_{asym} at highest concentrations. Our simulated results using CW saturation indicated inverse trend (MTR_{asym} higher than $bSSFPX_{asym}$). However, the experimental pulsed CEST performance may depend on other factors, such as pulse shape and duty cycle, as well as acquisition parameters such as TE and TR, which does not take into account. Indeed, other metrics, such as average power might be more appropriate for the evaluation of pulsed CEST performance (104). Despite these quantitative differences, the overall qualitative similarity indicates that the bSSFPX provides CEST contrast comparable to the standard pulsed CEST method.

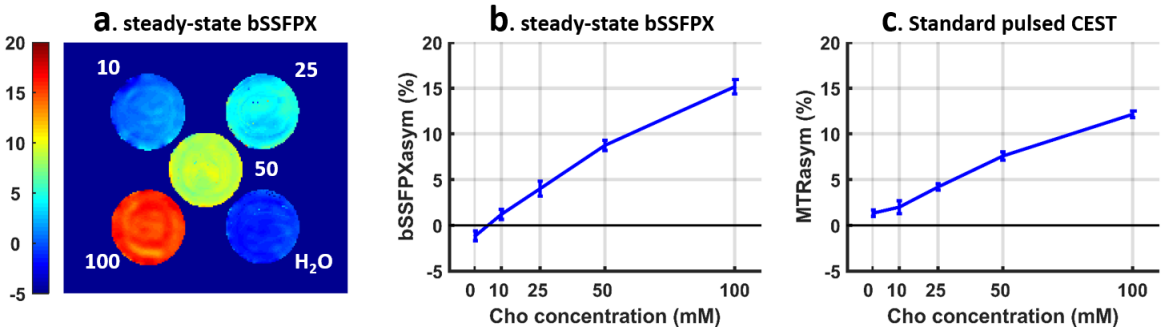

Figure 2-9 ss-bSSFPX results for phantom II.
(a) $bSSFPX_{asym}$ map, (b) ROI averaged $bSSFPX_{asym}$ for different choline concentrations and (c) ROI averaged MTR_{asym} for different choline concentrations.

Figure 2-10 compares $bSSFPX_{asym}$ and MTR_{asym} for a number of molecules with small chemical shift differences: choline, glucose and glycogen. All three show a very high bSSFPX effect: 14.7±0.3, 21.9±0.5, 14.4±0.6 for choline, glucose and glycogen, respectively (Fig. 2-10b). Similar to the results in choline, these values are very comparable to the MTR_{asym} observed using standard CEST methods in these molecules (Fig. 2-10c).

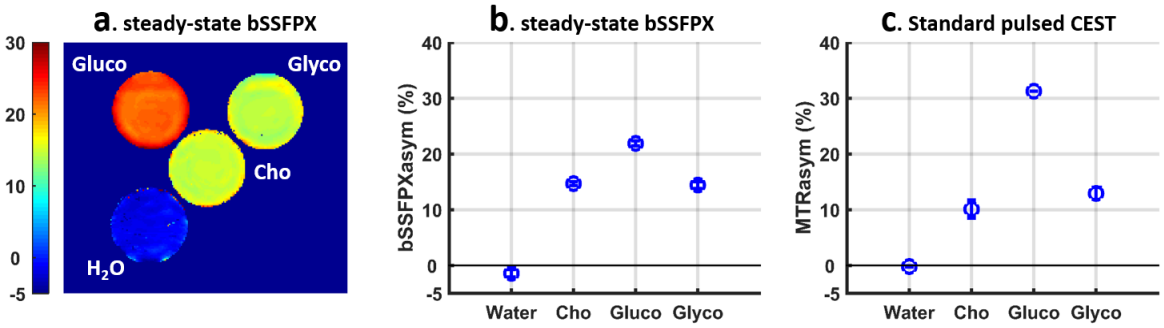

Figure 2-10 ss-bSSFPX results for phantom I.
(a) $bSSFPX_{asym}$ map, (b) ROI averaged $bSSFPX_{asym}$ and (c) ROI averaged MTR_{asym} for different molecules. Cho: choline, Gluco: glucose and Glyco: glycogen.

The bSSFPX profile repeats itself every 1/TR. Based on the simulation results, in this proof-of-principle study, only the molecules with one exchangeable group and small

chemical shift difference close to water have been investigated. As was already discussed in the simulations results, if the chemical shift difference of the solute pool is greater than the period 1/TR, the dip will fold over in the profile. Such folded profiles might still be analyzable if we know exactly the chemical shift of the solute pool beforehand, otherwise it is hard to tell where the solute pool lies in the spectrum. A solute molecule possessing several exchanging sites, within and outside the 1/TR range will make the analysis more difficult and complicated. The simplest work around is to decrease TR, which is hardware limited and may not be feasible.

At the same time, simulation and experimental results indicate excellent performance of bSSFPX at the small chemical shifts, for a large range of exchange rates (Figs. 2-4, 2-6, 2-9 and 2-10). Thus, we anticipate that bSSFPX would be most useful for the detection of solutes with a small chemical shift difference from water, such as choline, glycine, and glucose shown here, or glycosaminoglycan and myo-inositole.

The average $B_{1,CW}$ attainable with bSSFPX, is generally lower than in standard CEST and is limited by the nature of the experiment. The highest α useful for imaging is 90^{o}. The $B_{1,CW}$ may be further increased by shortening TR. In our machine the hardware parameters translated to the highest $B_{1,CW}$ of 2.9 μT. However, this is not the limiting factor on the bSSFPX performance, since the simulation and experimental results indicate optimal performance is achieved using smaller flip angles and correspondingly lower average B_1. This is perhaps the biggest difference from the standard CEST.

It should be noted that the sequence is very straightforward to implement. The only optimization that might be required is in terms of the flip angle, and adjusting TR to the

minimum value. Moreover, since duty cycle is so low, very long saturation times can be achieved effortlessly. The processing is relatively straightforward too, combining elements from bSSFP processing and CEST. Additional advantage of the sequence is that it does not require acquisition of a separate B_0 map. In contrast, obtaining reliable CEST and B_0 correction data for chemical shifts close to water can be very challenging in standard implementation. This could potentially serve as an advantage of bSSFPX in imaging of agents with chemical shift difference close to water.

One more distinctive feature of bSSFPX sequence is the application of the gradients during excitation/saturation pulse. For standard CEST, usually no gradients are used during saturation pulses; hence, the whole volume is saturated. For the single slice bSSFPX, only the spins in the imaging plane are saturated. The standard excitation pulses with standard gradients were used without any additional refinements. It is anticipated that as long as the slice selective excitation pulses perform adequately, the bSSFPX sequence will work and it is not sensitive to the gradients during the excitation pulses.

2.5.2 Phantom results of ts-bSSFPX

The evolution of the transient signal is governed by the relaxation times $T_{1\rho}$ and $T_{2\rho}$, parallel and perpendicular to the effective field, respectively (105) and by the precession frequency around the effective field. Similar to the CW case, both relaxation times depend on the off-resonance value as well as on the flip angle and contain exchange contributions.

Figure 2-11a shows the evolution of agar (phantom III) XY-spectra from the transient state (lighter blue lines) into the steady-state (darker blue lines) as the effective saturation time increases. In the Figure 2-11b, the signals at ±1.2 ppm are plotted against t_{sat}. Since the intrinsic T_2 in agar is short, the signals are largely governed by the $T_{1\rho}$ decay as they approach the steady-state and no transient oscillations were observed. As a result, the signals can be fitted to the equation $S(t) = S_{ss}(1-e^{-t/T_{1\rho}}) + S_0 e^{-t/T_{1\rho}}$ for $T_{1\rho}$. Agar has no exchanging moieties, hence its steady-state bSSFP profile is symmetric about water and the steady-state signals are similar for both frequencies. As expected, the fitted $T_{1\rho}$ at ±1.2 ppm are similar: 360±30 and 420±20 ms, respectively.

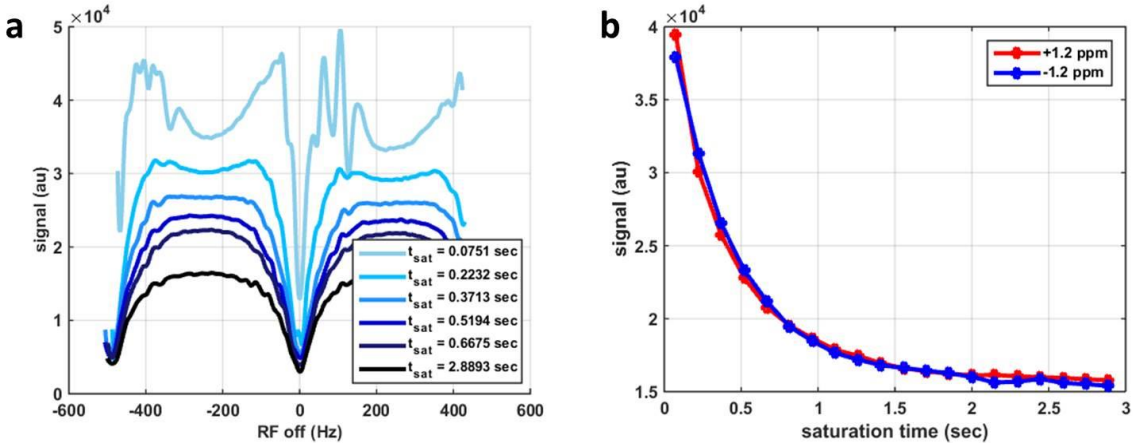

Figure 2-11 ts-bSSFPX profiles and signals for the agar phantom.
(a) Agar XY-spectra acquired using the transient-state bSSFPX. (b) Signals at ±1.2 ppm of a representative agar pixel against effective saturation time.

Figure 2-12 shows the 10 and 100 mM choline water solution XY-spectra against the effective saturation time. The T_1 and T_2 of the aqueous solutions are very long thus prominent transient oscillations and spurious effects were observed, especially at the earlier

time points. However, the profiles approach steady-state values as the saturation time increases. The steady-state profiles are asymmetric about water due to chemical exchange at ~1 ppm downfield (Fig. 2-12b, arrow). The MTR_{asym} (1 ppm) also approaches its steady-state values of ~2%, 10% and 16% for 10, 50 and 100 mM respectively (Fig. 2-13). After the initial transient oscillations (asterisks in Fig. 2-13), the MTR_{asym} demonstrates exponential growth similar to the QUEST curves (61). Some residual oscillations due to transient effects or experimental imperfections are still observed. As shown in Figure 2-2b, the acquisition is effectively performed during the saturation; hence one "shot" of the ts-bSSFPX sequence acquires sufficient data for $T_{1\rho}$ and/or exchange rate quantification, which may largely speed up the quantification process. The $T_{1\rho}$ and, potentially, the exchange rate could be then obtained by fitting the curves (Fig. 2-11b or Fig. 2-13).

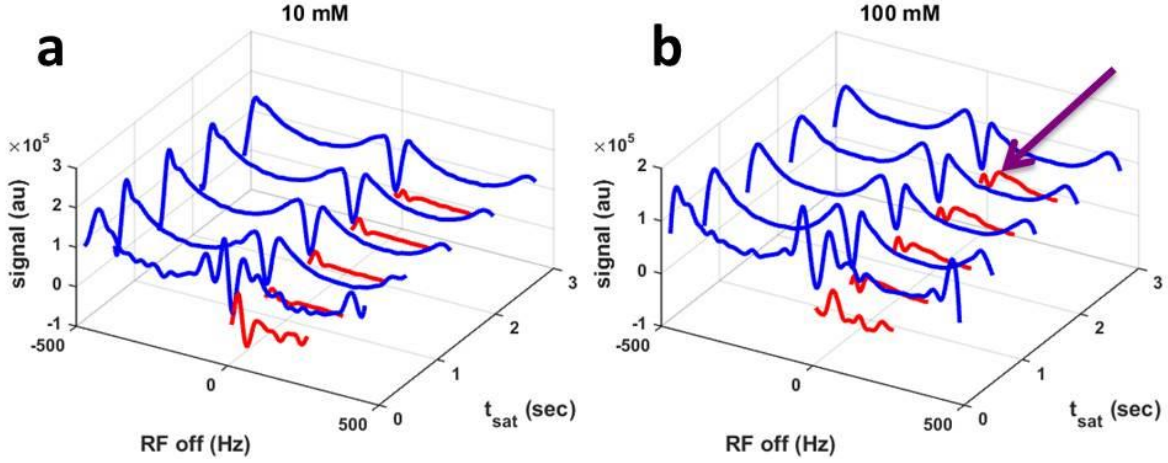

Figure 2-12 ts-bSSFPX results for choline water solution phantoms.
XY-spectra (blue) and MTR_{asym} (red) of 10 mM (a) and 100mM (b) choline solutions acquired using transient bSSFPX as a function of the effective saturation time, t_{sat}. All 20 t_{sat} points are acquired at a single shot with only 5 profiles shown.

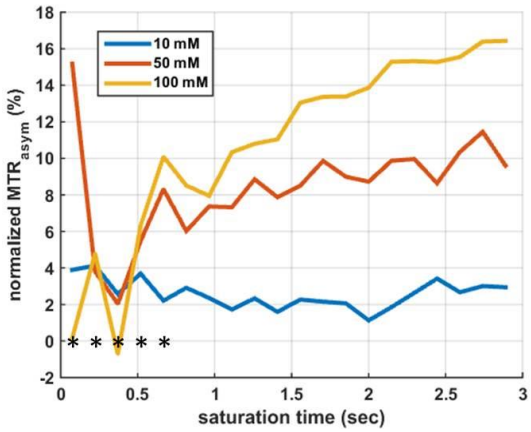

Figure 2-13 QUEST-like curve for choline water solutions.
Single-shot MTR_{asym} (1 ppm) versus saturation time (QUEST) curves for 10 mM (blue), 50mM (red) and 100mM (yellow) concentrations of choline solution. *: transient oscillations.

2.5.3 Analytical model compared with Bloch-McConnell simulations

Figure 2-14 compares the steady-state water only spectra obtained using the analytical model (Eq. 2.12). with the Bloch-McConnell Equations (BME) simulations. The analytical model is in excellent agreement with the BME for both Z- and XY-spectrum for the one-pool system. For the exchanging two-pools, the model is in good qualitative agreement with BME. At the steady-state, the solution follows BME for the most part but deviates slightly downward at the star labeled frequencies close to water (Fig. 2-14b, d).

Figure 2-15 compares the time evolution of the water only Z- and XY-spectra obtained using the analytical model (Eq. 2.19) with the BME simulations. The overall behavior and the agreement at both short and long t_{sat} is excellent, indicating that the model correctly depicts transient oscillations with $T_{1\rho}$ and $T_{2\rho}$ relaxations. However, large deviations were observed close to the saturation bands for short t_{sat} ($t_{sat} < 3T_{1w}$). These results indicate that the exchange contribution (Eq. 2.21) needs to be further improved.

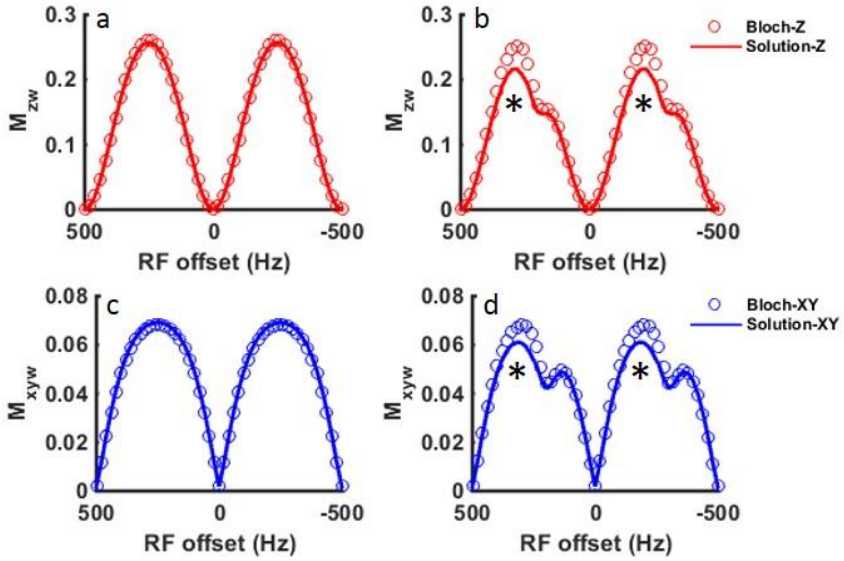

Figure 2-14 Comparison between the analytical model and Bloch-McConnell Equations simulations in the steady-state.

The simulated steady-state Z- (a, b) and XY-spectra (c, d) for 1-pool model (a, d) and 2-pool model (b, d). Circle: Bloch-McConnell Equations. Solid line: the derived analytical solution. *: solution deviates slightly downward from the Bloch-McConnell Equations.

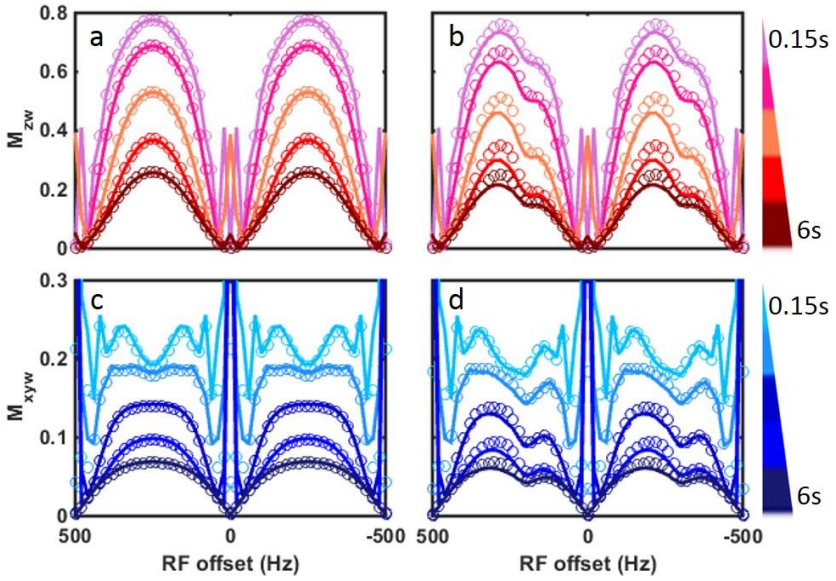

Figure 2-15 Comparison between the analytical model and Bloch-McConnell Equations simulations in the transient state.

The simulated time-dependent water only Z- (a, b) and XY-spectra (c, d) for 1-pool model (a, d) and 2-pool model (b, d). Circle: Bloch-McConnell Equations. Solid line: the derived mathematical model. Different colors from light to dark correspond to different saturation times: 0.15, 0.25, 0.5, 1, and 6 s.

2.5.4 In vivo study

The bSSFPX sequence was first tested in human brain, because brain is relatively free of motion and fat. Figure 2-16 shows the bSSFPX results of the three volutneers: the bSSFP images of the longest effective t_{sat} at 125 Hz or ~1 ppm (Fig. 2-16a, d, g), the $bSSFPX_{asym}$ maps averaged between 100 - 150 Hz (Fig. 2-16b, e, h) and the overlays of the bSSFP images and the $bSSFPX_{asym}$ maps to better locate the hyperintensity signals in the $bSSFPX_{asym}$ maps (Fig. 2-16c, f, i). The overlay images showed that the highest $bSSFPX_{asym}$ are mainly in the white matter (WM), especially in the corpus callosum regions.

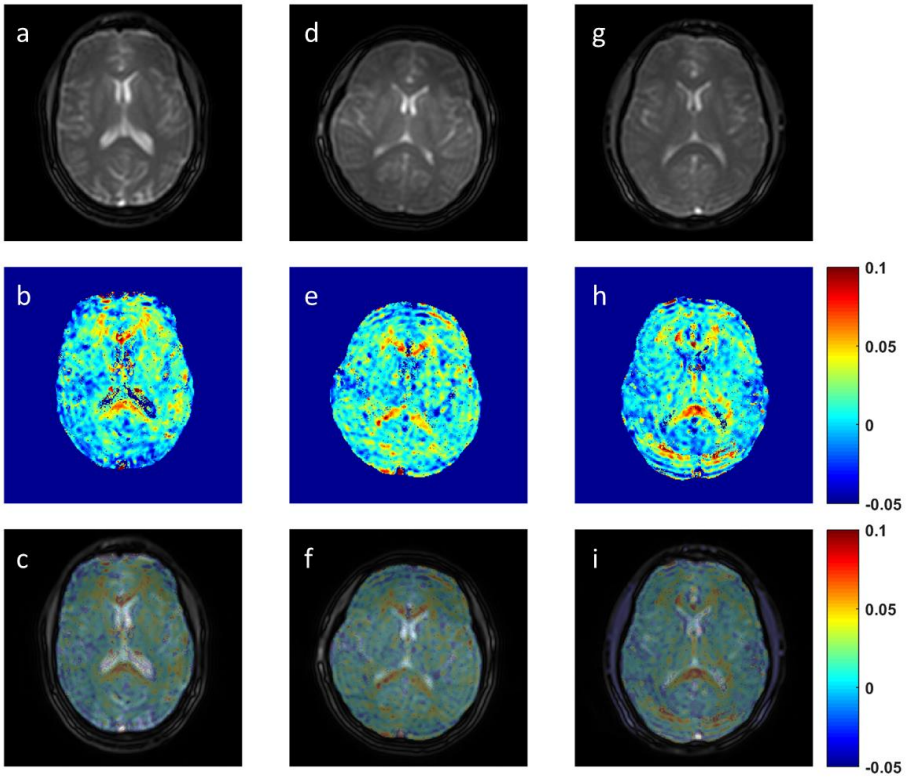

Figure 2-16 bSSFPX results for human brain.
bSSFPX results for subject 1 (a-c), subject 2 (d-f) and subject 3 (g-i). (a, d, g) The bSSFP images with the longest effective saturation time (2.4 s for subject 1 or 2.3 for subject 2, 3) at

125 Hz. (b, e, f) The $bSSFPX_{asym}$ maps averaged between 100 - 150 Hz. (c, f, i) The overlays of the bSSFP images and the $bSSFPX_{asym}$ maps.

Figure 2-17 shows the representative ROI-averaged bSSFPX profiles and $bSSFPX_{asym}$ of subject 3. Evident bSSFPX asymmetry was observed in the WM profile while the gray matter (GM) profile was almost symmetric about the water frequency. The largest asymmetry of the WM profile is located close to the water frequency. The asymmetry decreases as the off-resonance frequency is increased away from water. However, the asymmetry can still be observed in the 100 - 150 Hz frequency range.

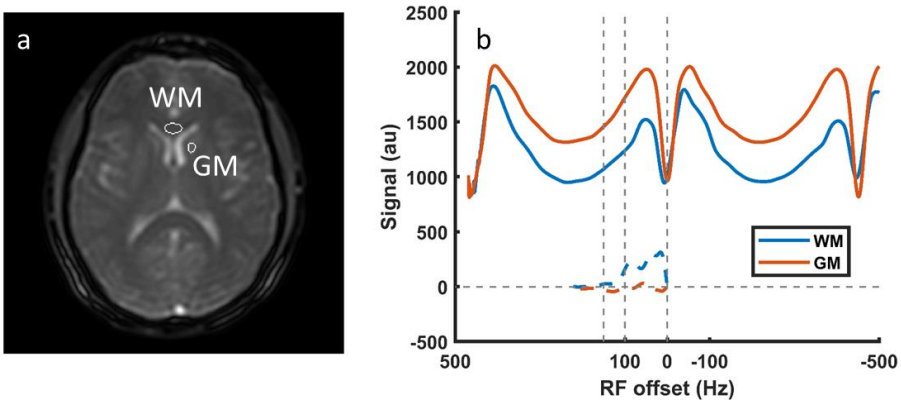

Figure 2-17 ROI averaged bSSFPX profiles and $bSSFPX_{asym}$.
(a) The white matter (WM) and gray matter (GM) ROIs and (b) the ROI-averaged bSSFPX profiles and $bSSFPX_{asym}$ of subject 3.

As discussed in the Ref. (82), the presence of intravoxel frequency distribution can cause the bSSFP profile asymmetry. However, the origin of the frequency distribution in the WM is still under investigations and discussions. Miller *et. al.* proposed that the susceptibility-induced field shifts dictated by the microstructure of the fiber tracts would be a possible origin and the resulting asymmetry is orientation-dependent (82,106). However, the

asymmetries of investigated in those studies were located very close to water, and were not assigned to a specific frequency range.

In our study, we show that the asymmetry may originate from chemical exchange effect of certain metabolites in the brain, such as myo-inositol (58). The asymmetry is assigned to a specific frequency range and is supposed not orientation-dependent. Further elaborate experiments are needed to validate the assumptions.

2.6 BSSFPX VS. CEST AND SL

The bSSFPX method provides an alternative way to acquire CEST and off-resonance SL ($T_{1\rho}$) data. Compared with the CEST and SL experiments, bSSFPX has several advantages. First, bSSFPX has the potential to speed up the quantitative CEST and SL. Either requires several repetitions of the experiment with different saturation time or spin-locking time. However, bSSFPX can acquire the data in a single experiment, because the acquisition is performed during the saturation. Second, long saturation time becomes achievable in clinical scanners due to the low duty cycle of the bSSFPX imaging sequence. Third, bSSFPX provides a conceptually different way to acquire exchange-sensitive information. Forth, compared with CEST, it is more robust for the acquisition of exchange information from groups resonating close to water (such as -OH).

The bSSFPX method has several disadvantages compared with CEST and SL. The most pronounced disadvantage is that the bSSFPX profile is repetitive, and the repetition period is TR dependent. As a result, the dips from the pools with chemical shifts exceeding

1/TR fold back into each cycle. Therefore, the bSSFPX profile is not as straightforward as CEST or CESL Z-spectrum and should be interpreted with care. Moreover, to cover more frequencies in a cycle, the TR needs to be as short as possible. The shortest TR is limited by the scanner hardware. The shortest TR in our 3 T scanner is about 2 ms. Assuming similar shortest TR, bSSFPX would have limited application at high fields (e.g. 7T) because less frequencies could be covered in a 1/TR cycle at high fields than at the low fields.

2.7 FUTURE DIRECTIONS

In the future, the analytical model will be further improved. The R_{ex} term used in the model is derived from the CW saturation, which may not suitable for pulsed saturation as is the case in the bSSFPX sequences. In addition, the analytical model for quantitative exchange rate measurement needs to be validated in the phantom studies. This is the ongoing work in the lab.

As discussed in the Section 2.5.4, the human brain study needs further investigation. To validate the assumptions, the brain is to be scanned in different orientations using bSSFPX and the subsequent $bSSFPX_{asym}$ in different brain regions are to be compared. Moreover, the bSSFPX images are to be compared with that of standard CEST images. To find the major contributors to the CEST effects around 1 ppm in the human brain, phantoms studies of possible metabolites are to be performed.

2.8 CONCLUSION

In this project, the analogous nature of bSSFP and CEST/$T_{1\rho}$ experiments is realized and explored. The ss-bSSFPX method was implemented and its feasibility for CEST experiments was proved through simulations and phantom studies. The comparison between the bSSFPX and the standard pulsed CEST experiments confirmed that the bSSFPX method could provide comparable CEST contrast to the standard experiment. The ts-bSSFPX method, aimed at the single-shot quantitative CEST/$T_{1\rho}$ experiments, was implemented and tested in phantoms. The analytical model is derived for bSSFPX based on the effective filed. Overall, this model is in good agreement with BME and follows the transient signal oscillations well. Work is in progress to use this model to quantify the exchange rate experimentally.

In a first in vivo experiment, the bSSFPX was tested in human brain. The results show that the WM has higher signals than the GM. We hypothesize that the asymmetry may originate from chemical exchange effect of certain metabolites in the brain. Further elaborate experiments are needed to validate this hypothesis and identify the major contributors to the $bSSFPX_{asym}$. Based on the results, we anticipate that the sequence could be a useful addition or alternative to CEST/$T_{1\rho}$ studies using molecules with small chemical shift difference from water like glucose, glycogen, choline, glycosaminoglycan or myo-inositol. Although it might be too early to speculate, we anticipate that the sequence will perform well in the studies of glucose infusion into brain tumors. As a new CEST data acquisition method, the bSSFPX experiment holds high promise for fast, quantitative and 3D CEST imaging.

CHAPTER THREE
Lipid influence on CEST

3.1 OVERVIEW

This work was accepted for publication in the Magnetic Resonance in Medicine 2018; 79(5):2731-2737. Portions of this work were presented at the 25th ISMRM in Honolulu, HI, United States (April 2017) and the Music City CEST in Nashville, TN, United States (August 2017).

CEST MRI is increasingly evolving from brain to body applications. One of the known problems in the body imaging is the presence of strong lipid signals. Although their influence on the CEST effect is acknowledged, there was no study that focuses on the interplay among echo time, fat fraction, and Z-spectrum. In this chapter, we addressed these points with the emphasis on the application in the breast. The influence of non-exchanging fat on Z-spectrum and MTR_{asym} was first studied by simulation at varying fat fractions and two echo times, in phase and out of phase. The results were then verified in phantoms and in vivo.

3.2 INTRODUCTION

Most human applications of CEST focus on the brain, utilizing solute amides resonating at 3.5 ppm, the so-called APT (8,47,49,107). Recently, there is an increasing trend

for CEST applications outside the brain. Promising applications were reported in prostate cancer (51), breast cancer (50,108-110) and renal ailments (111). One of the problems in body imaging is the presence of a large fat signal. Fat has a short T_1 and a long T_2 hence always appears bright on both T_1- and T_2-weighted images, confounding image interpretation. The problem is very acute in breast, where fibroglandular tissue and fat are interleaved. The influence of fat on image quality as well as suppression methods have been investigated long before CEST. However, the influence of fat in CEST imaging is relatively new and underexplored, although its confounding influence is acknowledged (10). Fat has multiple peaks in its ^{1}H-NMR spectrum ranging from 0.8 ppm to -4 ppm with respect to water and its main peak resonates at about -3.4 ppm (112). Hence, in the CEST Z-spectrum, it is on the opposite side of many diamagnetic or endogenous CEST agents. As a result, the CEST effect measured using MTR_{asym} analysis becomes inaccurate in the presence of fat, affecting APT the most. Moreover, fat overlaps with the nuclear Overhauser enhancement (NOE) (22-24,113). Separating NOE from fat is desired, not only for accurate quantitative CEST contrast analysis but also for using NOE as a source of contrast.

Although methods to remove lipid artifacts in CEST imaging were reported (113-115), there was no study focusing on the interplay between image acquisition parameters, fat fraction (FF) and the Z-spectrum.

The goal of the study is to discuss how the fat influences the Z-spectrum taking echo time (TE) into account in the gradient echo based sequences. The interplay is studied in simulations and verified in phantom and in vivo experiments. The study predominantly focuses on the CEST at 1 ppm, since previous studies indicated that it might be the most

sensitive to the malignant alternations in breast (100,108,110,116,117). However, other offsets, exchange regimes and experimental parameters are briefly addressed. This study demonstrates and explains the abnormal appearance of Z-spectra when fat is present and emphasizes the importance of a correct choice of the imaging parameters. The goals are to help in recognizing lipid artifacts in CEST images, to provide suggestions on the selection of imaging parameters and to build a foundation for the most efficient removal of these artifacts in the future studies.

3.3 METHODS

3.3.1 Simulation

Simulations (Matlab, The Mathworks, Natick, MA) used a three-pool Bloch-McConnell model including a bulk water pool (subscript w), a solute pool (s) and a fat pool (f). The water and solute pools are in chemical exchange and the solute/water ratio was kept constant. There is no exchange between fat and the other pools. To simulate different intravoxel FF, the pool sizes for water (M_{0w}) and fat (M_{0f}) varied between 0 and 1, with $FF = M_{0w} / \left(M_{0w} + M_{0f} \right)$ increasing from 0 to 100% while satisfying $M_{0w} + M_{0f} = 1$. Other parameters included T_{1w} = 1.5 s, T_{2w} = 0.8 s, M_{0s}/M_{0w} = 0.005, T_{1s} = 1 s, T_{2s} = 1 s, Δ_{ws} = 1 ppm, k_{sw} = 100 Hz, T_{1f} = 0.8 s, T_{2f} = 0.5 s, Δ_{wf} = -3.4 ppm, where $\Delta_{ws/f}$ is the chemical shift between water and the solute/fat pool, and k_{sw} is the exchange rate from solute to the water pool. A CW pulse with length t_{sat} = 5 s and B_1 ~0.97 μT was used for all simulations. To

study the influence of TE while avoiding the influence of other imaging parameters, the water and fat Z-magnetizations after the saturation pulse were tipped to the XY-plane assuming a perfect 90° pulse. Then, the signal was simulated assuming two conditions: in-phase (IP, 360° phase difference between water and fat) and out-of-phase (OP, 180° phase difference). The simulated MTR_{asym} was averaged in two ranges: 0.8-1.2 ppm centering at the solute pool (hydroxyl-MTR_{asym}) and 3.3-3.7 ppm centering at 3.5 ppm (amide-MTR_{asym}, opposite to fat resonance, to monitor fat influence on the Z-spectra in the absence of an exchanging moiety). Additional simulations were performed to gauge the influence of different solute properties (Δ_{ws} = 1, 2, 3.5 and 5.1 ppm in slow, intermediate and fast regime) as well as under different experimental conditions (B_1 = 0.5-5 μT and t_{sat} = 0.5-7.5 s).

3.3.2 Phantom

Three phantoms containing water solutions of exchanging molecules and oil (Crisco vegetable oil, the J.M. Smucker Co, Orrville, OH) were prepared. Phantom I contained 100 mM choline at pH = 5.9 (24°C, no additional buffers). Phantoms II and III contained 194 mM iopamidol (Isovue-370, Bracco Diagnostics, Milan, Italy) with the pH adjusted by titration to 7.5 and 6.0 respectively. Since the water solutions and oil are immiscible, an interface between them builds up automatically (Fig. 3-1).

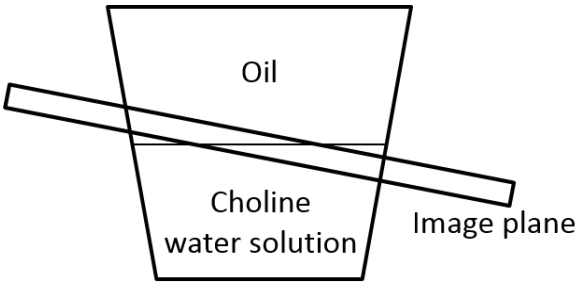

Figure 3-1 Schematic of the phantom and the image plane.

3.3.3 In vivo study

Three female volunteers without known breast ailments were recruited. The human study was approved by the local institutional review board and performed in accordance with the guidelines. Written informed consent was obtained from each subject.

3.3.4 MRI

All MRI scans were performed on a 3 T whole-body scanner (Ingenia, Philips Healthcare, Amsterdam, the Netherlands). The phantom studies employed a 15-channel head-spine coil at room temperature (~22°C). CEST images were acquired using a 2D single-shot T_1-weighted turbo field echo (TFE) sequence. Two scans were used to acquire CEST images with different TEs: i) IP at 2.30 ms and ii) OP at 3.45 ms, with the same TFE acquisition interpulse delay TR of 5 ms. The saturation pulse train was 4900 ms in length and consisted of 98 HS pulses, each 50 ms long, flip angle (FA) = 900° and no inter-pulse delay, equivalent to $B_{1,CW}$ = 1.17 μT (118). The total saturation and acquisition length was 5.1 s. Alternated parallel transmission is used to achieve an RF duty cycle of 100% (91). 41 points

in the Z-spectrum in the range ±6 ppm for phantom I or ±10 ppm for phantoms II and III were acquired. Other imaging parameters were: centric k-space ordering, voxel size 2×2 mm^2, slice thickness 8 mm and excitation FA = 45°. To obtain an image with varying FF, the image plane was placed oblique at the interface of oil and choline/iopamidol water solution (Fig. 3-1). Thus, the resulting image had a FF decreasing from 100% down to 0% from left to right (119).

The in vivo study employed a 16-channel bilateral breast coil. CEST images were acquired using the same TFE sequence with the same TEs (IP/OP) and interpulse TR as in the phantom study. The saturation pulse train (2 s) consisted of 40 HS pulses. Different saturation length was used in vivo to adhere to the stricter SAR limitations (< 90% body) and to utilize shorter T_1 in tissue (less time needed to reach the saturation steady-state). Total saturation and acquisition length was 2.6 s. 33 points in the Z-spectrum in the range ±6 ppm were acquired. Other imaging parameters were: centric k-space ordering, voxel size 2 × 2 mm^2, slice thickness 5 mm and excitation FA = 10°.

In all the studies, a separate B_0 mapping sequence (dual echo field echo with $TE_1/\Delta TE$ = 2.3/2.3 ms for two IP images) immediately followed the CEST imaging, without B_0 re-adjustment between the scans.

3.3.5 Data processing

The data were processed using custom MATLAB codes on a pixel-by-pixel basis. The field inhomogeneity was corrected using the separate B_0 map. The ROIs were placed

manually on regions with different FFs to generate ROI-averaged Z-spectra and MTR_{asym}. The exact FF in the experiments was not determined. The ROIs were selected qualitatively based on the position in the image. The IP and OP MTR_{asym} were averaged in different ranges to generate CEST maps: i) 3.3-3.7 ppm for the influence of fat (no exchanging pool present) in all the phantoms; ii) 0.8-1.2 ppm or 4.0-4.4 ppm and 5.3-5.7 ppm for choline or iopamidol, respectively. For the image plane position (Fig. 3-1) used in the phantom study, increasing row number corresponds to the increasing FF. The MTR_{asym} for each frequency range was averaged row-by-row and plotted against the row number (Figs. 3-6a, 3-8a and 3-10a).

3.4 RESULTS

3.4.1 Simulation

Figure 3-2 shows the representative simulated IP and OP Z-spectra and MTR_{asym} with different intravoxel FFs. Here both the Z-spectra and MTR_{asym} are normalized to the sum of the water and fat pool sizes for display purpose. Importantly, in the experiment, the results are normalized by the reference signal, which is also affected by the presence of fat and choice of TE. The influence of fat is further studied in two particular ranges, hydroxyl and amide, using continuously increasing FF (Figs. 3-3 and 3-4). In Figure 3-3, the MTR_{asym} was normalized to the reference signal. For comparison, normalization by the sum of the pool sizes is shown in Figure 3-4.

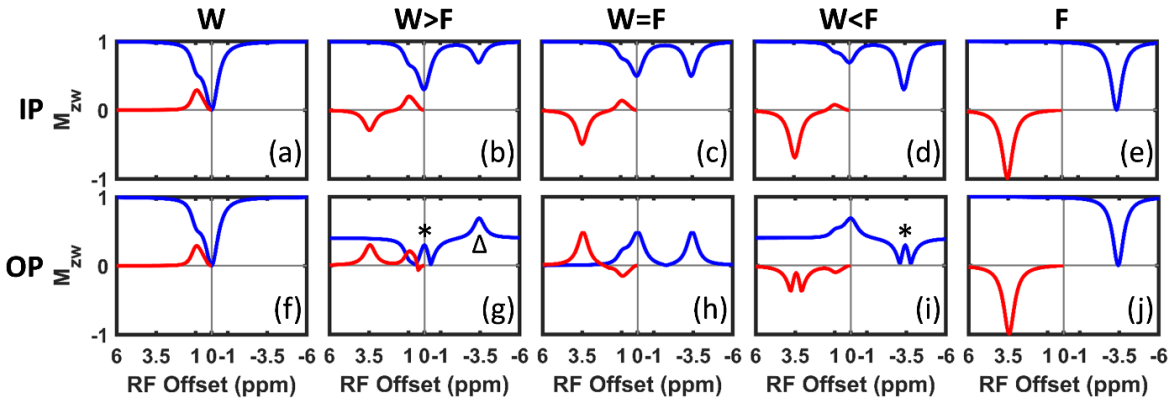

Figure 3-2 Simulated IP and OP Z-spectra and MTR_{asym} with varying FF.
Simulated (a - e) IP and (f - j) OP Z-spectra (blue line) and MTR_{asym} (red line) with FF of 0% (W), 30% (W > F), 50% (W = F), 70% (W < F) and 100% (F). The Z-spectra were normalized to the sum of the water and fat pool size for display convenience. (* in g and i) mark the "fold-back" of the negative values in the Z-spectra when magnitude is taken. (Δ in g) labels a fat related peak (see text for further discussion).

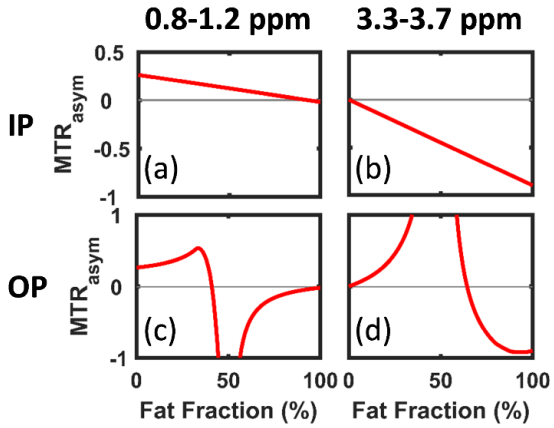

Figure 3-3 Simulated MTR_{asym} normalized to the reference signal against FF.
The simulated MTR_{asym} averaged in two ranges: 0.8-1.2 ppm (a,c) and 3.3-3.7 ppm (b,d) for IP (a,b) and OP (c,d) respectively. The MTR_{asym} were normalized to the reference signal, which is the sum of the water and fat signals with their relative phase taken into account. Part of the MTR_{asym} (very large negative and positive values due to normalized to a reference signal close to 0) are not shown in (c) and (d) for display convenience.

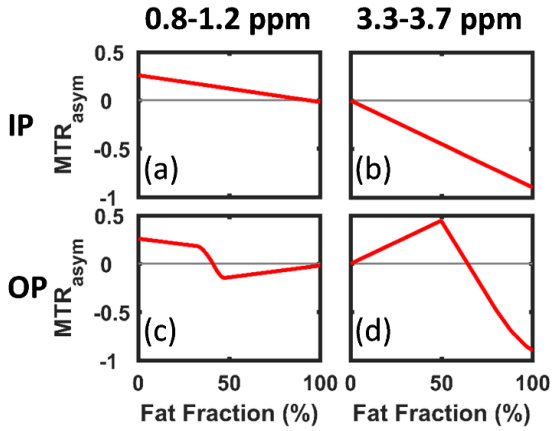

Figure 3-4 Simulated MTR_{asym} normalized to the sum of the pool sizes against FF.
The simulated MTR_{asym} averaged in two ranges: 0.8-1.2 ppm (a,c) and 3.3-3.7 ppm (b,d) for IP (a,b) and OP (c,d) respectively. The MTR_{asym} is normalized to the sum of the water and fat pool size.

As expected, if only water or fat is present, the IP and OP Z-spectra are identical (Fig. 3-2a vs. f and e vs. j). In IP, the water and fat signals overlap and the IP Z-spectra (Fig. 3-3a-e, blue line) are straightforward to understand: the water dip shrinks while the fat dip increases as the FF increases. Linear monotonic decrease of both hydroxyl- and amide-MTR_{asym} are observed in Figure 3-2a-e (red line), Figure 3-3a,b and Figure 3-4a,b.

The OP Z-spectra and MTR_{asym} are more complicated than the IP, since water and fat have a phase difference of $(2n+1)\pi$ ($n \in \mathbb{Z}$). As shown in Figure 3-2f-j, both water and fat could form 'dips' and 'ascends' in the Z-spectra depending on the FF. The reference signal approaches zero as FF approaching 50% (Fig. 3-2g-i). As a result, close to W =~ F, the MTR_{asym} normalized to the reference signal may become a very large positive or negative number, depending on the sign of the MTR_{asym} before normalization. As shown in Figure 3-3c, the hydroxyl-MTR_{asym} as a function of FF increases at first, indicating that the decrease of the reference signal is faster than the decrease of the hydroxyl-MTR_{asym} before

normalization. As FF approaches 50%, the hydroxyl-MTR_{asym} rapidly drops to a large negative value and gradually increases back to approximately zero for FF>50%. Conversely, the amide-MTR_{asym} increases from 0 to a very large value as FF increases from 0 to 50% and then decreases as FF further increases to 100% (Fig. 3-3d). The MTR_{asym} normalized to the sum of the water and fat pool sizes (Fig. 3-2, red line) shows similar trend to the MTR_{asym} normalized to the reference (Fig. 3-3) except for the decreasing OP hydroxyl-MTR_{asym} at low to mid FF (Fig. 3-4).

Additional simulations demonstrate that while the details change, the overall behavior remains consistent with the Figure 3-3 for a variety of experimental and solute parameters, including B_1, saturation time, exchange pool location and exchange rate (see Section 3.3.1). The results can be found in the Appendix A.

3.4.2 Phantom validation

Figures 3-5 and 3-6 show the results of the phantom I. The normalized IP and OP Z-spectra and MTR_{asym} were averaged in four ROIs: W only, W > F, W < F and F only. The choline peak is relatively far from the direct fat influence, especially at the low power levels used here (Fig. 3-5). Comparing Figure 3-2 and Figure 3-5, the experimental Z-spectra and MTR_{asym} maps display the same trends as the simulation. For the IP case, both the hydroxyl- (Fig. 3-6b) and amide- (Fig. 3-6d) MTR_{asym} decrease as FF increases, similar to the simulation (Fig. 3-3a,b). The hydroxyl-MTR_{asym} decreases from ~15% to ~0% (Fig. 3-6b) while the amide-MTR_{asym} decreases approximately linearly from 0% to about -45% (Fig. 3-

6d). As shown in Figure 3-6e-h, the OP MTR_{asym} maps display very large negative or positive values in the middle where W ~ F due to normalization by the reference values close to zero. In the regions W > F and W < F, the behavior of both the hydroxyl- and amide-MTR_{asym} (Fig. 3-6f,h) are also in exact agreement with the trend observed in the simulation (Fig. 3-3c,d).

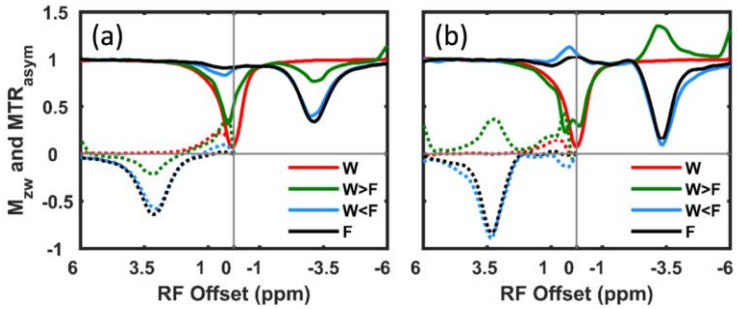

Figure 3-5 ROI averaged IP and OP Z-spectra and MTR_{asym} of choline-oil phantom. ROI averaged IP (a) and OP (b) Z-spectra and MTR_{asym} of the choline-oil phantom (Phantom I).

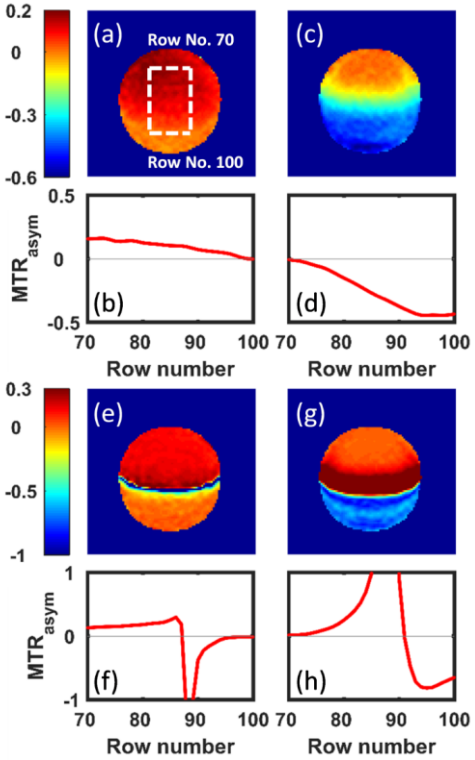

Figure 3-6 IP and OP CEST map and MTR_{asym} against FF of choline-oil phantom. The MTR_{asym} maps of choline-oil phantom (Phantom I) were generated by averaging the MTR_{asym} in two frequency ranges: 0.8-1.2 ppm (a, e) and 3.3-3.7 ppm (c, g) for both IP (a, c) and OP (e, g). The MTR_{asym} in each case are then averaged in the middle part of the CEST maps (vertical dashed line in (a), omitted in other images) row-by-row (horizontal dashed line in (a), omitted in other images) and plotted against the image row number (b, d, f, h). Part of the MTR_{asym} (very large negative and positive values due to normalization to a reference signal close to 0) are not shown in (f) and (h) for display convenience.

Figures 3-7, 3-8, 3-9 and 3-10 show the results of the phantoms II and III. The 4.2 ppm peak of iopamidol is close to direct influence of fat, while the 5.5 ppm peak is further away and thus is less influenced by fat. Moreover, there are two exchanging pools and exchange-mediated T_2 shortening (120). Despite these differences from the simple model systems above, the IP and OP CEST maps and MTR_{asym} (Figs. 3-7 to 3-10) show similar behavior as phantom I and simulations (Figs. 3-3, 3-5 and 3-6).

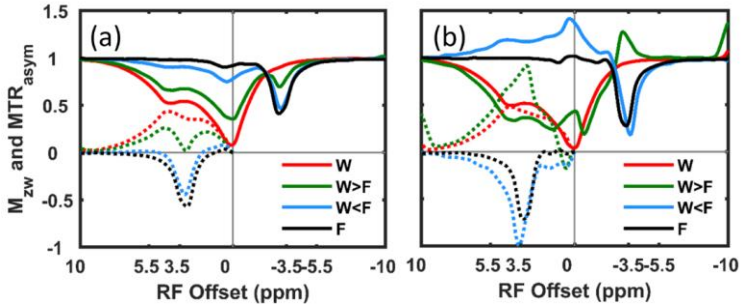

Figure 3-7 ROI averaged IP and OP Z-spectra and MTR_{asym} of iopamidol (pH 7.5)-oil phantom.

ROI averaged IP (a) and OP (b) Z-spectra and MTR_{asym} of the iopamidol pH 7.5-oil phantom (Phantom II).

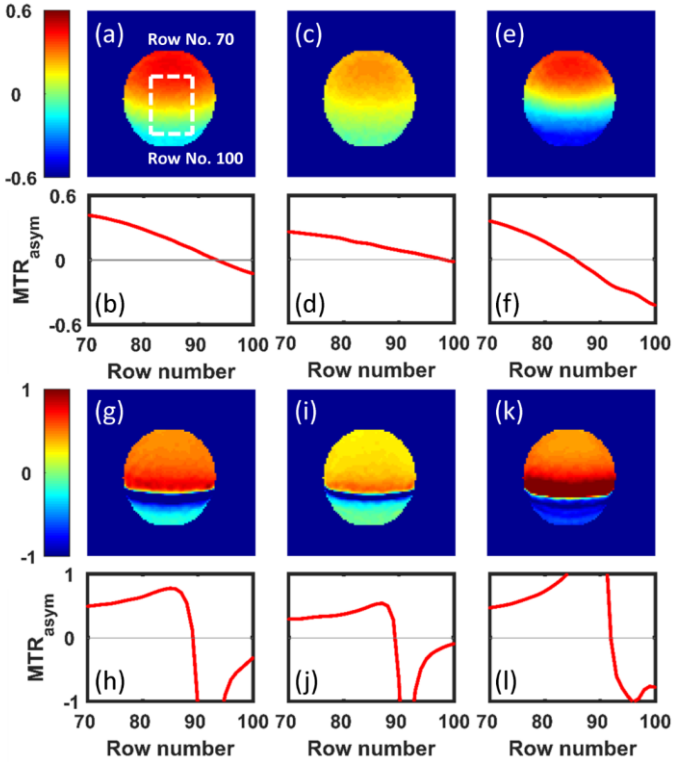

Figure 3-8 IP and OP CEST map and MTR_{asym} against FF of iopamidol (pH 7.5)-oil phantom.

The MTR_{asym} maps of the iopamidol pH 7.5-oil phantom (Phantom II) were generated by averaging the MTR_{asym} in three frequency ranges: 4.0 - 4.4 ppm (a, g), 5.3 - 5.7 (c, i) and 3.3 - 3.7 ppm (e, k) for both IP (a, c, e) and OP (g, i, k). The MTR_{asym} in each case are then averaged in the middle part of the CEST maps (vertical dashed line in (a), omitted in other images) row-by-row (horizontal dashed line in (a), omitted in other images) and plotted against the image row number (b, d, f, h, j, l). Part of the MTR_{asym} (very large negative and

positive values due to normalization to a reference signal close to 0) are not shown in (h, j, l) for display convenience.

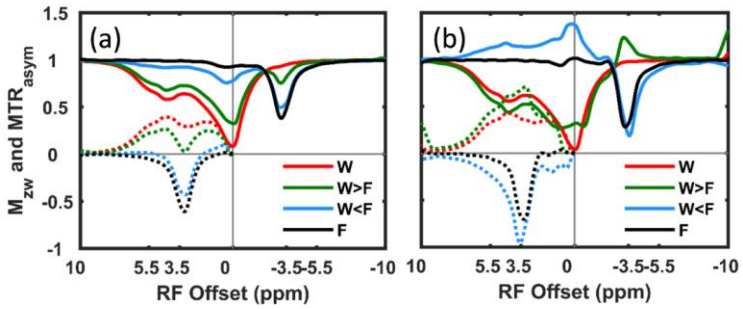

Figure 3-9 ROI averaged IP and OP Z-spectra and MTR_{asym} of iopamidol (pH 6.0)-oil phantom.

ROI averaged IP (a) and OP (b) Z-spectra and MTR_{asym} of the iopamidol pH 6.0-oil phantom (Phantom III).

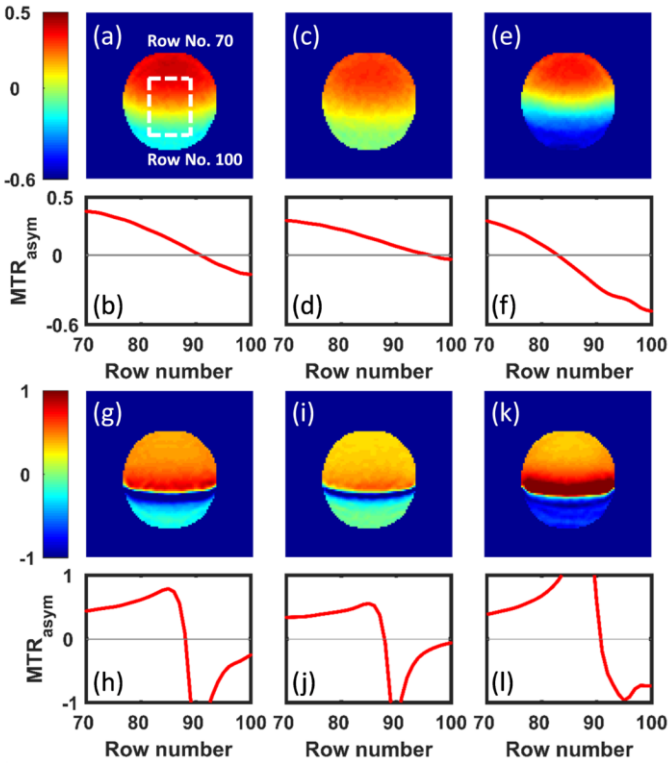

Figure 3-10 IP and OP CEST map and MTR_{asym} against FF of iopamidol (pH 6.0)-oil phantom.

The MTR_{asym} maps of the iopamidol pH 6.0-oil phantom (Phantom III) were generated by averaging the MTR_{asym} in three frequency ranges: 4.0 - 4.4 ppm (a, g), 5.3 - 5.7 (c, i) and 3.3

- 3.7 ppm (e, k) for both IP (a, c, e) and OP (g, i, k). The MTR_{asym} in each case are then averaged in the middle part of the CEST maps (vertical dashed line in (a), omitted in other images) row-by-row (horizontal dashed line in (a), omitted in other images) and plotted against the image row number (b, d, f, h, j, l). Part of the MTR_{asym} (very large negative and positive values due to normalization to a reference signal close to 0) are not shown in (h, j, l) for display convenience.

3.4.3 In vivo study

The representative in vivo IP and OP Z-spectra are shown in Figure 3-11. The Z-spectra were not normalized. The pixels were chosen on a straight line going from pure fat into pure fibroglandular tissue (Fig. 3-11k). Comparing Figures 3-2, 3-5 and 3-11, it is evident that the in vivo Z-spectra display exactly the same behavior as was predicted in simulations and phantoms.

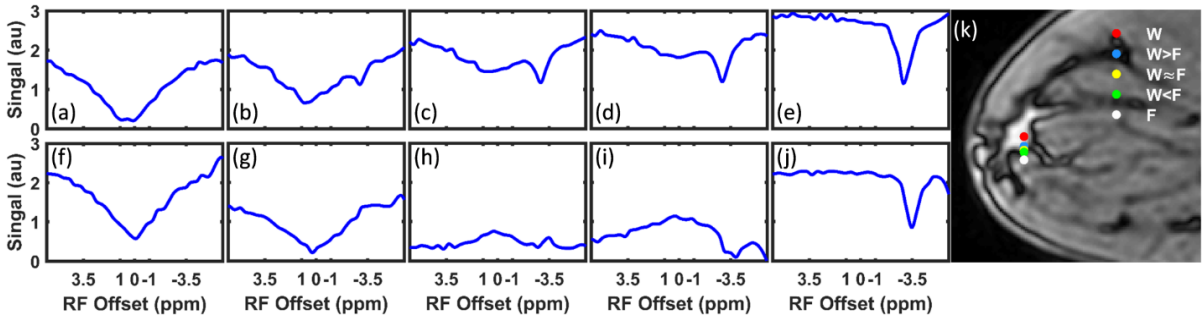

Figure 3-11 IP and OP Z-spectra for a healthy volunteer.
Representative IP (a-e) and OP (f-j) Z-spectra without normalization for different fat fractions from a healthy volunteer. The Z-spectra were from separate pixels shown as dots in the OP image acquired at TE = 3.45 ms (k).

3.5 DISCUSSION

In the simulations, the MTR_{asym} of the solute is only weakly influenced by fat, because the two pools are relatively far from each other (|2.4| ppm). The linear decrease of IP MTR_{asym} at both frequency ranges (Fig. 3-3a,b) is due to the monotonic decrease of the relative size of the water pool.

The intensity of the OP Z-spectrum at any frequency can be quantitatively explained by the equation: intensity = |Z-Intensity(water)-Z-Intensity(fat)|. Consider the reference signal: it is equal to the absolute value of fraction difference between water and fat; e.g. resulting in 0.4 in the cases of W > F (|0.7 - 0.3| = 0.4) and W < F (|0.3 - 0.7| = 0.4) and 0 in the case of W = F (|0.5 - 0.5| = 0). The reference signal may become lower than the rest of the Z-spectrum. For example, consider W > F and the saturation is at -3.4 ppm (labeled by Δ in Fig. 3-2g). Assuming that fat is fully saturated at this frequency while water is unperturbed, the OP Z-spectrum value becomes |0.7 - 0| = 0.7 which is larger than the reference signal value of 0.4.

In practice, the reference signal is always non-negative since magnitude images are used most of the time. Thus, the sign of MTR_{asym} before normalization determines the sign of the MTR_{asym} after normalization by the reference signal. The hydroxyl-MTR_{asym} becomes negative when the water "dip" at 0 ppm in the Z-spectrum changes to an "ascent" due to the increasing FF (Fig. 3-2f-i). At low FF, the amide-MTR_{asym} is positive because there is an "ascent" at the lipid frequency in the Z-spectrum (Fig. 3-2g-h); at larger FF, amide-MTR_{asym} becomes negative as Z-spectrum intensities form a "dip" around -3.4 ppm.

The oil used in the phantom study has multiple peaks (121). The main peak is at about -3.4 ppm, followed by the peaks of decreasing sizes at -3.8 ppm and 0.6 ppm. The experimental IP and OP images refer to the main peak of the oil. The other peaks may introduce additional asymmetry of the Z-spectrum as reflected in Figures 3-5, 3-7 and 3-9.

The field inhomogeneity was corrected using the B_0 maps generated by a sequence with two IP echoes. This method may not be as accurate as WASSR (41) in pixels without fat and underperforms in pixels with large FF. However, WASSR is suboptimal for B_0 correction in the images containing pixels with FF in the broad range, from 0 to 100%, since WASSR fails in voxels with little or no water.

Saturation parameters and the solute properties influence the Z-spectrum and the MTR_{asym}. However, as the simulations demonstrate, these parameters did not largely alter the overall behavior of the IP and OP MTR_{asym} against FF (122). While these parameters influenced the specific values of the MTR_{asym}, the overall trends (i.e. decreases with FF and singularity areas) remained the same. Thus, the explanation suggested above is largely valid.

Other experimental parameters including T_1, T_2, T_2*, excitation FA, and TR together determine the acquired signal (including the reference) and thus will further influence the Z-spectrum appearance. Moreover, presence of multiple fat peaks or multiple exchanging sites at high concentration may potentially lead to a non-zero reference signal at FF = 50% and smoothing of the singularities.

Two well-defined acquisition conditions, IP and OP, were investigated here. Other TEs will lead to a complicated behavior consisting of a mix of the effects. Moreover, while

quantification methods other than MTR_{asym} may be used successfully in IP Z-spectra to eliminated lipid/NOE peak (50), these methods would fail in the OP Z-spectra.

3.6 CONCLUSION

In conclusion, the study demonstrates that the TE and FF together determine the appearance of the Z-spectrum for gradient echo based sequences. Phantom and in vivo studies agree with the simulation. Although several lipid artifact removal methods were reported in CEST (3,50,109,110,123), additional studies are needed to examine the efficiency of various fat removal methods and their influence on the CEST contrast.

CHAPTER FOUR
CEST-Dixon for human breast lesion characterization at 3T

4.1 OVERVIEW

The majority of this work was accepted for publication in the Magnetic Resonance in Medicine 2018; 80(3):895-903. Portions of this work were presented at the 24th annual meeting of ISMRM in Singapore (May 2016), the Music City CEST in Nashville, TN, United States (August 2017) and the joint annual meeting ISMRM-ESMRMB in Paris, France (June 2018).

CEST MRI for breast lesion characterization is promising because CEST can provide molecular information which reflects tissue compositions. Therefore, incorporating CEST into breast cancer imaging protocol may lead to technology with improved specificity and prediction value. However, strong lipid signals lead to artifacts in breast CEST imaging. In this chapter, a CEST-Dixon imaging sequence for simultaneous water-fat separation and B_0 mapping was developed and used to characterize suspicious lesions in patients undergoing percutaneous biopsy. The CEST-Dixon sequence was validated in phantoms and in vivo. Five healthy volunteers and ten patients were scanned to compare the CEST contrast in three frequency ranges centered at 1, 2, and 3.5 ppm. The correlation between the CEST contrast and pathology markers (tumor type, estrogen receptor (ER) status, and Ki-67) was also investigated by stratifying the patients into ER-negative invasive ductal carcinoma (IDC) (more aggressive), ER-positive IDC (less aggressive), and benign groups.

4.2 INTRODUCTION

MRI has been adopted as both a screening tool for women at high risk for developing breast cancer as well as a diagnostic tool to evaluate the extent of disease in women recently diagnosed with breast cancer (124,125). Dynamic contrast-enhanced (DCE) breast MRI provides very high sensitivity but lacks specificity (126) as a result of significant overlap in the enhancement patterns of benign and malignant breast lesions (127). Multiple non-contrast imaging methods, such as spectroscopy and diffusion-weighted imaging, have been developed and applied to breast MRI in order to improve specificity and decrease false positive results when used either alone, or in combination with DCE-MRI (128).

Recently, CEST has been investigated for its feasibility and application in cancer imaging, because it provides information at the molecular level that reflects biochemical composition of tissues (10). Compared with spectroscopy, CEST has significantly improved sensitivity to certain metabolites and can achieve much higher spatial resolution, which is particularly desirable for clinical applications (10). APT neuroimaging, a sub-type of CEST imaging, is emerging as a powerful tool in the assessment of brain tumor aggressiveness and treatment response monitoring (48,49). Several previous studies in cells, animals, and humans applied CEST to breast malignancies also demonstrated the potential of CEST for tumor detection, characterization, and treatment assessment (50,100,108-110,116). Therefore, addition of CEST to current breast imaging protocols may potentially lead to technology with improved specificity and prediction value, while retaining excellent sensitivity.

Most of the reported studies on breast CEST imaging are preclinical or focus on imaging sequence implementation and/or optimization (100,109,110,116). Only two papers on CEST imaging have incorporated small number of breast cancer patients (50,108). Many questions need to be further investigated with regards to the application of CEST to breast malignancy, including how CEST contrast changes in breast tumors, which CEST frequency range has the highest correlation with malignancy, and what are the major contributors to CEST contrast in malignancy.

One of the largest challenges for successful breast CEST imaging is the presence of a large fat signal. Although the total amount of fat varies in the breast, fibroglandular tissue and fat are interleaved. Fat can confound CEST contrast, complicate Z-spectrum appearance and potentially lead to lipid artifacts and erroneous CEST effects (115,122). The influence of fat on CEST imaging has been discussed in details in the previous chapter (Chapter 3).

In this study, a CEST-Dixon method that employs the combination of CEST preparation with multi-point Dixon water-fat separation (112,129) to obtain water-only CEST images (123,130) is discussed. These water-only images are used to calculate MTR_{asym} maps in three CEST frequency ranges for normal tissues and suspicious lesions. Biopsy results were used as the gold standard for method evaluation. The goal of the study includes three aspects: 1) to implement and validate the CEST-Dixon sequence in human subjects at 3 T for simultaneous water-fat separation and B_0 mapping, 2) to compare the CEST contrasts in normal breast tissues with that of malignant and benign tissues in three CEST frequency ranges, and 3) to determine if the CEST-Dixon method could be used to assess tumor status

using several standard biopsy pathology markers (ER and Ki-67 (131)) as reference standards.

4.3 METHODS

4.3.1 Phantom

To investigate whether CEST-Dixon introduces additional asymmetries in the Z-spectrum, iopamidol (Isovue-300, Bracco Diagnostics, Milan, Italy) phantoms at pH 6.0, 6.5, 7.0 and 7.5 were prepared and transferred to small vials. A vial containing vegetable oil (Crisco, the J.M. Smucker Co, Orrville, OH) was used as a fat reference. A vial of distilled water was prepared as a control. The vials were held in a plastic container that was filled with tap water to minimize B_0 inhomogeneity.

4.3.2 In vivo study

The study was approved by the local Institutional Review Board (IRB) and performed in accordance with the guidelines. Written consent was obtained from each subject. 5 female volunteers without known breast diseases and 10 female patients with suspicious breast lesions for which biopsy was recommended were recruited for the study. The patients were scanned prior to biopsy and the diagnostic “gold standard” was provided via clinical pathology results, which included 8 malignancies and 2 non-malignant lesions. The

confirmed malignancies included 6 invasive ductal carcinoma (IDC), 1 IDC and encapsulated papillary carcinoma (EPC), and 1 invasive mucinous carcinoma (IMC) (Table 4-1). The non-malignant lesions included 1 atypical ductal hyperplasia (ADH) and 1 fibroadenoma (Table 1). Only one lesion was scanned per patient. Patient 7 was excluded from the analysis due to observable motion associated with the tumor that was located close to the chest wall. Patient 8 was excluded from the analysis due to the small size of the lesion (which at the acquired image resolution (2 × 2 mm^2) resulted in partial volume effects and only few pixels for the ROI analysis). Patient 2 was excluded from the analysis because IMC and IDC are two different tumor types. Thus, the analysis included 5 healthy volunteers and 7 patients with suspicious breast lesions in total. The patients are further stratified into three groups: ER-negative (ER-) IDC group (Patients 1 and 3, N = 2), ER-positive (ER+) IDC group (Patients 4-6, N = 3) and benign group (Patients 9 and 10). The ER- breast cancer lack the estrogen receptor which is an index for sensitivity to endocrine treatment and is more aggressive than the ER+ breast cancer (132).

Table 4-1 Pathology data and CEST MRI results.

							MTR_{asym} (%)		
Patient	Diagnosis	Grade[a]	ER	PR	HER2	Ki-67 (%)	(1 ppm)	(2 ppm)	(3.5 ppm)
1	IDC	G3	–	1–2%, weak +	–	80-90	5.2 ± 5.0	6.3 ± 4.6	3.3 ± 4.5
2	IMC	G1	+	+	–	20-25	13.6 ± 6.3	8.9 ± 5.9	4.4 ± 5.4
3	IDC	G2	–	–	–	70-80	5.0 ± 2.0	4.0 ± 2.3	2.5 ± 1.8
4	IDC+EPC	G2	+	+	–	2-5	–1.3 ± 1.4	0.2 ± 0.9	–0.8 ± 4.5
5	IDC	G1	+	+	–	5	0.8 ± 2.9	1.8 ± 2.4	1.6 ± 1.5
6	IDC	G2	+	+	–	10	–0.5 ± 5.3	1.8 ± 6.1	–2.5 ± 4.6
7	IDC	G3	–	–	–	>95	-	-	-
8	IDC	G2	+	+	–	15	-	-	-
9	ADH	-	-	-	-	-	–1.2 ± 1.5	0.7 ± 1.3	–0.5 ± 3.6
10	Fibroadenoma	-	-	-	-	-	0.8 ± 1.7	2.7 ± 1.8	1.6 ± 2.1

[a]Nottingham grade.

PR, progesterone receptor; IMC, invasive mucinous carcinoma; EPC, encapsulated papillary ductal carcinoma; ADH, atypical ductal hyperplasia.

4.3.3 MRI

A 3 T human scanner (Ingenia, Philips Healthcare, Amsterdam, the Netherlands) with dual-channel body transmit coil was used throughout the study. The phantom data were acquired using a 15-channel head-spine coil. The CEST preparation consisted of 10 HS pulses, each 49.5 ms long, FA of 900° and with a delay of 0.5 ms between the pulses. The total saturation time was 500 ms and $B_{1,CW}$ = 1.2 μT. The CEST images were acquired using 2D 3-point multi-echo Dixon sequence with TR/TE_1/ΔTE = 4.8/1.33/1.1 ms, FA = 45° and centric k-space ordering. The Dixon acquisition was based on a multi-shot multi-echo T_1-weighted TFE sequence. We chose 3 echoes (3-point Dixon method, Fig. 4-1), since it is the minimal number of the echoes required to obtain water, fat and B_0 information. 41 offsets were acquired in the Z-spectrum from -10 ppm to 10 ppm and 1 reference image was acquired. The FOV was 220 × 220 mm^2 with a voxel size of 1.5 × 1.5 mm^2 and a slice thickness of 8 mm.

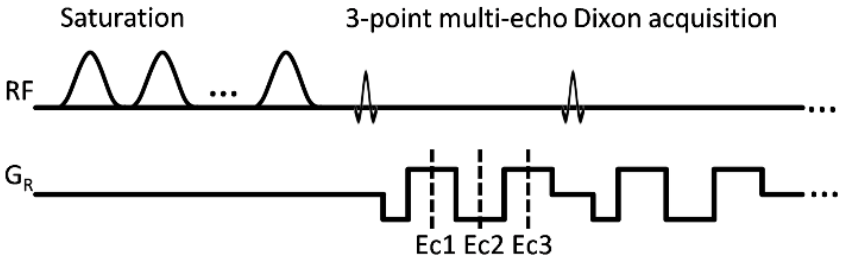

Figure 4-1 Schematic of the CEST-Dixon sequence.
A 3-point multi-echo Dixon is used for image acquisition following the CEST preparation. G_R: readout gradient. Ec: echo.

The human data were acquired using a 16-channel bilateral breast coil. A 3D fat-suppressed enhanced T_1 high-resolution isotropic volume excitation (eTHRIVE) sequence with a resolution of $0.6 \times 0.6 \times 1$ mm^3 was used for anatomical images. The imaging slice was placed for optimal observation of the fibroglandular tissue and/or the suspicious lesion based on the eTHRIVE images. The CEST preparation and acquisition was the same as the phantom experiment except for the following parameters: $TR/TE_1/\Delta TE = 5.1/1.57/1.1$ ms, FA = 10° and 33 offsets were acquired in the Z-spectrum from -6 ppm to 6 ppm. The FOV was varied according to the volunteer size, but the in-plane resolution was fixed at 2×2 mm^2 and the slice thickness was 5 mm. Transverse bilateral images were acquired. The data from the first two patients were acquired with SENSE = 4 and multi-shot factor 14 and the total scan time 1 min 10 s. All the other volunteer and patient data were acquired without SENSE and using multi-shot factor 25 to improve SNR, and the total scan time was 2 min 26 s.

4.3.4 Data analysis

Six types of images were obtained using the Dixon method for each frequency offset: 1) the source images (three images total, one per TE), 2) the water-only image, 3) fat-only image, 4) IP image, 5) OP image, and 6) the B_0 map. Standard single-peak lipid Philips reconstruction protocol was used to obtain water-only, fat-only, IP, OP and B_0 images from the source images.

Phantom studies: To investigate whether CEST-Dixon introduces additional asymmetries in the Z-spectrum, the MTR_{asym} at 1.8, 4.2 and 5.5 ppm (133) calculated from

the CEST images acquired with and without Dixon were compared in the phantom study. The second echo source images (TE = 2.43 ms, close to IP) were chosen to serve as a standard, non-Dixon CEST images for the comparison. The Dixon CEST images were the water-only images.

In vivo studies: The water-fat separation of the CEST-Dixon method was validated in vivo by comparing the Z-spectra from the CEST images acquired with and without Dixon for pixels of different fat fractions. Same as the phantom study, the second echo source images (TE = 2.67 ms, close to IP) were chosen to serve as the non-Dixon CEST images and the water-only images were the Dixon CEST images.

The water-only CEST images were processed on a pixel-by-pixel basis using custom Matlab (The Mathworks, Natick, MA) routines. Field inhomogeneity was corrected using an averaged B_0 map generated by averaging the Dixon B_0 maps of all frequency offsets. MTR_{asym} was used for CEST signal measurement. For in vivo studies, the MTR_{asym} were averaged in the ROIs and in the three frequency ranges: 1) 0.8-1.2 ppm, 2) 1.8-2.2 ppm, and 3) 3.3-3.7 ppm and denoted hydroxyl, amine and amide MTR_{asym} respectively.

ROI placement - Healthy volunteers: ROIs of the fibroglandular tissue of the healthy volunteers were made based on the signal intensities of the water-only and fat-only images (50). First, a threshold was selected to exclude the background noise in both water-only and fat-only images. The two masks were then overlapped to locate the pixels affected by partial volume effects and with high FF. The fat fraction was calculated pixelwise based on the water-only and fat-only images: FF = F/(W+F). The high FF pixels were removed from the

mask based on the water-only image. Next, skin, chest wall and heart were removed from the mask manually to generate the final mask for the fibroglandular tissues.

ROI placement - Patient volunteers: The tumor ROIs were drawn manually by a fellowship-trained breast imaging radiologist with 5 years of experience based on the water-only images while referring to the high resolution eTHRIVE images. The final tumor and fibroglandular tissue ROIs were reviewed and approved by the radiologist.

4.3.5 Statistical analysis

A weighted Least Squares Linear fit was performed for the correlation between MTR_{asym} and Ki-67 level with the inverse of the square of the standard deviation used as the weighting factor (134), and a $p < 0.05$ was considered statistically significant.

4.4 RESULTS

Figure 4-2 compares the MTR_{asym} at 1.8, 4.2 and 5.5 ppm of the water and iopamidol phantoms calculated from the images acquired with and without Dixon. The non-Dixon and Dixon images refer to the second echo source image and water-only images. As shown in Figure 4-2, the MTR_{asym} with and without Dixon are similar for all the phantoms and frequencies, although Dixon results showed slightly increased effect in the iopamidol solutions (the values are still within the experimental error of each other).

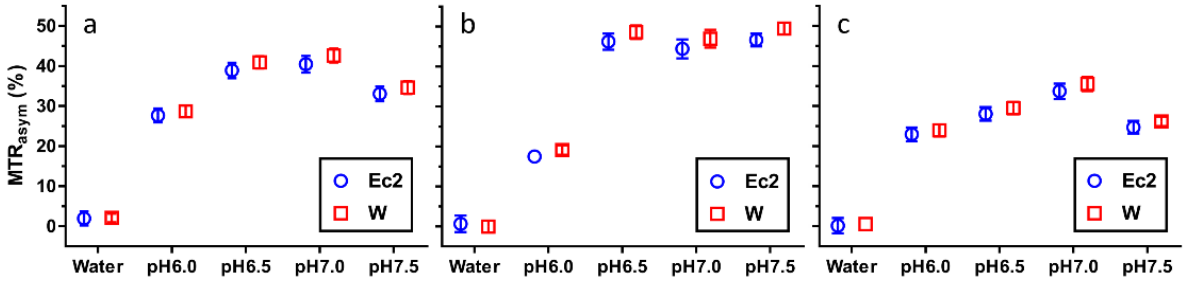

Figure 4-2 MTR_{asym} of the water and iopamidol phantoms with and without Dixon. MTR_{asym} at 1.8 ppm (a), 4.2 ppm (b) and 5.5 ppm (c) for water and iopamidol solutions of different pH with and without Dixon. The non-Dixon and Dixon images were the second echo source images (Ec2) and water-only images (W) respectively.

To validate the water/fat separation of CEST-Dixon method, Figure 4-3 shows the three types of images obtained from a healthy volunteer: the second echo source image, water-only and fat-only images. Water-only and fat-only images are of a good quality, and provide a clear separation of water and fat signals (Fig. 4-3n, o vs m). Figure 5-3 also shows the in vivo Z-spectra for single pixels with different fat fractions in the 3 types of images. The selected single pixels are shown as colored dots in Figure 4-3h inset. The pixels were selected from a straight line going from fibroglandular tissue to the fat with an increasing fat fraction along the line. Hence, the water only pixel was from the fibroglandular tissue, the fat only pixel was from the fat tissue and the pixels with mixed water fat signals were selected at the interface of the two tissues. Since the second echo source images (TE = 2.67 ms) were closer to IP images, the water dip in the Z-spectra decreases while the fat dip increases as the fat fraction increases (Fig. 4-3a-d) (122). The corresponding water-only and fat-only Z-spectra are shown in the Figure 4-3e-h and Figure 4-3i-l respectively. It can be seen that the water and fat dips were successfully separated, though some residual fat signals were observed in high fat fraction (Fig. 4-3g arrow). The Z-spectra were not normalized to the

reference in this figure to better display the pixels whose signal intensities were close to noise level: fat-only pixel in the water-only images (Fig. 4-3h) and the water-only pixel in the fat-only images (Fig. 4-3i).

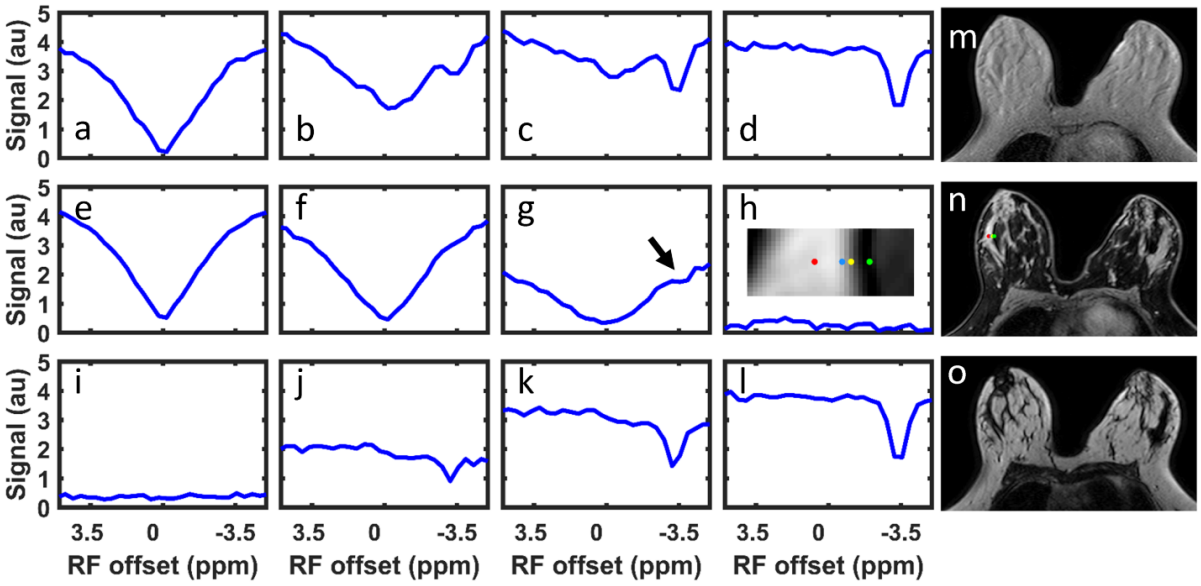

Figure 4-3 In vivo Z-spectra with different FF of Ec2 source image, water-only and fat-only images.
In vivo Z-spectra without normalization (a-l) and corresponding images (m-o) of a healthy volunteer in 3 types of images: second echo source image (a-d, m), water-only (e-h, n) and fat-only (i-l, o). The Z-spectra were from separate single pixels with different fat factions: water only (W: a, e, i), water fraction larger than fat (W > F: b, f, j), fat fraction larger than water (F > W: c, g, k) and fat only (F: d, h, l). Selected single pixels with different fat fractions are shown as colored dots in the water-only image (n) and in the zoomed-in inset in (h): red: W, blue: W > F, yellow: W < F and green: F. The arrow in (g) indicates the residual fat signal.

Figure 4-4 shows the amide CEST maps with and without Dixon and the corresponding whole fibroglandular tissue ROI averaged Z-spectra and MTR_{asym} of the same healthy volunteer as Figure 4-3. Here, the ROI encompassing the whole fibroglandular tissue was generated as described above ("Methods, ROI placement - healthy volunteers") and is

shown in Figure 4-4g. The non-Dixon images refer to the second and first echo source images, which are close to the IP (TE = 2.67 ms) and OP (TE = 1.57 ms) images, respectively. Dixon results shown are the water-only images. As shown in Figure 4-4a, in non-Dixon image, a large number of pixels in the amide CEST map have negative values due to the presence of fat (122). Correspondingly, a fat dip is observed in the Z-spectrum, leading to negative amide MTR_{asym} (Fig. 4-4b). Non-Dixon images acquired close to OP condition lead to curious looking Z-spectrum and erroneously high MTR_{asym} (Fig. 4-4d,c) due to signal interferences and normalization that was discussed in the previous chapter (Chapter 3) (122). At the same time, in the water-only Z-spectrum (Fig. 4-4e), the fat dip is removed, producing the amide MTR_{asym} and CEST map (Fig. 4-4e,f) essentially free of fat influence. To demonstrate the degree of B_0 inhomogeneity that is obtained in a typical case, Figure 4-4h shows the average B_0 map obtained in the same healthy volunteer. Large deviations in the homogeneity spanning a range from +200 to -200 Hz can be observed.

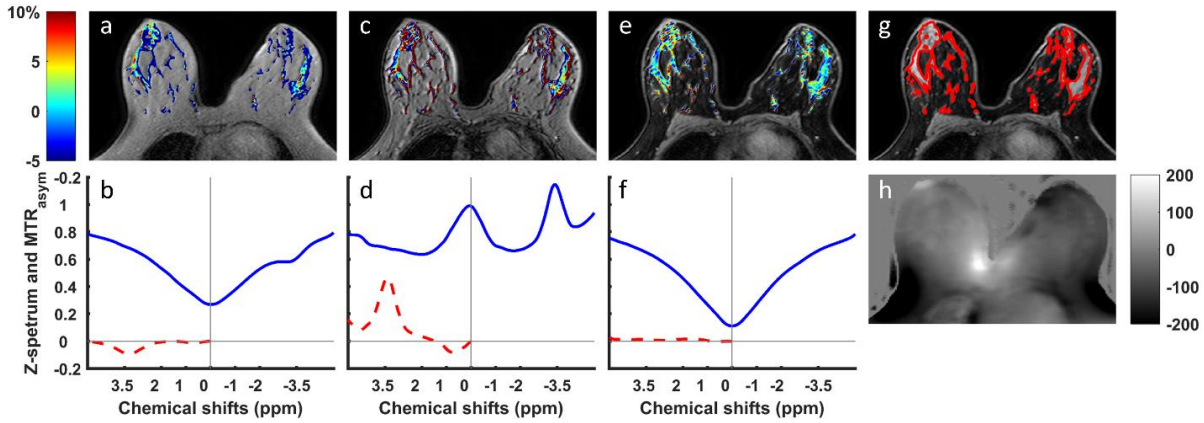

Figure 4-4 In vivo amide CEST maps, the corresponding Z-spectra and MTR_{asym} with and without Dixon.

Amide CEST maps (a, c, e), the corresponding Z-spectra and MTR_{asym} (b, d, f) with (e, f) and without Dixon (a-d), ROI encompassing all fibroglandular tissue in red (g) and

corresponding B_0 map (h). The non-Dixon and Dixon images refer to the second echo source image (a) or first echo source image (c) and water-only image (e). The CEST maps are overlaid on the corresponding reference images: using second echo (a), first echo (c) or water-only (e). The ROI is outlined in red on water-only image in (g).

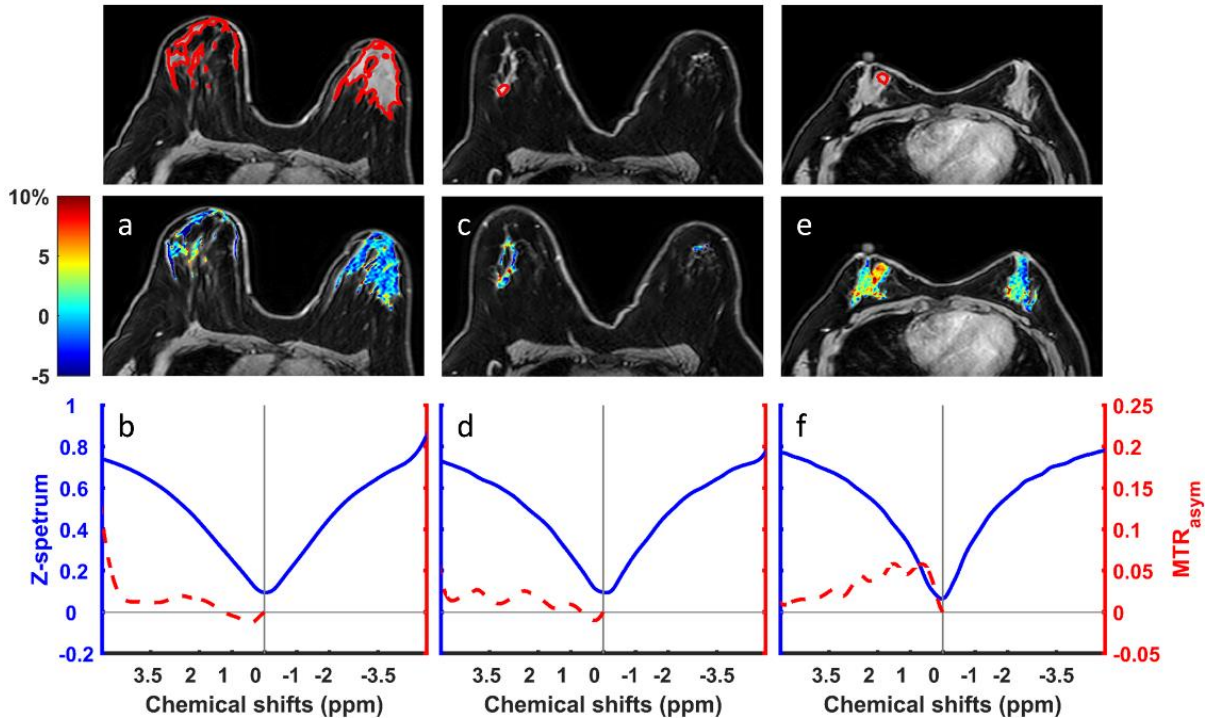

Figure 4-5 In vivo hydroxyl CEST maps ROI averaged Z-spectra and MTR_{asym} for a healthy volunteer, an ER- IDC patient and an ER+ IDC patient.
Hydroxyl CEST maps and ROI averaged Z-spectra (blue) and MTR_{asym} (red) for a healthy volunteer (a, b), invasive ductal carcinoma, not otherwise specified (IDC NOS) patient (c, d, Patient 5 in Table 5-1) and a triple-negative breast cancer (TNBC) patient (e, f, Patient 3 in Table 5-1). Note different y-scale for Z-spectra (blue) and MTR_{asym} (red). CEST maps in (a, c, e) are overlaid on the reference water-only images. The panels above (a, c, e) show the corresponding ROIs in red: (b) was averaged across the fibroglandular tissues of both breasts; (d, f) were averaged in the tumor areas as indicated by the ROIs. See Methods section for more details on the ROI placement.

Figure 4-5 shows the representative water-only Dixon hydroxyl CEST maps and ROI averaged Z-spectra and MTR_{asym} for a healthy volunteer (Fig. 4-5a,b), an IDC, Not Otherwise Specified (NOS), ER+ patient (Fig. 4-5c,d) and a triple-negative breast cancer

(TNBC) patient (Fig. 4-5e,f). The Z-spectrum and MTR_{asym} of the healthy volunteer was averaged across the fibroglandular tissue of both breasts (Fig. 4-5b). The Z-spectra and MTR_{asym} of the patients were averaged in the tumor areas (Fig. 4-5c,e). The MTR_{asym} in the three CEST frequency ranges of all the subjects are summarized in Figures 4-6 and 4-7. When the malignant lesions are stratified by ER status, it can be seen that the ER- IDC group exhibits higher CEST effects in all the three frequency ranges than the ER+ IDC, benign and normal groups (Fig. 4-6). For the three frequency ranges, the ER+ IDC, benign and normal groups tend to have similar CEST effects which suggest that the ER+ IDC group is indistinguishable from normal and benign groups. Moreover, the hydroxyl range has the largest difference between the ER- IDC and the other groups. Hence, Figure 4-5 displays hydroxyl MTR_{asym}. When not stratified by ER status, although the IDC group displays higher MTR_{asym} in hydroxyl and amine ranges than the other groups, the deviations across subjects for all frequencies increase and the differentiability between the IDC group and the benign and normal groups reduces (Fig. 4-7).

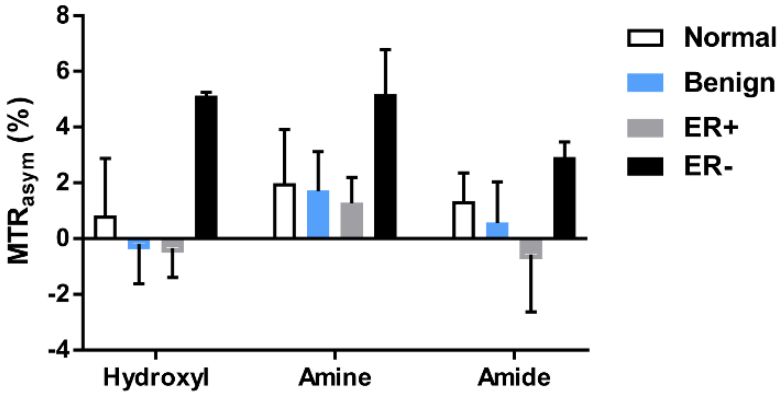

Figure 4-6 MTR_{asym} averaged in three frequency ranges for normal, benign, ER+ IDC and ER- IDC groups.

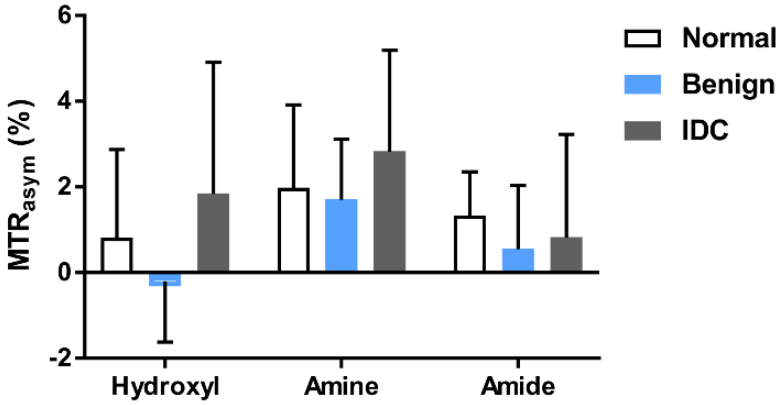

Figure 4-7 MTR_{asym} averaged in three frequency ranges for normal, benign and IDC groups.

In Figure 4-8, the tumor MTR_{asym} in the three frequency ranges are plotted against the Ki-67. It can be seen that the MTR_{asym} increases as Ki-67 level increases for all frequency ranges. The R^2 values were 0.95, 0.87 and 0.36 for hydroxyl, amine and amide frequency ranges, respectively.

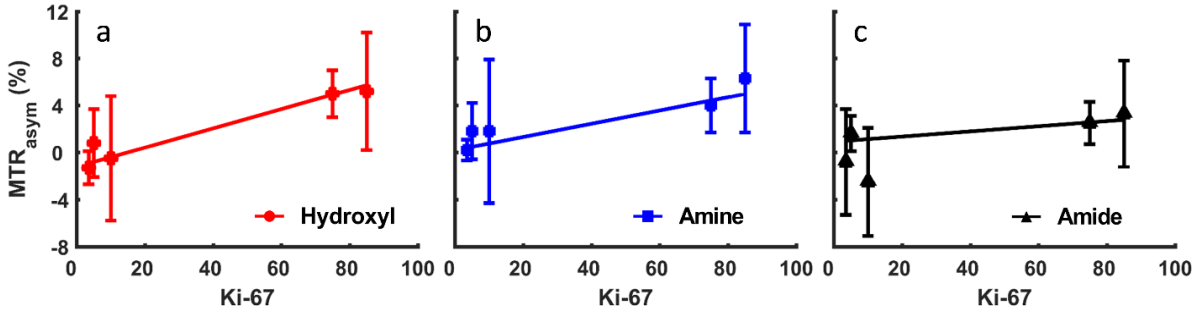

Figure 4-8 Hydroxyl-, amine- and amide-MTR_{asym} against Ki-67 level.
MTR_{asym} averaged in the hydroxyl (a), amine (b) and amide (c) frequency ranges against Ki-67 level. The R^2 are 0.95, 0.87 and 0.36 for hydroxyl, amine and amide groups respectively.

Figure 4-9 displays the MTR_{asym} in the three frequency ranges for all subjects, similar to Figure 4-6, but using the second echo source images. The hydroxyl and amine ranges still have the highest values in the ER- IDC group, however the amine MTR_{asym} had decreased in ER+ IDC, benign and normal groups (Fig. 4-9 vs Fig. 4-6). This is due to the influence of the lipid signals on the amine frequencies. Moreover, the APT signal becomes negative for normal, benign and ER+ lesions, due to increased negative lipid contribution.

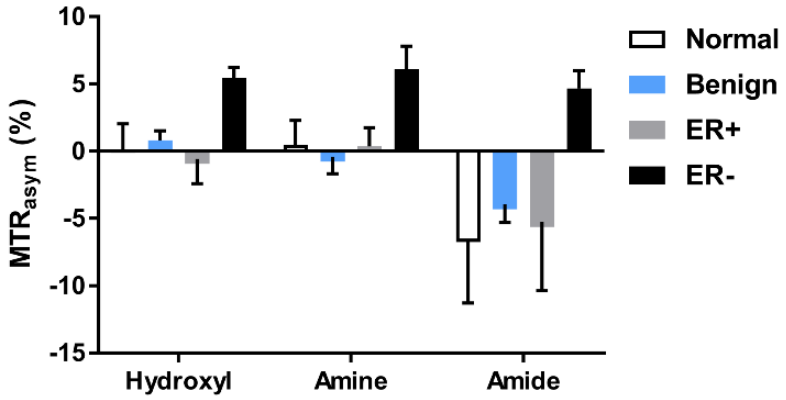

Figure 4-9 MTR_{asym} averaged in three frequency ranges for normal, benign, ER+ IDC and ER- IDC groups without Dixon.
The non-Dixon images were second echo source image.

4.5 DISCUSSION

The presence of strong lipid signals is a big challenge for body CEST imaging because fat can lead to erroneous CEST contrast. CEST-Dixon offers attractive approach around this obstacle. The B_0 maps derived from the Dixon technique can be used for field inhomogeneity correction, without the need for a separate B_0 mapping sequence. In this

study, a 3-point multi-echo Dixon is used for image acquisition. 3 TE values were chosen because this is the least number of echoes needed to robustly separate water, fat, and B_0. ΔTE was adjusted to the minimum possible value to reduce potential artifacts caused by phase-wrapping.

The CEST-Dixon method was validated in phantoms and in vivo. In the phantom experiment, the MTR_{asym} with and without Dixon are similar (Fig. 4-2) indicating that the Dixon water/fat decomposition does not introduce additional asymmetries to the Z-spectrum. The vial containing fat only was not visible in the water-only images. Moreover, Figure 4-2 indicates that MTR_{asym} measurements using Dixon images lead to slightly reduced standard deviation. This might be due to the multi-point Dixon post-processing involving 3 echoes acting similar to averaging, thus increasing SNR.

The in vivo results of the healthy volunteers show successful water-fat separation (Fig. 4-3m-o). However, in some of the pixels with high fat fraction (approximately > 50%), the lipid peak was still detectable in the water-only images (Fig. 4-3g, arrow), albeit much smaller than what is observed in the non-Dixon image (compare Figs. 4-3c versus g). This residual fat contribution in the Z-spectrum would be magnified by normalization (122), hence, MTR_{asym} distortions might still be observed. For this reason, in this preliminary study, the pixels with high fat fraction were removed from the ROIs to avoid the influence of the residual fat. While we cannot conclusively indicate the origin of this residual artifact, partial volume effects might be a contributing factor (50). Another factor should also be considered: the fat-water separation model of multi-point Dixon post-processing assumes non-saturated water and fat peaks, which is not true in CEST. Also, since the single-peak model for fat was

used in the image reconstruction, other fat peaks would remain in the Z-spectrum and introduce additional asymmetries, especially the second and third largest fat peaks which lie about 3.8 ppm upfield and 0.6 ppm downfield respectively may influence the amide and hydroxyl MTR_{asym} accordingly. Additional investigation is needed on the influence of the saturation and multi-peak versus single-peak modeling on CEST-Dixon method. Finally, it might be a contribution from the true relayed NOE, cleared from the artifact contribution of the saturated, but non-exchanging lipids.

Figure 4-4e,f demonstrates that despite some residual problems described above, CEST-Dixon leads to a smoother Z-spectrum in the normal fibroglandular tissue and while residual lipid artifacts might be observable in some pixels, overall their influence is removed. Moreover, the Z-spectrum from water-only images displays higher suppression levels near water resonance, almost zero, as should be expected (Fig. 4-4f). While second echo (close to IP) leads to higher values close to water resonance, due to fat signal contribution (Fig. 4-4a).

Following validation of the CEST-Dixon method in the healthy volunteers, a preliminary study was conducted in the small group of patients with suspicious breast lesions identified at mammography and ultrasound. Figures 4-5, 4-6 and 4-7 demonstrate that the MTR_{asym} in the healthy fibroglandular tissue is generally low, around 2% for all three frequency ranges. Compared to the previously reported human breast studies at 3 T, the amide MTR_{asym} is slightly lower than the previously reported values (50,109), however MTR_{asym} at 1.2, 1.3 and 1.8 ppm reported earlier was mostly negative (108), presumably due to lipid contribution. The standard deviations within ROI that included whole fibroglandular tissue (with high fat fraction pixels excluded), were around 4% (with minimum 2% and

maximum 5% observed). This relatively large standard deviation is in line with previous CEST measurements in breast at 3 T and at 7 T (50,109,110).

Table 4-1 lists MTR_{asym} values measured in the patients. The standard deviations with ROIs are similar to the ones observed in healthy volunteers. The data was stratified by ER status (ER- vs ER+). Figure 4-6 suggests that such stratification provides differentiation between the more aggressive and less aggressive cancer groups. In ER- IDC tissues, there is a trend towards increased MTR_{asym} compared to the ER+ IDC, benign and normal tissues especially in the hydroxyl and amine ranges (Fig. 4-6). The ER+ IDC and benign lesions demonstrate MTR_{asym} values close to normal fibroglandular tissue in all three frequency ranges. When both ER statuses are grouped together, the trend of increased MTR_{asym} in the IDC group, as compared to the other groups, can still be seen in the hydroxyl and amine ranges, however this trend is reduced (Fig. 4-7). In the amide range, the IDC group becomes indistinguishable from the benign and normal groups (Fig. 4-7). Although the sample sizes are very small, this preliminary data reiterates important potential for CEST MRI to differentiate more aggressive from less aggressive breast cancers.

A statistically significant correlation was observed between Ki-67 and MTR_{asym} in all three frequency ranges with the most significant correlation for hydroxyl MTR_{asym} and amine MTR_{asym} close behind (Fig. 4-8). Our study is small and the Ki-67 values reported here do cluster at the low and high end. Nevertheless, to the best of our knowledge, correlation of Ki-67 and APT was observed previously in animal model of brain cancer (107), but our results are the first to demonstrate such correlation in humans. High Ki-67 indicates increased cell proliferation. While it is not an accepted marker of breast cancer aggressiveness, it is one of

the standard pathological indices evaluated for patient care and is associated with more aggressive cancer types (135). The observed correlation is in agreement with our previous observations, indicating a trend of increased CEST contrast in more aggressive tumors. While larger studies are needed to validate this result, it indicates the potential of CEST MRI to provide important information on the molecular level that could complement and improve specificity of current breast MRI protocols.

Following stratification by sub-types, the largest MTR_{asym} values were observed in hydroxyl and amine ranges. Moreover, the largest difference between ER- IDC vs ER+ IDC, benign and normal values was observed in hydroxyl MTR_{asym} (Fig. 4-6), and the strongest correlation with Ki-67 was also observed in hydroxyl and amine ranges (Fig. 4-8). Previous studies did not differentiate by tumor types, but Ref. (108) had also demonstrated increased hydroxyl MTR_{asym} in malignancy, in general agreement with our observations (Fig. 4-7). Moreover, the focus on hydroxyl and amine range is in agreement with recent studies in cells and animal models that also focused on the hydroxyl MTR_{asym} (100,116). The origins of the increased CEST contrast in the hydroxyl range (or in 1.2 - 1.8 ppm range as in (108)) were attributed to the increase in the glycosaminoglycan concentration (110), alterations in mucin (116) or products of choline metabolism (100,102,108). Moreover, our observations seem to suggest an increase in hydroxyl MTR_{asym} associated with more aggressive metabolism as indicated by ER status and Ki-67 (Figs. 4-6 and 4-8). This deviates from the animal model observations, where a decrease in hydroxyl MTR_{asym} was associated with more aggressive cancers (100,116). At the same time, the very large hydroxyl MTR_{asym} (13.6%) observed in the mucinous carcinoma case (Patient 2, Table 4-1) supports the sensitivity of CEST MRI to

mucin concentration as suggested previously (116). More studies are required, in cells, animal models and humans to address the origins of the CEST changes in breast malignancy. Figures 4-6 and 4-8 suggest that APT signal, which was proven to be the best for monitoring of brain malignancies (2), might be less suitable for the monitoring of malignant alterations in breast. It should be noted, that the purpose of our study here was not to fully address these important questions, but to provide a new tool for the assessment of breast malignancy at 3 T.

In this preliminary study, statistical analyses were not performed for Figures 4-6, 4-7 and 4-9 due to the small the number of the subjects. In Figures 4-6 and 4-9, the number of each group is further reduced when the tumors are stratified by ER status. However, the results do reflect the trend of change in the CEST contrast indicating the potential of CEST imaging in tumor characterization. Currently, a study using improved breast CEST imaging protocol on more subjects is ongoing.

Figure 4-9 is analogous to Figure 4-6, but using non-Dixon, second echo source images. The influence of fat on the APT signals in normal, benign and ER+ IDC groups is obvious, with the signals becoming negative. The standard deviations also increase in all the three frequency ranges. Figure 4-6 clearly demonstrates importance of the efficient water-fat separation in the breast CEST studies and advantage of Dixon method in conjunction with CEST.

Application of multi-echo acquisition and Dixon post-processing has another advantage, even in the areas void of fat: it provides embedded B_0 map acquired at the same time as CEST. Careful B_0 correction is essential for accurate CEST mapping, especially at the lower 3 T field and for resonances close to water (i.e. hydroxyl). Great effort is dedicated

to careful B_0 mapping, however there are unavoidable uncertainties when separate B_0 map is acquired (using gradient echoes or WASSR (41)), associated with subject's motion between scans and changes in hardware temperature and water frequency drift. Dixon method used here eliminated many of the uncertainties and provided perfectly registered, dynamically updated B_0 maps.

Since all the echoes are acquired in the same shot (Fig. 4-1), the use of multi-echo Dixon method does not add to the total scan time. Our implementation took about 2.5 min, equivalent to the acquisition time of a standard gradient echo sequence. Moreover, some time was saved by not acquiring a separate B_0 map, which typically takes ~30 s. While motion was not a problem in most of the cases, it could be a problem for lesions close to the chest wall, as was the case for Patient 7 (Table 4-1). In such cases breathing-synchronization strategies and motion post-processing could be employed (136).

Fat suppression in breast imaging can be challenging (137). First, B_0 inhomogeneity is large, deteriorating efficacy of the spectral-selective pulses used in selective fat suppression and SPIR methods. Second, B_1 inhomogeneity creates challenges for inversion pulses (such as in spectral presaturation with inversion recovery (SPIR) and short TI inversion recovery (138)). Finally, fat signal composed of multiple fat components with different T_1s, challenging the SPIR and STIR implementation. In comparison, the Dixon method is insensitive to B_0 and B_1 inhomogeneities (139,140). Moreover, combination of CEST with Dixon avoids interferences of the preparation pulses (and their imperfections) with the CEST saturation train and does not add to the total SAR, which could already be

high. Thus, there are numerous potential advantages to using Dixon methods with CEST in breast.

Here, we used the simplest MTR_{asym} analysis. Another alternative to fat suppression could be advanced post-processing using multi-Lorentzian (43) or other model-based fittings. Such methods could offer the advantage of quantitative information on different exchanging moieties. However, IP images have to be acquired to ease fitting, or, the influence of the echo timings (122) should be included in the fitting model. Moreover, multi-Lorentzian fitting is model- and pool number dependent and require sophisticated off-line post-processing. In contrast, all human commercial scanners have at least three-echo version of the Dixon acquisition and post-processing implemented (such as the one that was used here). It is also tempting to speculate that the sequence could be used to differentiate lipid artifact stemming from saturation of non-exchanging fat from relayed NOE occurring via dipolar interaction and exchange with water molecules (113).

Small lesions could still be challenging to detect and analyze, as was the case with Patient 8. The partial volume effects pose the same problem for all imaging methods employed in breast, independent of what fat suppression method is used.

Finally, a technical limitation of the study should be noted. A bilateral imaging protocol has been employed, while unilateral may provide better B_1 homogeneity. Also, in this preliminary study we have chosen B_1 field of 1.2 μT. This value was selected based on an approximate optimization in two patients, previous brain studies and reports of breast studies in literature (50). Optimal B_1 value depends on the exchange rate and, thus, may depend on which group is chosen for observation. Previous human studies had focused on

APT (50,109), however cell and animal studies indicated higher dependence on hydroxyl protons (100,116), as discussed above. The preliminary results also indicated increased differences in hydroxyl region. Thus, lower power and a more selective pulse is used. Moreover, total saturation length was 500 ms, which is the longest allowed in standard RF amplifier operating mode on clinical MR scanners. However, it is known that longer RF saturation leads to improved CEST effect. Based on the preliminary results presented here, we can conclude that hydroxyl range shows promise to be most sensitive to the important malignant alterations. Thus, we are conducting further optimization of the saturation protocol, in terms of length and RF power, using alternating transmit to achieve prolonged saturation (91) (> 500 ms) and using unilateral imaging.

4.6 FUTURE DIRECTIONS

4.6.1 Further technical optimization

The ongoing work include further optimization of the imaging protocol, such as using longer saturation time, saturation power optimization, and adoption of unilateral coverage for improved B_1 homogeneity.

Currently, in collaboration with Philips, longer saturation time (2 s) was used for the in vivo study. The longer saturation time was achieved via application of alternating parallel transmit technology. The 2-second saturation time, together with the saturation power, is chosen to balance the total SAR and scan time. Three different saturation power, saturation

FA = 540°, 900° and 1260° were explored. As shown in Figure 4-10, the FA = 900° has the highest MTR_{asym} for all three frequencies ranges and for both the lesion and normal appearing fibroglandular tissue (NAFG), indicating the saturation FA of 900° is optimum for this imagine protocol. The three saturation FAs were chosen based on a previous simulation study (141), which suggested that the saturation FA of 180° + 360°n ($n \in \mathbb{N}$) leads to the most efficient saturation in a pulsed saturation sequence. The next step is to validate the above finding in more patients.

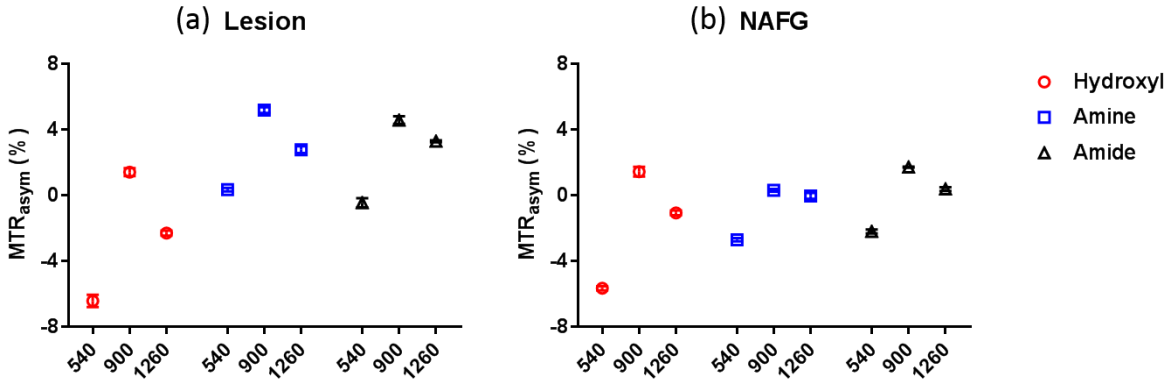

Figure 4-10 MTR_{asym} against saturation power.
Hydroxyl- (red circle), amine- (blue square) and amide- (black triangle) MTR_{asym} against saturation flip angle for lesion (a) and normal appearing fibroglandular tissue (NAFG) (b) respectively.

In the preliminary study, both breasts were covered in an axial image. However, B_1 inhomogeneities increase in bilateral setting as is shown in an example in Figure 4-11a (142). Large FOV and coil load are the possible reasons for the B_1 inhomogeneity. Because CEST effects depends on saturation power, the B_1 inhomogeneity can confound CEST data interpretation (143). To circumvent this issue, a unilateral sagittal image were acquired in the

current protocol. The unilateral B_1 maps become more homogeneous compared with bilateral B_1 map (Fig. 4-11b, c versus a). The potential downside of unilateral acquisition is increased total scan time if bilateral coverage is required.

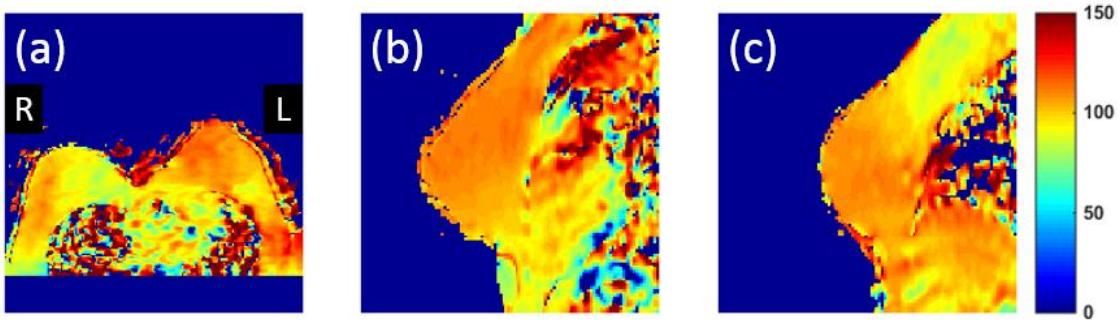

Figure 4-11 Bilateral B_1 map versus unilateral B_1 map in the same volunteer.
Axial B_1 map of bilateral breast coverage (a), sagittal B_1 map of unilateral left breast coverage (b) and sagittal B_1 map of unilateral right breast coverage (c) of the same healthy volunteer. Regions with an ideal pulse angle would have the value of 100% in a B_1 map. R: right; L: left.

4.6.2 Influence of biopsy clips on CEST

Currently, all patients were recruited prior to biopsy. This is a very challenging time for the patients, and it contributed to low participation rates. Moreover, interesting future direction to pursue is adjuvant therapy monitoring and prediction, which occurs after biopsy.

However, scans after biopsy are associated with potential complication. The clinical workflow is as follows: when the suspicious lesion is identified (typically on mammography or ultrasound), the patient is immediately referred to biopsy. When the biopsy is performed, markers are placed at the sites. The rest of the clinical treatment follows, depending on the patient needs. Any CEST-MRI performed after biopsy will have to take into account biopsy

marker influence. While MRI safe, these clips do perturb magnetic fields around them. Thus, the first step is to investigate how the breast marker clip influences the CEST effects. The study can provide suggestions on the tumor size for reliable CEST measurements in the future studies.

We have conducted a phantom investigation of the influence of three types of breast biopsy markers used in our institution: HydroMARK (Devicor Medical Produces Inc., Cincinnati, OH, hydrogel/titanium and stainless, "hydromark" in the following), UltraClip® Ultrasound Enhanced Ribbon (BARD Peripheral Vascular Inc,Tempe, AZ, BioDur^{TM} material, "ribbon") and UltraClip® Ultrasound Enhanced Coil (BARD Peripheral Vascular Inc,Tempe, AZ, titanium, "coil"). The marker clips are made of metal and different materials (often proprietary, thus of unknown exact composition), shapes and coating.

In the first set of experiments, the marker clips were injected into the whites of three boiled hen eggs. The imaging was conducted using a single-slice multi-shot TSE sequence with voxel size = 2-by-2 mm, slice thickness = 5 mm and a centric k-space ordering. The saturation consists of 40 HS pulse with FA = 900°, 50 ms in length and no inter-pulse delay. 33 points were acquired in the Z-spectrum from -6 ppm to 6 ppm. A reference imaging was acquired at -200 kHz.

As shown in Figure 4-12, already on the reference image (TSE image), the hydromark and ribbon have smaller signal enhancement or void surrounding the clips while the coil has the largest signal void.

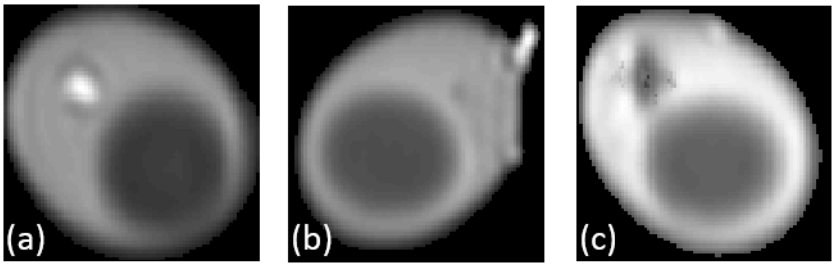

Figure 4-12 The influence of biopsy marker clip.
The CEST reference images showing the hydromark (a), ribbon (b) and coil (c) biopsy marker clips injected into the whites of the boiled hen eggs.

The above study shows that the marker clips can induce large B_0 distortions around them, thus influencing the CEST effects subsequently. However, due to very small intrinsic CEST effects of the boiled egg whites (144), the influence of the clips on the CEST still needs further investigation. Moreover, because the egg whites have different properties compared with tissues, such as T_1 and T_2, the imaging parameters used for phantoms studies are different from the ones used in human scans. Next, the experiments will be conducted in phantoms containing mixtures with large CEST effects. Finally, in vivo investigation of the marker clips on CEST will be required for the final assessment and, potentially, solution to the problem.

4.7 CONCLUSION

In the present study, the CEST-Dixon method was shown to be promising for CEST MRI in breast at 3 T. Water-fat decomposition leads to homogenous fat removal in the water-only images. The more aggressive ER- IDC malignancy displays trend to higher CEST contrast than the less aggressive ER+ IDC, benign and normal tissues. No significant

differences were observed between the ER+ IDC, benign and normal groups. Significant correlation between MTR_{asym} and Ki-67 was observed. The hydroxyl range demonstrated highest correlation with malignant alteration in breast, in agreement with previous cell, animal and human studies. While the study is preliminary the results indicate that the CEST imaging using Dixon for water-fat separation may differentiate between more aggressive and less aggressive breast cancer. A larger clinical study is needed to fully validate these observations and investigate the added value of CEST-Dixon in breast MRI imaging. Work is in progress to further optimize the imaging protocol. In addition, the influence of breast marker clips on CEST effects are under investigation to pave the way for the study of CEST-Dixon in treatment response monitoring.

CHAPTER FIVE
Dissertation Summary

The general purpose of my dissertation is to develop new CEST imaging techniques and apply these techniques in human studies at 3 T. For this purpose, I undertook two projects. In the first project, the feasibility of bSSFP for chemical exchange detection was explored. It was realized that the bSSFP in itself is sensitive to the exchange processes; hence, no additional saturation or preparation is needed for CEST-like data acquisition. As a new way for CEST data acquisition, the bSSFPX has the potential to be used for fast and quantitative CEST imaging. In the second project, a CEST-Dixon sequence for simultaneous water-only CEST imaging and B_0 mapping was developed and applied to characterize breast lesions. To evaluate the fat removal efficacy of CEST-Dixon, the influence of non-exchanging fat on CEST imaging was studied at different fat fractions and echo times. It is proved that the CEST-Dixon method can eliminate lipid contamination robustly in breast CEST imaging. In the preliminary breast cancer study, the results suggest that the CEST-Dixon method may differentiate between more aggressive and less aggressive breast cancer.

Although bSSFPX and CEST-Dixon are two promising methods, combination of bSSFPX with Dixon is challenging. The multi-echo Dixon method (145) is commonly used for water/fat separation in a bSSFP sequence. The multi-echo method acquires data at different TEs within the same TR. The acquisition of three or more echoes will increase the TR as well as the total scan time. However, increasing TR is not desired in a bSSFPX experiment because it reduces the frequency coverage of bSSFPX.

3D acquisition is desired in clinical applications because it can provide better coverage with higher resolution along the slice encoding direction. Both the bSSFPX method and the CEST-Dixon methods can be expanded to a 3D acquisition. These will be focus of further development and studies.

APPENDIX A
Influence of saturation parameters and exchange regimes on the IP and OP MTR_{asym} against fat fraction

Simulations were performed to study the influences of B_1 and saturation time (t_{sat}) on the IP and OP MTR_{asym} (normalized to the reference signal) against FF for pool systems with different exchanging pool location (Δ_{ws}) and exchange rate (k_{sw}). In the simulation, B_1 varied from 0.5 to 5 μT and t_{sat} changed from 0.5 to 7.5 s. The exchanging pools were located 1, 2, 3.5 and 5.1 ppm; each pool was simulated in slow, intermediate or fast exchange regime. Thus, the exchanging rates were 20, 100 and 1000 Hz for 1 ppm exchanging pool, 20, 250 and 2500 Hz for 2 ppm exchanging pool, 20, 450 and 4500 Hz for 3.5 ppm exchanging pool and 20, 650, 6500 Hz for 5.1 ppm exchanging pool. Other simulation parameters were the same as the ones described in the Section 3.3.1.

The above parameters did not largely alter the trend of change of the IP and OP MTR_{asym} (normalized to the reference signal) against FF, as described in the details in the Section 3.4.1 (Figs. A-1 to A-8 vs. Fig. 3-3). One exception occurred for high B_1 (Figs. A-5f,g and A-7n,o). As described in the Section 3.5, since the reference signal is non-negative, the sign of MTR_{asym} after normalization is determined by the sign of the MTR_{asym} before normalization to the reference signal. For low B_1, the MTR_{asym} before normalization was positive as the reference signal approaches 0, hence the MTR_{asym} after normalization becomes a large positive number (Figs. A-5f,g and A-7n,o low B_1). As B_1 increases, the MTR_{asym} before normalization becomes negative as the reference signal approaches 0 due to

broadening of the fat dip, hence the MTR_{asym} after normalization becomes a large negative number for this case (Figs. A-5f,g and A-7n,o high B_1).

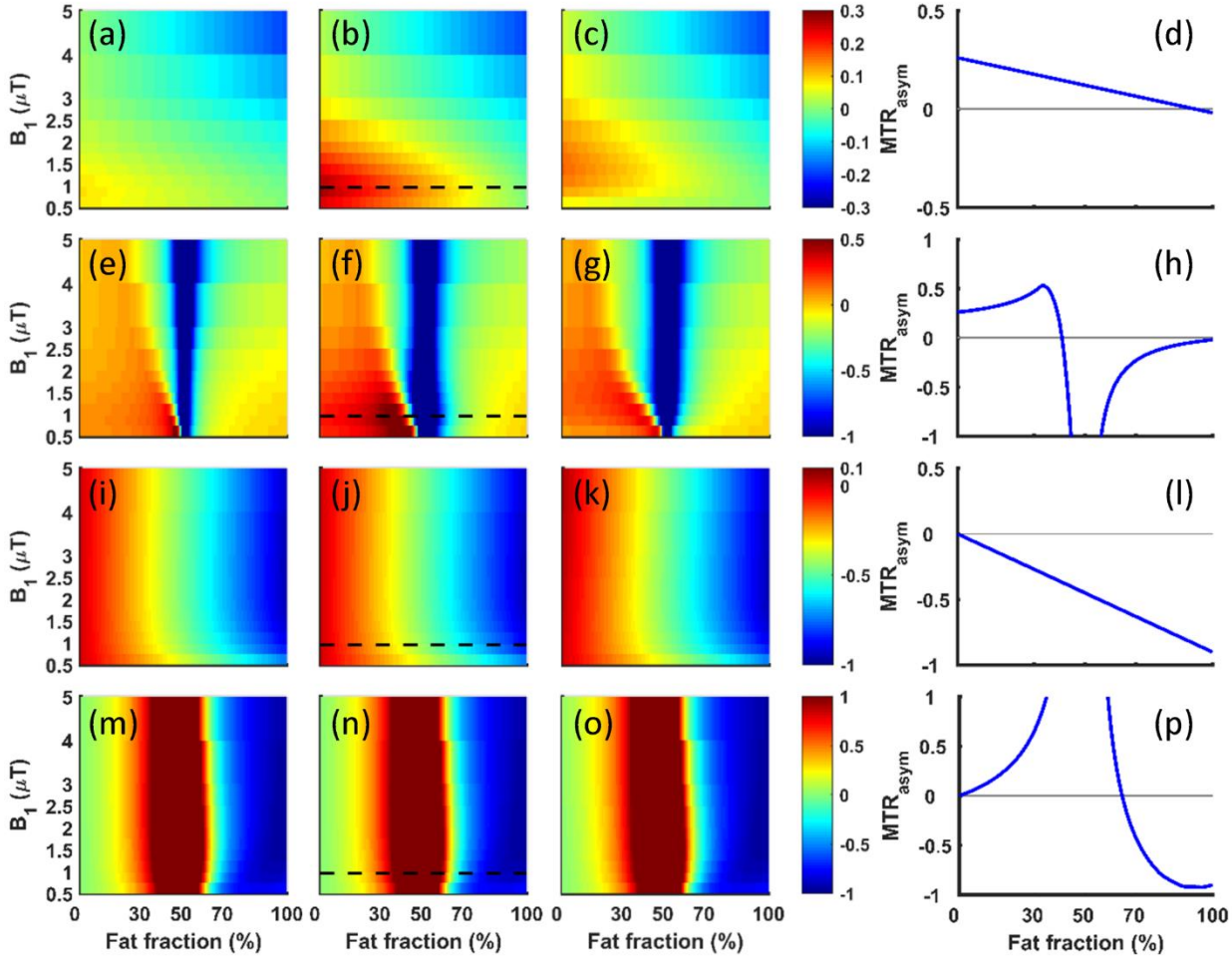

Figure A-1. The simulated MTR_{asym} for varying B_1 and FF.
The exchanging pool located 1 ppm downfield respect of water. The MTR_{asym} were averaged in two ranges: 0.8 - 1.2 ppm (a-c,e-g) and 3.3 - 3.7 ppm (i-k,m-o) for IP (a-c, i-k) and OP (e-g, m-o). The exchange rates were 20 Hz (a,e,i,m), 100 Hz (b,f,j,n), and 1000 Hz (c,g,k,o) respectively. The MTR_{asym} against FF plots at the dashed lines in (b,f,j,n) are shown in (d,h,l,p) accordingly as an example.

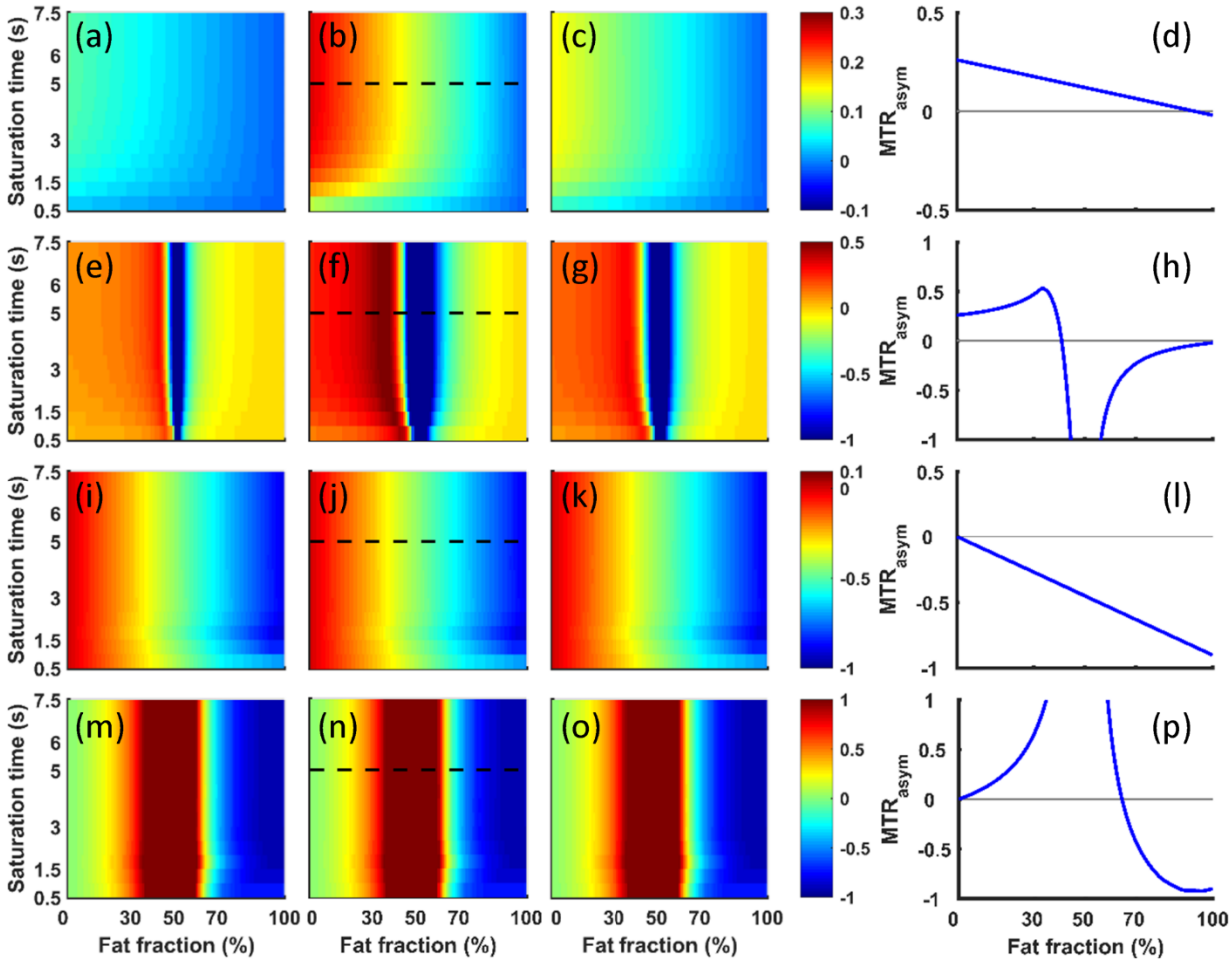

Figure A-2. The simulated MTR_{asym} for varying saturation time and FF.
The exchanging pool located 1 ppm downfield respect of water. The MTR_{asym} were averaged in two ranges: 0.8 - 1.2 ppm (a-c,e-g) and 3.3 - 3.7 ppm (i-k,m-o) for IP (a-c, i-k) and OP (e-g, m-o). The exchange rates were 20 Hz (a,e,i,m), 100 Hz (b,f,j,n), and 1000 Hz (c,g,k,o) respectively. The MTR_{asym} against FF plots at the dashed lines in (b,f,j,n) are shown in (d,h,l,p) accordingly as an example.

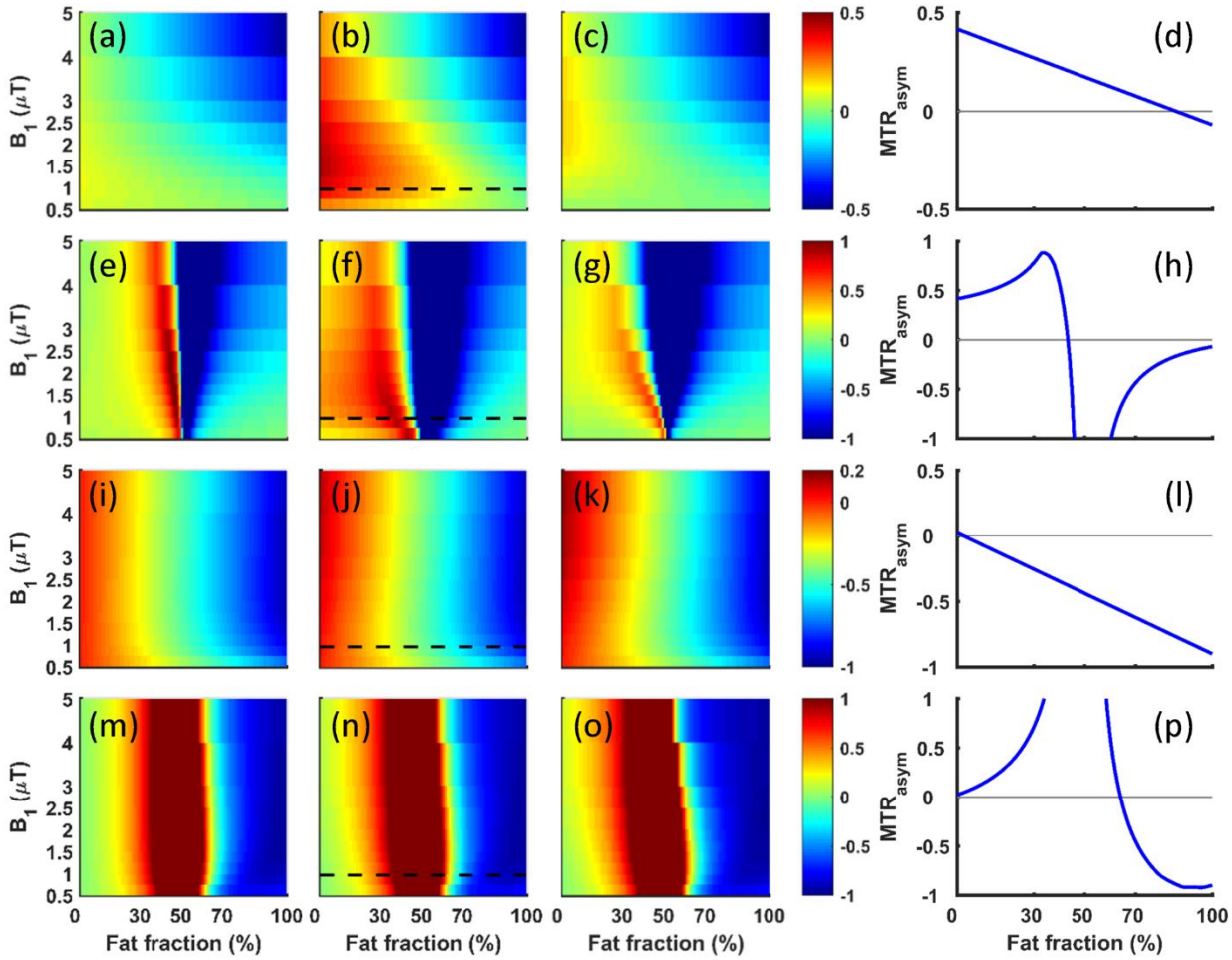

Figure A-3. The simulated MTR_{asym} for varying B_1 and FF.
The exchanging pool located 2 ppm downfield respect of water. The MTR_{asym} were averaged in two ranges: 1.8 - 2.2 ppm (a-c,e-g) and 3.3 - 3.7 ppm (i-k,m-o) for IP (a-c, i-k) and OP (e-g, m-o). The exchange rates were 20 Hz (a,e,i,m), 250 Hz (b,f,j,n), and 2500 Hz (c,g,k,o) respectively. The MTR_{asym} against FF plots at the dashed lines in (b,f,j,n) are shown in (d,h,l,p) accordingly as an example.

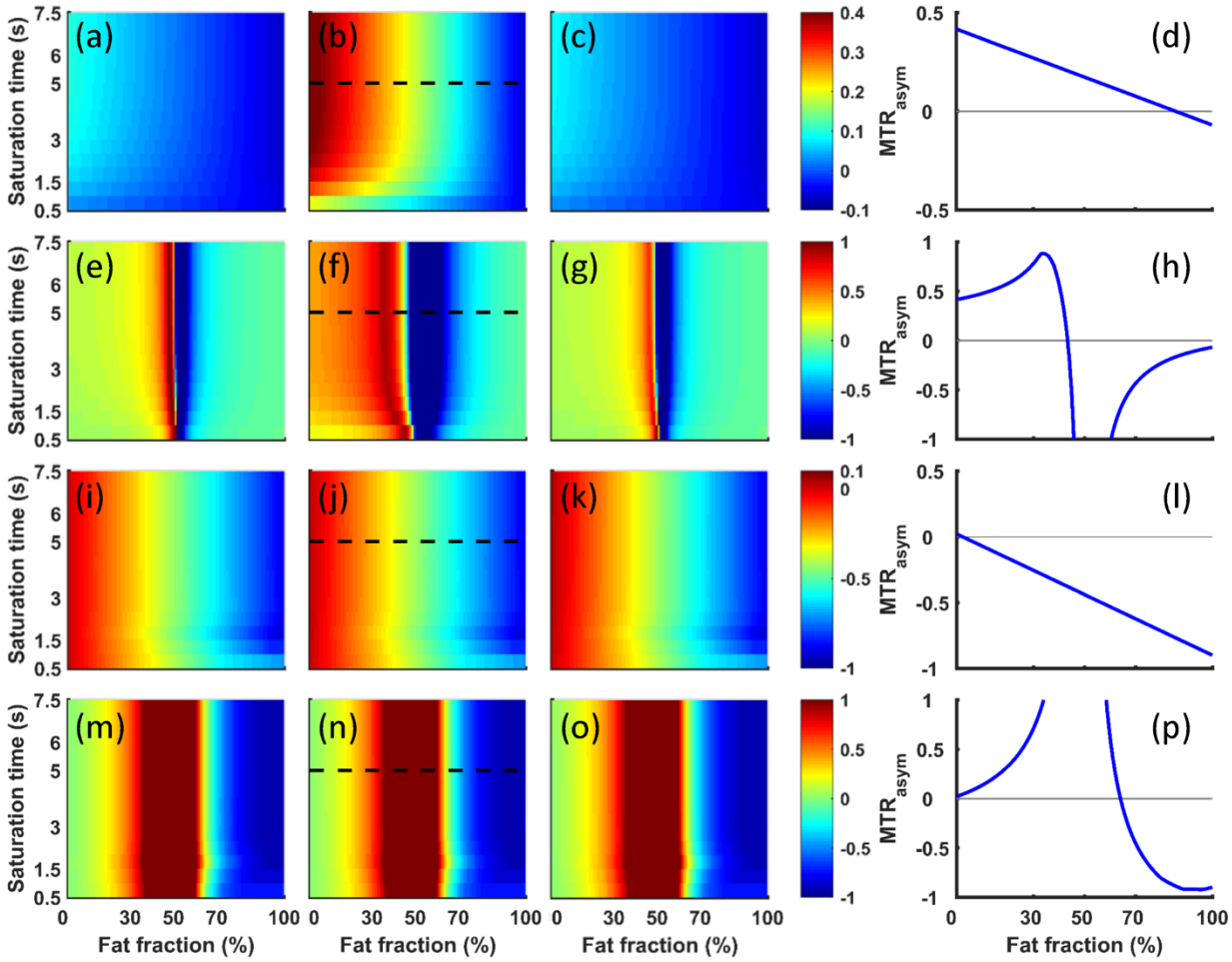

Figure A-4. The simulated MTR_{asym} for varying saturation time and FF.
The exchanging pool located 2 ppm downfield respect of water. The MTR_{asym} were averaged in two ranges: 1.8 - 2.2 ppm (a-c,e-g) and 3.3 - 3.7 ppm (i-k,m-o) for IP (a-c, i-k) and OP (e-g, m-o). The exchange rates were 20 Hz (a,e,i,m), 250 Hz (b,f,j,n), and 2500 Hz (c,g,k,o) respectively. The MTR_{asym} against FF plots at the dashed lines in (b,f,j,n) are shown in (d,h,l,p) accordingly as an example.

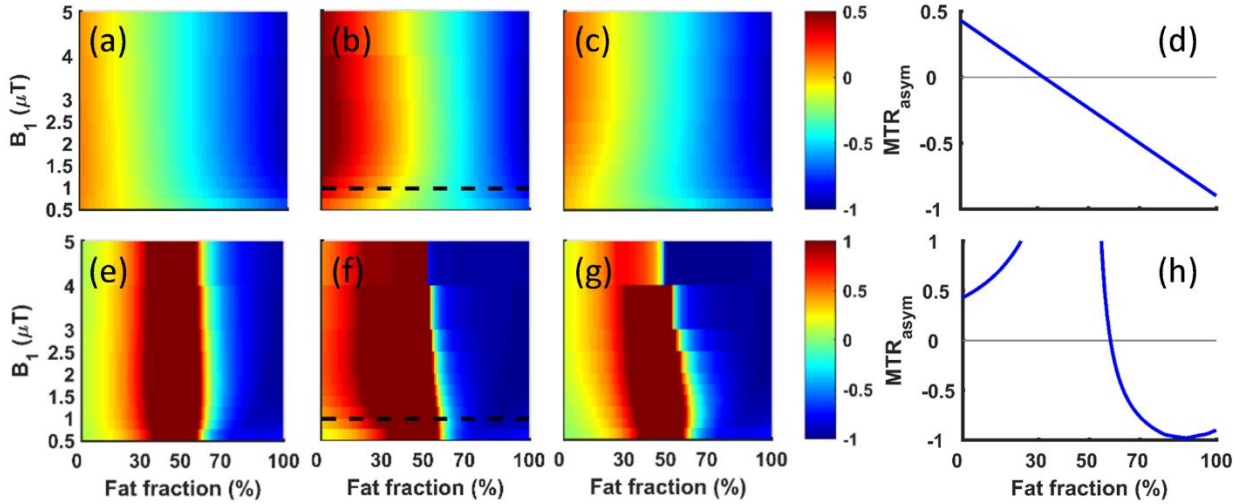

Figure A-5. The simulated MTR_{asym} for varying B_1 and FF.
The exchanging pool located 3.5 ppm downfield respect of water. The MTR_{asym} were averaged in two ranges: 3.3 - 3.7 ppm (a-c,e-g) for IP (a-c) and OP (e-g). The exchange rates were 20 Hz (a,e,i,m), 450 Hz (b,f,j,n), and 4500 Hz (c,g,k,o) respectively. The MTR_{asym} against FF plots at the dashed lines in (b,f) are shown in (d,h) accordingly as an example.

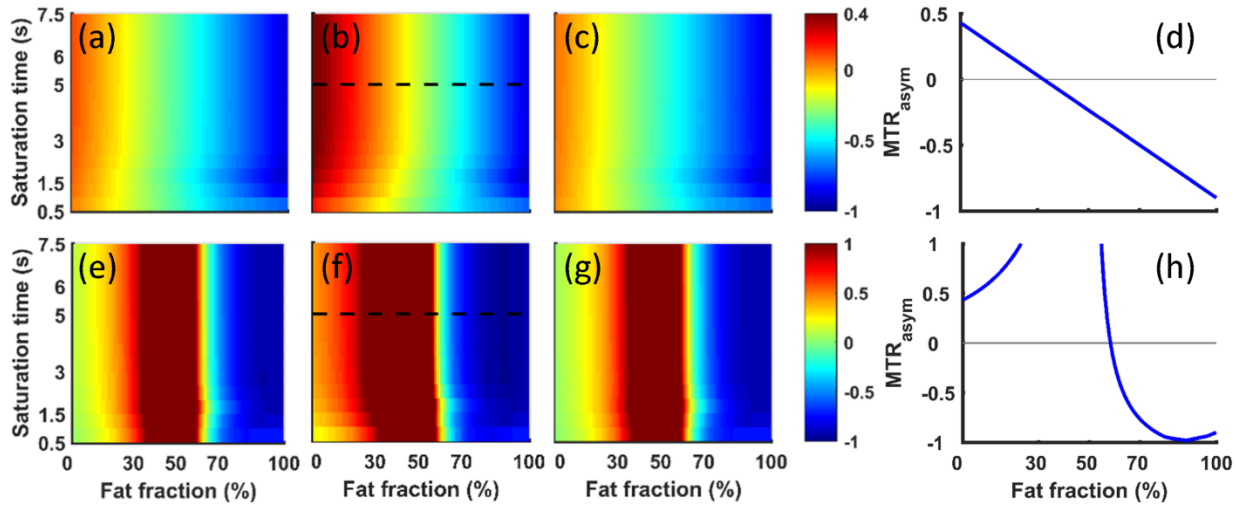

Figure A-6. The simulated MTR_{asym} for varying saturation time and FF.
The exchanging pool located 3.5 ppm downfield respect of water. The MTR_{asym} were averaged in two ranges: 3.3 - 3.7 ppm (a-c,e-g) for IP (a-c) and OP (e-g). The exchange rates were 20 Hz (a,e,i,m), 450 Hz (b,f,j,n), and 4500 Hz (c,g,k,o) respectively. The MTR_{asym} against FF plots at the dashed lines in (b,f) are shown in (d,h) accordingly as an example.

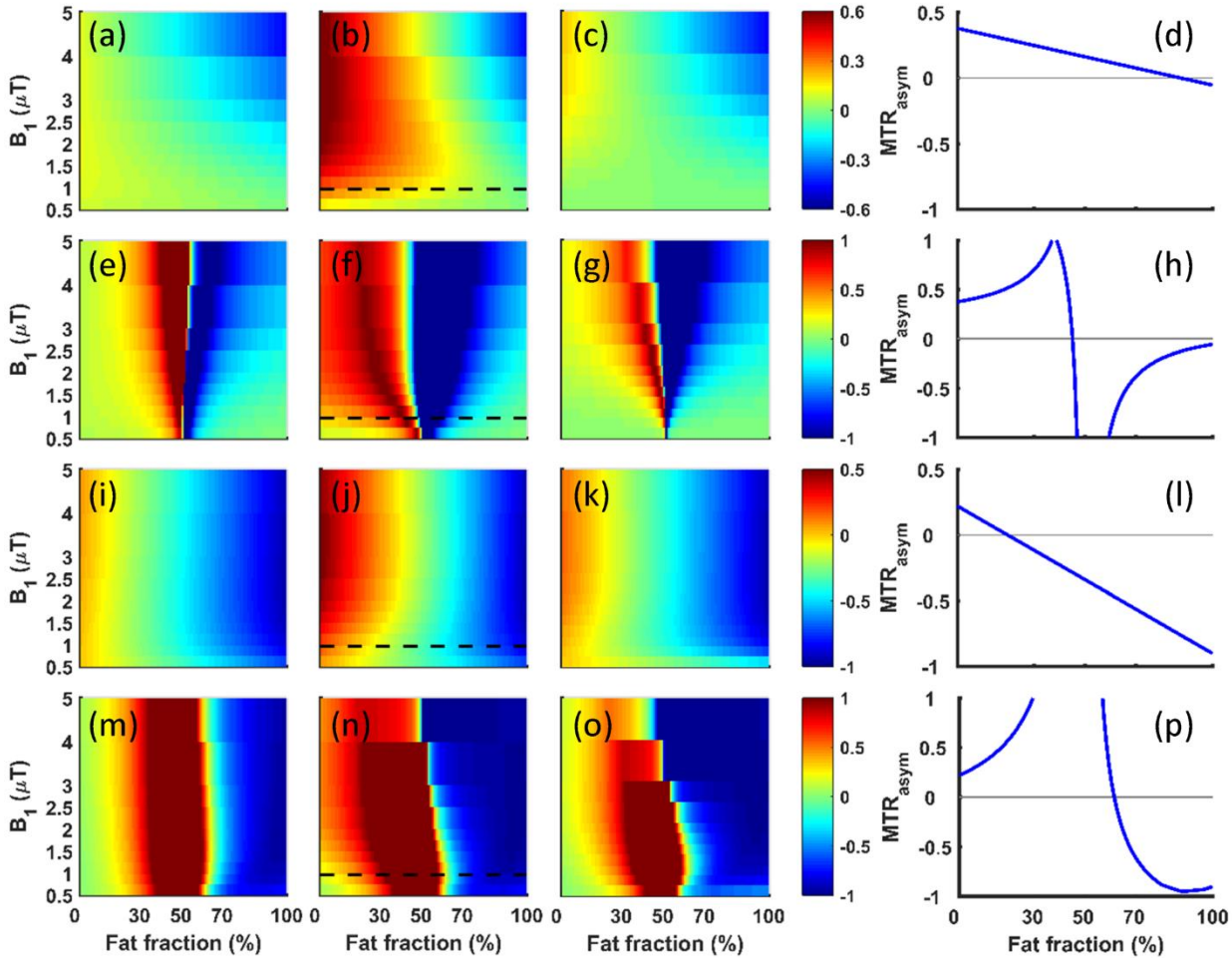

Figure A-7. The simulated MTR_{asym} for varying B_1 and FF.

The exchanging pool located 5.1 ppm downfield respect of water. The MTR_{asym} were averaged in two ranges: 4.9 - 5.3 ppm (a-c,e-g) and 3.3 - 3.7 ppm (i-k,m-o) for IP (a-c, i-k) and OP (e-g, m-o). The exchange rates were 20 Hz (a,e,i,m), 650 Hz (b,f,j,n), and 6500 Hz (c,g,k,o) respectively. The MTR_{asym} against FF plots at the dashed lines in (b,f,j,n) are shown in (d,h,l,p) accordingly as an example.

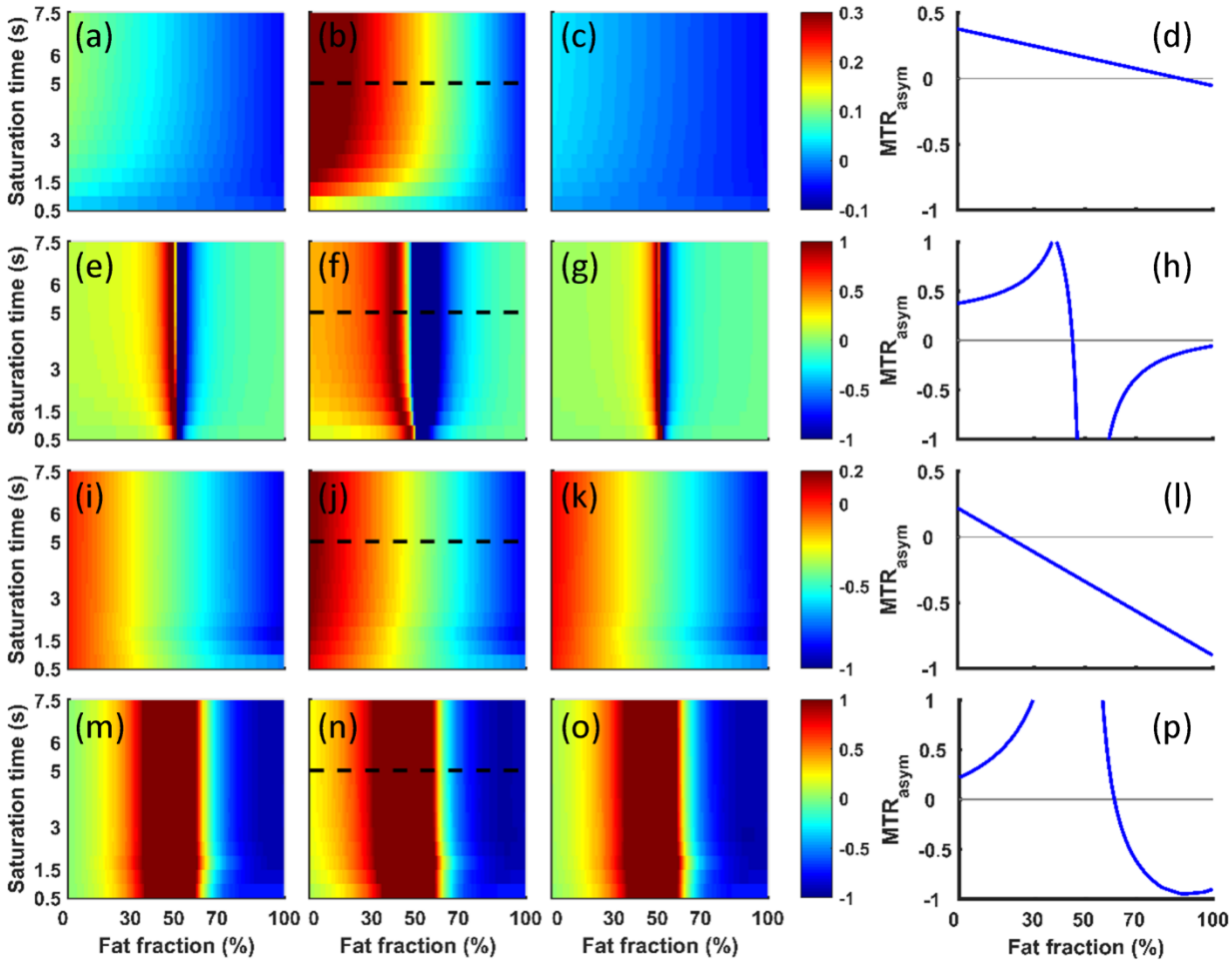

Figure A-8. The simulated MTR_{asym} for varying saturation time and FF.
The exchanging pool located 5.1 ppm downfield respect of water. The MTR_{asym} were averaged in two ranges: 4.9 - 5.3 ppm (a-c,e-g) and 3.3 - 3.7 ppm (i-k,m-o) for IP (a-c, i-k) and OP (e-g, m-o). The exchange rates were 20 Hz (a,e,i,m), 650 Hz (b,f,j,n), and 6500 Hz (c,g,k,o) respectively. The MTR_{asym} against FF plots at the dashed lines in (b,f,j,n) are shown in (d,h,l,p) accordingly as an example.

BIBLIOGRAPHY

1. Ward K, Aletras A, Balaban R. A new class of contrast agents for MRI based on proton chemical exchange dependent saturation transfer (CEST). J Magn Reson 2000;143(1):79-87.

2. Zhou J, Lal B, Wilson DA, Laterra J, van Zijl P. Amide proton transfer (APT) contrast for imaging of brain tumors. Magn Reson Med 2003;50(6):1120-1126.

3. Kogan F, Haris M, Singh A, Cai K, Debrosse C, Nanga RP, Hariharan H, Reddy R. Method for high-resolution imaging of creatine in vivo using chemical exchange saturation transfer. Magn Reson Med 2014;71(1):164-172.

4. Walker-Samuel S, Ramasawmy R, Torrealdea F, Rega M, Rajkumar V, Johnson SP, Richardson S, Gonçalves M, Parkes HG, Årstad E, Thomas DL, Pedley RB, Lythgoe MF, Golay X. In vivo imaging of glucose uptake and metabolism in tumors. Nature Medicine 2013;19(8):1067-1072.

5. Dagher AP, Aletras A, Choyke P, Balaban RS. Imaging of urea using chemical exchange-dependent saturation transfer at 1.5 T. J Magn Reson Imaging 2000;12(5):745-748.

6. Zhou J, Zijl PCMv. Chemical exchange saturation transfer imaging and spectroscopy. Progress in Nuclear Magnetic Resonance Spectroscopy 2006;48(2-3):109-136.

7. Ward K, Balaban R. Determination of pH using water protons and chemical exchange dependent saturation transfer (CEST). Magn Reson Med 2000;44(5):799-802.

8. Zhou J, Payen J-F, Wilson DA, Traystman RJ, van Zijl PC. Using the amide proton signals of intracellular proteins and peptides to detect pH effects in MRI. Nat Med 2003;9(8):1085-1090.

9. Li AX, Wojciechowski F, Suchy M, Jones CK, Hudson RHE, Menon RS, Bartha R. A sensitive PARACEST contrast agent for temperature MRI: Eu 3+-DOTAM-glycine (Gly)-phenylalanine (Phe). Magn Reson Med 2008;59(2):374-381.

10. van Zijl P, Yadav NN. Chemical exchange saturation transfer (CEST): what is in a name and what isn't? Magn Reson Med 2011;65(4):927-948.

11. Liu G, Song X, Chan KW, McMahon MT. Nuts and bolts of chemical exchange saturation transfer MRI. NMR Biomed 2013;26(7):810-828.

12. Vinogradov E, Sherry AD, Lenkinski RE. CEST: from basic principles to applications, challenges and opportunities. J Magn Reson 2013;229:155-172.

13. van Zijl PCM, Jones CK, Ren J, Malloy CR, Sherry AD. MRI detection of glycogen in vivo by using chemical exchange saturation transfer imaging (glycoCEST). Proceedings of the National Academy of Sciences 2007;104(11):4359-4364.

14. Xu X, Yadav NN, Knutsson L, Hua J, Kalyani R, Hall E, Laterra J, Blakeley J, Strowd R, Pomper M. Dynamic glucose-enhanced (DGE) MRI: translation to human scanning and first results in glioma patients. Tomography: a journal for imaging research 2015;1(2):105.

15. Lee JS, Xia D, Jerschow A, Regatte RR. In vitro study of endogenous CEST agents at 3T and 7T. Contrast Media and Molecular Imaging 2016;11(1):4-14.

16. Zhang S, Merritt M, Woessner DE, Lenkinski RE, Sherry AD. PARACEST Agents: Modulating MRI Contrast via Water Proton Exchange. Acc Chem Res 2003;36(10):783-790.

17. Silvio A, Daniela DC, Enzo T. Highly Sensitive MRI Chemical Exchange Saturation Transfer Agents Using Liposomes. Angewandte Chemie International Edition 2005;44(34):5513-5515.

18. Schröder L, Lowery TJ, Hilty C, Wemmer DE, Pines A. Molecular imaging using a targeted magnetic resonance hyperpolarized biosensor. Science 2006;314(5798):446-449.

19. Xiang X, W.Y. CK, Linda K, Dmitri A, Jiadi X, Guanshu L, Yoshinori K, Bachchu L, John L, T. MM, C.M. vZP. Dynamic glucose enhanced (DGE) MRI for combined imaging of blood–brain barrier break down and increased blood volume in brain cancer. Magn Reson Med 2015;74(6):1556-1563.

20. Hua J, Jones CK, Blakeley J, Smith SA, van Zijl P, Zhou J. Quantitative description of the asymmetry in magnetization transfer effects around the water resonance in the human brain. Magn Reson Med 2007;58(4):786-793.

21. Ng M-C, Hua J, Hu Y, Luk KD, Lam EY. Magnetization transfer (MT) asymmetry around the water resonance in human cervical spinal cord. J Magn Reson Imaging 2009;29(3):523-528.

22. Ling W, Regatte RR, Navon G, Jerschow A. Assessment of glycosaminoglycan concentration in vivo by chemical exchange-dependent saturation transfer (gagCEST). Proceedings of the National Academy of Sciences 2008;105(7):2266-2270.

23. Jones CK, Polders D, Hua J, Zhu H, Hoogduin HJ, Zhou J, Luijten P, van Zijl P. In vivo three-dimensional whole-brain pulsed steady-state chemical exchange saturation transfer at 7 T. Magn Reson Med 2012;67(6):1579-1589.

24. Jones CK, Huang A, Xu J, Edden RA, Schär M, Hua J, Oskolkov N, Zacà D, Zhou J, McMahon MT. Nuclear Overhauser enhancement (NOE) imaging in the human brain at 7T. Neuroimage 2013;77:114-124.

25. Woessner DE, Zhang S, Merritt ME, Sherry AD. Numerical solution of the Bloch equations provides insights into the optimum design of PARACEST agents for MRI. Magn Reson Med 2005;53(4):790-799.

26. Zhou J, Wilson DA, Sun PZ, Klaus JA, van Zijl P. Quantitative description of proton exchange processes between water and endogenous and exogenous agents for WEX, CEST, and APT experiments. Magn Reson Med 2004;51(5):945-952.

27. Zaiss M, Schmitt B, Bachert P. Quantitative separation of CEST effect from magnetization transfer and spillover effects by Lorentzian-line-fit analysis of z-spectra. J Magn Reson 2011;211(2):149-155.

28. Zaiss M, Bachert P. Exchange-dependent relaxation in the rotating frame for slow and intermediate exchange – modeling off-resonant spin-lock and chemical exchange saturation transfer. NMR Biomed 2013;26(5):507-518.

29. Jin T, Autio J, Obata T, Kim SG. Spin-locking versus chemical exchange saturation transfer MRI for investigating chemical exchange process between water and labile metabolite protons. Magn Reson Med 2011;65(5):1448-1460.

30. Zaiss M, Bachert P. Chemical exchange saturation transfer (CEST) and MR Z-spectroscopy in vivo: a review of theoretical approaches and methods. Phys Med Biol 2013;58(22):R221.

31. Trott O, Palmer III AG. R1ρ Relaxation outside of the Fast-Exchange Limit. J Magn Reson 2002;154(1):157-160.

32. Zaiss M, Bachert P. Exchange-dependent relaxation in the rotating frame for slow and intermediate exchange–modeling off-resonant spin-lock and chemical exchange saturation transfer. NMR Biomed 2013;26(5):507-518.

33. Yuan J, Zhou J, Ahuja AT, Wang Y-XJ. MR chemical exchange imaging with spin-lock technique (CESL): a theoretical analysis of the Z-spectrum using a two-pool R1ρ relaxation model beyond the fast-exchange limit. Phys Med Biol 2012;57(24):8185.

34. Morrison C, Henkelman RM. A model for magnetization transfer in tissues. Magn Reson Med 1995;33(4):475-482.

35. Henkelman RM, Huang X, Xiang QS, Stanisz G, Swanson SD, Bronskill MJ. Quantitative interpretation of magnetization transfer. Magn Reson Med 1993;29(6):759-766.

36. Desmond KL, Stanisz GJ. Understanding quantitative pulsed CEST in the presence of MT. Magn Reson Med 2012;67(4):979-990.

37. Li AX, Hudson RH, Barrett JW, Jones CK, Pasternak SH, Bartha R. Four-pool modeling of proton exchange processes in biological systems in the presence of MRI–paramagnetic chemical exchange saturation transfer (PARACEST) agents. Magn Reson Med 2008;60(5):1197-1206.

38. Scheidegger R, Vinogradov E, Alsop DC. Amide proton transfer imaging with improved robustness to magnetic field inhomogeneity and magnetization transfer asymmetry using saturation with frequency alternating RF irradiation. Magn Reson Med 2011;66(5):1275-1285.

39. Friedman JI, McMahon MT, Stivers JT, Van Zijl PC. Indirect detection of labile solute proton spectra via the water signal using frequency-labeled exchange (FLEX) transfer. J Am Chem Soc 2010;132(6):1813-1815.

40. Yadav NN, Jones CK, Xu J, Bar-Shir A, Gilad AA, McMahon MT, van Zijl PCM. Detection of rapidly exchanging compounds using on-resonance frequency-labeled exchange (FLEX) transfer. Magn Reson Med 2012;68(4):1048-1055.

41. Kim M, Gillen J, Landman BA, Zhou J, van Zijl P. Water saturation shift referencing (WASSR) for chemical exchange saturation transfer (CEST) experiments. Magn Reson Med 2009;61(6):1441-1450.

42. Zaiss M, Xu J, Goerke S, Khan IS, Singer RJ, Gore JC, Gochberg DF, Bachert P. Inverse Z-spectrum analysis for spillover-, MT-, and T1-corrected steady-state pulsed CEST-MRI - application to pH-weighted MRI of acute stroke. NMR Biomed 2014;27(3):240-252.

43. Cai K, Singh A, Poptani H, Li W, Yang S, Lu Y, Hariharan H, Zhou XJ, Reddy R. CEST signal at 2ppm (CEST@2ppm) from Z-spectral fitting correlates with creatine distribution in brain tumor. NMR Biomed 2015;28(1):1-8.

44. Evbuomwan OM, Lee J, Woods M, Sherry AD. The Presence of Fast-Exchanging Proton Species in Aqueous Solutions of paraCEST Agents Can Impact Rate Constants Measured for Slower Exchanging Species When Fitting CEST Spectra to the Bloch Equations. lnorg Chem 2014;53(19):10012-10014.

45. Randtke EA, Chen LQ, Pagel MD. The reciprocal linear QUEST analysis method facilitates the measurements of chemical exchange rates with CEST MRI. Contrast Media Mol Imaging 2014;9(3):252-258.

46. Randtke EA, Chen LQ, Corrales LR, Pagel MD. The Hanes-Woolf linear QUESP method improves the measurements of fast chemical exchange rates with CEST MRI. Magn Reson Med 2014;71(4):1603-1612.

47. Jones CK, Schlosser MJ, van Zijl P, Pomper MG, Golay X, Zhou J. Amide proton transfer imaging of human brain tumors at 3T. Magn Reson Med 2006;56(3):585-592.

48. Zhou J, Blakeley JO, Hua J, Kim M, Laterra J, Pomper MG, van Zijl P. Practical data acquisition method for human brain tumor amide proton transfer (APT) imaging. Magn Reson Med 2008;60(4):842-849.

49. Zhou J, Tryggestad E, Wen Z, Lal B, Zhou T, Grossman R, Wang S, Yan K, Fu D-X, Ford E. Differentiation between glioma and radiation necrosis using molecular magnetic resonance imaging of endogenous proteins and peptides. Nat Med 2011;17(1):130-134.

50. Dula AN, Arlinghaus LR, Dortch RD, Dewey BE, Whisenant JG, Ayers GD, Yankeelov TE, Smith SA. Amide proton transfer imaging of the breast at 3 T: establishing reproducibility and possible feasibility assessing chemotherapy response. Magn Reson Med 2013;70(1):216-224.

51. Jia G, Abaza R, Williams JD, Zynger DL, Zhou J, Shah ZK, Patel M, Sammet S, Wei L, Bahnson RR. Amide proton transfer MR imaging of prostate cancer: a preliminary study. J Magn Reson Imaging 2011;33(3):647-654.

52. Cai K, Haris M, Singh A, Kogan F, Greenberg JH, Hariharan H, Detre JA, Reddy R. Magnetic resonance imaging of glutamate. Nat Med 2012;18(2):302-306.

53. Cai K, Singh A, Roalf DR, Nanga RPR, Haris M, Hariharan H, Gur R, Reddy R. Mapping glutamate in subcortical brain structures using high-resolution GluCEST MRI. NMR Biomed 2013;26(10):1278-1284.

54. Haris M, Nath K, Cai K, Singh A, Crescenzi R, Kogan F, Verma G, Reddy S, Hariharan H, Melhem ER, Reddy R. Imaging of glutamate neurotransmitter alterations in Alzheimer's disease. NMR Biomed 2013;26(4):386-391.

55. Kim M, Chan Q, Anthony MP, Cheung K, Samartzis D, Khong PL. Assessment of glycosaminoglycan distribution in human lumbar intervertebral discs using chemical exchange saturation transfer at 3 T: feasibility and initial experience. NMR Biomed 2011;24(9):1137-1144.

56. Haris M, Singh A, Cai K, Kogan F, McGarvey J, DeBrosse C, Zsido GA, Witschey WRT, Koomalsingh K, Pilla JJ, Chirinos JA, Ferrari VA, Gorman JH, Hariharan H, Gorman RC, Reddy R. A technique for in vivo mapping of myocardial creatine kinase metabolism. Nat Med 2014;20(2):209-214.

57. Feliks K, Mohammad H, Catherine D, Anup S, P. NR, Kejia C, Hari H, Ravinder R. In vivo chemical exchange saturation transfer imaging of creatine (CrCEST) in skeletal muscle at 3T. J Magn Reson Imaging 2014;40(3):596-602.

58. Haris M, Cai K, Singh A, Hariharan H, Reddy R. In vivo mapping of brain myo-inositol. Neuroimage 2011;54(3):2079-2085.

59. Sun PZ, Cheung JS, Wang E, Lo EH. Association between pH-Weighted Endogenous Amide Proton Chemical Exchange Saturation Transfer MRI and Tissue Lactic Acidosis during Acute Ischemic Stroke. J Cereb Blood Flow Metab 2011;31(8):1743-1750.

60. Gregory RB, Crabo L, Percy AJ, Rosenberg A. Water catalysis of peptide hydrogen isotope exchange. Biochemistry 1983;22(4):910-917.

61. McMahon MT, Gilad AA, Zhou J, Sun PZ, Bulte JW, van Zijl P. Quantifying exchange rates in chemical exchange saturation transfer agents using the saturation time and saturation power dependencies of the magnetization transfer effect on the magnetic resonance imaging signal (QUEST and QUESP): Ph calibration for poly-L-lysine and a starburst dendrimer. Magn Reson Med 2006;55(4):836-847.

62. Dixon WT, Ren J, Lubag AJ, Ratnakar J, Vinogradov E, Hancu I, Lenkinski RE, Sherry AD. A concentration-independent method to measure exchange rates in PARACEST agents. Magn Reson Med 2010;63(3):625-632.

63. Ostroff ED, Waugh JS. Multiple Spin Echoes and Spin Locking in Solids. Phys Rev Lett 1966;16(24):1097-1098.

64. Mehring M. Principles of High Resolution NMR in Solids. Diehl P, Fluck E, Kosfeld R, editors. Heidelberg: Springer-Verlag; 1983.

65. Rhim W-K, Burum DP, Elleman DD. Multiple-Pulse Spin Locking in Dipolar Solids. Phys Rev Lett 1976;37(26):1764-1766.

66. Maricq MM. Application of average Hamiltonian theory to the NMR of solids. Phys Rev B: Condens Matter 1982;25(11):6622-6632.

67. Carr HY. Steady-State Free Precession in Nuclear Magnetic Resonance. Phys Rev 1958;112(5):1693-1701.

68. Freeman R, Hill HDW. Phase and Intentsity Anomalies in Fourier Transform NMR. J Magn Reson 1971;4:366-383.

69. Haacke EM, Brown RW, Thompson MR, Venkatesan R. Magnetic Resonance Imaging - Physical Principles and Sequence Design. New York: A John Wiley and Sons, Inc; 1999.

70. Ganter C. Analytical solution to the transient phase of steady-state free precession sequences. Magn Reson Med 2009;62(1):149-164.

71. Scheffler K, Hennig J. Is TrueFISP a gradient-echo or a spin-echo sequence? Magn Reson Med 2003;49(2):395-397.

72. Scheffler K, Hennig J. T1 quantification with inversion recovery TrueFISP. Magn Reson Med 2001;45(4):720-723.

73. Bernstein MA, King KF, Zhou XJ. Handbook of MRI pulse sequences: Elsevier; 2004.

74. Deoni SC, Rutt BK, Jones DK. Investigating exchange and multicomponent relaxation in fully-balanced steady-state free precession imaging. J Magn Reson Imaging 2008;27(6):1421-1429.

75. Deoni SC, Rutt BK, Peters TM. Rapid combined T1 and T2 mapping using gradient recalled acquisition in the steady state. Magn Reson Med 2003;49(3):515-526.

76. Zur Y, Stokar S, Bendel P. An analysis of fast imaging sequences with steady-state transverse magnetization refocusing. Magn Reson Med 1988;6(2):175-193.

77. Bieri O, Scheffler K. Fundamentals of balanced steady state free precession MRI. J Magn Reson Imaging 2013;38(1):2-11.

78. Hargreaves BA, Vasanawala SS, Pauly JM, Nishimura DG. Characterization and reduction of the transient response in steady-state MR imaging. Magn Reson Med 2001;46(1):149-158.

79. Schmitt P, Griswold MA, Gulani V, Haase A, Flentje M, Jakob PM. A simple geometrical description of the TrueFISP ideal transient and steady-state signal. Magn Reson Med 2006;55:177-186.

80. Scheffler K, Lehnhardt S. Principles and applications of balanced SSFP techniques. Eur Radiol 2003;13:2409-2418.

81. Oppelt A, Graumann R, Barfuss H, Fischer H, Hartl W, Schajor W. FISP: a new fast MRI sequence Electromedica (Engl Ed) 1986;54:15-18.

82. Miller KL. Asymmetries of the balanced SSFP profile. Part I: Theory and observation. Magn Reson Med 2010;63(2):385-395.

83. Bieri O, Scheffler K. Optimized balanced steady-state free precession magnetization transfer Imaging. Magn Reson Med 2007;58(3):511-518.

84. Hinshaw WS. Image formation by nuclear magnetic resonance: The sensitive-point method. J Appl Phys 1976;47(8):3709-3721.

85. Zur Y, Stokar S, Bendel P. An analysis of fast imaging sequences with steady-state transverse magnetization refocusing. Magn Reson Med 1988;6(2):175-193.

86. Ernst RR, Bodenhausen G, Wokaun A. Principles of Nuclear Magnetic Resonance in One and Two Dimensions. In: Rowlinson JS, editor. The International Series of Monographs in Chemistry. Oxford: Clarendon Press; 1994.

87. Abragam A. The principles of nuclear magnetism. Marshall W, Wilkinson D, editors: Oxford: Clarendon Press; 1961.

88. Ganter C. Analytical solution to the transient phase of steady-state free precession sequences. Magn Reson Med 2009;62(1):149-164.

89. Moritz Z, Peter B. Chemical exchange saturation transfer (CEST) and MR Z - spectroscopy in vivo : a review of theoretical approaches and methods. Phys Med Biol 2013;58(22):R221.

90. Michaeli S, Sorce DJ, Idiyatullin D, Ugurbil K, Garwood M. Transverse relaxation in the rotating frame induced by chemical exchange. J Magn Reson 2004;169(2):293-299.

91. Keupp J, Baltes C, Harvey P, Van den Brink J. Parallel RF transmission based MRI technique for highly sensitive detection of amide proton transfer in the human brain. In Proceedings of the 19th Annual Meeting of ISMRM, Montreal, Quebec, Canada 2011:p 710.

92. Foerster BU, Tomasi D, Caparelli EC. Magnetic field shift due to mechanical vibration in functional magnetic resonance imaging. Magn Reson Med 2005;54(5):1261-1267.

93. Narvainen J, Hubbard PL, Kauppinen RA, Morris GA. Z-Spectroscopy with Alternating-Phase Irradiation. J Magn Reson 2010;207:242-250.

94. Scheidegger R, Vinogradov E, Alsop D. Amide proton transfer imaging with improved robustness to magnetic field inhomogeneity and magnetization transfer

assymetry using Saturation with Frequency ALternating RF Irradiation (SAFARI). Magn Reson Med 2011;66:1275-1285.

95. Lee J-S, Regatte RR, Jerschow A. Separating Chemical Exchange Saturation Transfer Contrast from Magnetization Transfer Asymmetry under Two-Frequency RF Irradiation J Magn Reson 2012;215:56-63.

96. Hargreaves B. Rapid Gradient-Echo Imaging. Journal of magnetic resonance imaging : JMRI 2012;36(6):1300-1313.

97. Zhang S, Liu Z, Grant A, Keupp J, Lenkinski RE, Vinogradov E. Balanced Steady-State Free Precession (bSSFP) from an effective field perspective: Application to the detection of chemical exchange (bSSFPX). J Magn Reson 2017;275:55-67.

98. Zaiss M, Schmitt B, Bachert P. Quantitative separation of CEST effect from magnetization transfer and spillover effects by Lorentzian-line-fit analysis of z-spectra. J Magn Reson 2011;211(2):149-155.

99. Woessner DE, Zhang S, Merrit M, Sherry AD. A numerical solution of the Bloch equations provides insights into the optimal design of PARACEST agents. Magn Reson Med 2005;53:790-799.

100. Chan KW, Jiang L, Cheng M, Wijnen JP, Liu G, Huang P, Zijl P, McMahon MT, Glunde K. CEST-MRI detects metabolite levels altered by breast cancer cell aggressiveness and chemotherapy response. NMR Biomed 2016;29(6):806-816.

101. van Zijl PCM, Jones CK, Ren J, Malloy CR, Sherry AD. MRI Detection of Glycogen *In Vivo* by Using Chemical Exchange Saturation Transfer Imgaing (glycoCEST). Proc Nat Acad Sci USA 2007;104:4359-4364.

102. Wijnen JP, Chan KWY, Van Zijl PCM, McMahon MT, Glunde K. Chemical Exchange Saturation Transfer (CEST)-MRI detects free choline in breast cancer cells. Proc Intl Soc Mag Reson Med 2012:1544.

103. Schmitt B, Trattnig S, Schlemmer H-P. CEST-imaging: A new contrast in MR-mammography by means of chemical exchange saturation transfer. Eur J Radiol 2012;81:S144-S146.

104. Zu Z, Li K, Janve VA, Does MD, Gochberg DF. Optimizing pulsed-chemical exchange saturation transfer imaging sequences. Magn Reson Med 2011;66(4):1100-1108.

105. Ganter C. Off-resonance effects in the transient response of SSFP sequences. Magn Reson Med 2004;52(2):368-375.

106. Miller KL, Smith SM, Jezzard P. Asymmetries of the balanced SSFP profile. Part II: White matter. Magn Reson Med 2010;63(2):396-406.

107. Sagiyama K, Mashimo T, Togao O, Vemireddy V, Hatanpaa KJ, Maher EA, Mickey BE, Pan E, Sherry AD, Bachoo RM, Takahashi M. In vivo chemical exchange saturation transfer imaging allows early detection of a therapeutic response in glioblastoma. Proc Natl Acad Sci USA 2014;111(12):4542-4547.

108. Schmitt B, Zamecnik P, Zaiss M, Rerich E, Schuster L, Bachert P, Schlemmer HP. A New Contrast in MR Mammography by Means of Chemical Exchange Saturation Transfer (CEST) Imaging at 3 Tesla: Preliminary Results. Fortschr Röntgenstr 2011;183(11):1030-1036.

109. Klomp DW, Dula AN, Arlinghaus LR, Italiaander M, Dortch RD, Zu Z, Williams JM, Gochberg DF, Luijten PR, Gore JC. Amide proton transfer imaging of the human breast at 7T: development and reproducibility. NMR Biomed 2013;26(10):1271-1277.

110. Dula AN, Dewey BE, Arlinghaus LR, Williams JM, Klomp D, Yankeelov TE, Smith S. Optimization of 7-T chemical exchange saturation transfer parameters for validation of glycosaminoglycan and amide proton transfer of fibroglandular breast tissue. Radiology 2014;275(1):255-261.

111. Longo DL, Dastrù W, Digilio G, Keupp J, Langereis S, Lanzardo S, Prestigio S, Steinbach O, Terreno E, Uggeri F. Iopamidol as a responsive MRI-chemical exchange saturation transfer contrast agent for pH mapping of kidneys: In vivo studies in mice at 7 T. Magn Reson Med 2011;65(1):202-211.

112. Yu H, Shimakawa A, McKenzie CA, Brodsky E, Brittain JH, Reeder SB. Multiecho water-fat separation and simultaneous R2* estimation with multifrequency fat spectrum modeling. Magn Reson Med 2008;60(5):1122-1134.

113. Lu J, Zhou J, Cai C, Cai S, Chen Z. Observation of true and pseudo NOE signals using CEST-MRI and CEST-MRS sequences with and without lipid suppression. Magn Reson Med 2015;73(4):1615-1622.

114. Sun PZ, Zhou J, Sun W, Huang J, van Zijl P. Suppression of lipid artifacts in amide proton transfer imaging. Magn Reson Med 2005;54(1):222-225.

115. Zhu H, Jones CK, van Zijl PCM, Barker PB, Zhou JY. Fast 3D Chemical Exchange Saturation Transfer (CEST) Imaging of the Human Brain. Magn Reson Med 2010;64(3):638-644.

116. Song X, Airan RD, Arifin DR, Bar-Shir A, Kadayakkara DK, Liu G, Gilad AA, van Zijl PCM, McMahon MT, Bulte JWM. Label-free in vivo molecular imaging

of underglycosylated mucin-1 expression in tumour cells. Nature Communications 2015;6:6719.

117. Zhang S, Seiler S, Wang X, Madhuranthakam AJ, Keupp J, Knippa EE, Lenkinski RE, Vinogradov E. CEST-Dixon for human breast lesion characterization at 3 T: A preliminary study. Magn Reson Med 2018:n/a-n/a.

118. Zu Z, Li K, Janve VA, Does MD, Gochberg DF. Optimizing pulsed-chemical exchange saturation transfer imaging sequences. Magn Reson Med 2011;66(4):1100-1108.

119. Hussain HK, Chenevert TL, Londy FJ, Gulani V, Swanson SD, McKenna BJ, Appelman HD, Adusumilli S, Greenson JK, Conjeevaram HS. Hepatic Fat Fraction: MR Imaging for Quantitative Measurement and Display—Early Experience 1. Radiology 2005;237(3):1048-1055.

120. Soesbe TC, Merritt ME, Green KN, Rojas-Quijano FA, Sherry AD. T2 exchange agents: a new class of paramagnetic MRI contrast agent that shortens water T2 by chemical exchange rather than relaxation. Magn Reson Med 2011;66(6):1697-1703.

121. Soriano Jr NU, Venditti R, Argyropoulos DS. Biodiesel synthesis via homogeneous Lewis acid-catalyzed transesterification. Fuel 2009;88(3):560-565.

122. Zhang S, Keupp J, Wang X, Dimitrov I, Madhuranthakam AJ, Lenkinski RE, Vinogradov E. Z-spectrum appearance and interpretation in the presence of fat: Influence of acquisition parameters. Magn Reson Med 2017:doi: 10.1002/mrm.26900.

123. Jia G, Wei W, Yang X, Flanigan DC, Keupp J, Zhou J, Knopp MV. Improving mobile protein level detection using mDIXON-based APT-MRI in bone marrow edema. In Proceedings of the 20th Annual Meeting of ISMRM, Melbourne Australia 2012:p 3373.

124. Berg WA, Zhang Z, Lehrer D, et al. Detection of breast cancer with addition of annual screening ultrasound or a single screening mri to mammography in women with elevated breast cancer risk. JAMA 2012;307(13):1394-1404.

125. Kuhl CK. MRI of breast tumors. Eur Radiol 2000;10(1):46-58.

126. Saslow D, Boetes C, Burke W, Harms S, Leach MO, Lehman CD, Morris E, Pisano E, Schnall M, Sener S. American Cancer Society guidelines for breast screening with MRI as an adjunct to mammography. CA Cancer J Clin 2007;57(2):75-89.

127. Guo Y, Cai YQ, Cai ZL, Gao YG, An NY, Ma L, Mahankali S, Gao JH. Differentiation of clinically benign and malignant breast lesions using diffusion-weighted imaging. J Magn Reson Imaging 2002;16(2):172-178.

128. Weinstein S, Rosen M. Breast MR imaging: current indications and advanced imaging techniques. Radiol Clin North Am 2010;48(5):1013-1042.

129. Xiaodong Z, D. NM, A.R. KS, M. DB, Berthold K, R. BM. Liver fat quantification using a multi-step adaptive fitting approach with multi-echo GRE imaging. Magn Reson Med 2014;72(5):1353-1365.

130. Keupp J, Eggers H. CEST-dixon MRI for sensitive and accurate measurement of amide proton transfer in humans at 3T. In Proceedings of the Joint Annual Meeting ISMRM-ESMRMB 2010, Stockholm, Sweden 2010;18:p 338.

131. Weigel MT, Dowsett M. Current and emerging biomarkers in breast cancer: prognosis and prediction. Endocr Relat Cancer 2010;17(4):R245-R262.

132. Sheikh MS, Garcia M, Pujol P, Fontana JA, Rochefort H. Why are estrogen-receptor-negative breast cancers more aggressive than the estrogen-receptor-positive breast cancers? Invasion Metastasis 1994;14(1-6):329-336.

133. Sun PZ, Longo DL, Hu W, Xiao G, Wu R. Quantification of iopamidol multi-site chemical exchange properties for ratiometric chemical exchange saturation transfer (CEST) imaging of pH. Phys Med Biol 2014;59(16):4493.

134. Least-Squares Fitting. http://wwwmathworkscom/help/curvefit/least-squares-fittinghtml Accessed September 13, 2017.

135. Haroon S, Hashmi AA, Khurshid A, Kanpurwala MA, Mujtuba S, Malik B, Faridi N. Ki67 index in breast cancer: correlation with other prognostic markers and potential in pakistani patients. Asian Pac J Cancer Prev 2013;14(7):4353-4358.

136. Li B, She H, Zhang S, Keupp J, Dimitrov I, Montillo A, Madhuranthakam AJ, Lenkinski R, Vinogradov E. Image Registration with Structurealized Mutual Information: application to CEST. In Proceedings of the 25th Annual Meeting of ISMRM, HI USA 2017:1293.

137. Harvey JA, Hendrick RE, Coll JM, Nicholson BT, Burkholder BT, Cohen MA. Breast MR Imaging Artifacts: How to Recognize and Fix Them 1. Radiographics 2007;27(suppl_1):S131-S145.

138. Ah-See M-LW, Makris A, Taylor NJ, Harrison M, Richman PI, Burcombe RJ, Stirling JJ, d'Arcy JA, Collins DJ, Pittam MR. Early changes in functional dynamic magnetic resonance imaging predict for pathologic response to

neoadjuvant chemotherapy in primary breast cancer. Clin Cancer Res 2008;14(20):6580-6589.

139. Costa DN, Pedrosa I, McKenzie C, Reeder SB, Rofsky NM. Body MRI Using IDEAL. American Journal of Roentgenology 2008;190(4):1076-1084.

140. Wang X, Harrison C, Mariappan YK, Gopalakrishnan K, Chhabra A, Lenkinski RE, Madhuranthakam AJ. MR Neurography of Brachial Plexus at 3.0 T with Robust Fat and Blood Suppression. Radiology 2017;283(2):538-546.

141. Zhang S, Keupp J, Liu Z, Lenkinski RE, Vinogradov E. Saturation parameters influence on SAFARI performance. In Proceedings of the 23rd Annual Meeting of ISMRM, Toronto, Canada 2015.

142. Kuhl CK, Kooijman H, Gieseke J, Schild HH. Effect of B1 inhomogeneity on breast MR imaging at 3.0 T. Radiology 2007;244(3):929-930.

143. Singh A, Cai K, Haris M, Hariharan H, Reddy R. On B1 inhomogeneity correction of in vivo human brain glutamate chemical exchange saturation transfer contrast at 7T. Magn Reson Med 2013;69(3):818-824.

144. Zhou J, Yan K, Zhu H. A Simple Model for Understanding the Origin of the Amide Proton Transfer MRI Signal in Tissue. Applied Magnetic Resonance 2012;42(3):393-402.

145. Leupold J, Månsson S, Stefan Petersson J, Hennig J, Wieben O. Fast multiecho balanced SSFP metabolite mapping of 1H and hyperpolarized 13C compounds. Magnetic Resonance Materials in Physics, Biology and Medicine 2009;22(4):251-256.